Universidad Carlos III de Madrid

Bachelor Thesis

Analysis of Drag Reduction in Wingtip Devices

Andrea Mosquera Alonso

Director:

Daniel Gómez Lendínez

June 2017

To the memory of my grandfather, O. M.,
who dreamed of flying;

And to my grandfather, F.A.,
who taught me never to forget where I come from.

Acknowledgments

This work would not have been possible without the invaluable contributions of my tutor, professor Daniel Gómez Lendínez, whose help and dedication throughout the last months have been vital to overcome many apparently unsolvable challenges. It is thanks to his advice and efforts that I have been able to learn and progress in this endeavor. I would also like to thank professors Óscar Flores, Carlos Sanmiguel, and Javier Rodríguez, from Universidad Carlos III de Madrid, for their generous advice on key points of this project, and professor Basman Elhadidi, from the University of Cairo, for offering me the first insights into computational fluid dynamics.

I have been fortunate to receive the support of my friends and colleagues during the last years. We have braved through difficult times together and formed a family of sorts, bonded by our will to pursue a greater knowledge. I would not have reached this point without them.

To conclude, I want to thank my parents, who, despite deep differences, troubled times, and constant time-zone coordination problems, have loved and encouraged me to persevere, to devote my best efforts to every task, no matter how small, and to follow the dreams that keep pulling me away from them. For your open-mindedness and courage: thank you. And lastly, I want to thank Clara, my traveling companion in this difficult road we have chosen. It is thanks to her that I continue to see the meaning of our steps when dark times engulf them. May our journey take us to new, undiscovered lands in the years to come.

Ad astra per aspera,

A.

Abstract

Given the importance of fuel reduction in the aeronautical industry, for both economic and environmental purposes, the last few years have seen the popularization of wingtip devices as a mean to increase aerodynamic efficiency. This work presents and studies several wingtip device geometries at different flight conditions, assessing the impact that a number of geometric parameters cause on the lift and drag forces. This is performed through computational fluid dynamic simulations, potential flow-based panel method analyses, and an attempt at experimental measurements.

The main conclusions derived from this study indicate that, for several wingtip device configurations, it is possible to achieve a 10% increase in the aerodynamic efficiency of a given wing. The validity of the panel method employed is discussed, and several considerations are presented towards future numerical and experimental research.

Contents

List of Figures

List of Tables

Chapter 1

Introduction

1.1 Motivation

From the beginning of the 21st century, the aeronautical industry has devoted significant efforts to increasing the efficiency of commercial aircraft, in order to achieve longer flights for the same fuel mass -increased range and endurance- or reduce the fuel consumption for a given route. Several steps have been taken in this direction, including the design of more fuel-efficient engines, improvements in air traffic management and control, aerodynamic optimization, and international initiatives such as the International Air Transport Association (IATA) Fuel Action Campaign or the Clean Sky program. These efforts serve a double purpose. Firstly, to reduce fuel costs for airlines, which remain an economic burden: in 2016, American Airlines spent $4,712M in fuel for a total of 3,578M gallons, at a price of $1.32 per gallon [41]; for smaller, less fuel-efficient carriers, this value is much higher. Secondly, to contribute to the global efforts to decrease CO_2 emissions to the atmosphere. In an increasingly populated world where the reality of climate change can no longer be denied, every small action adds to the global struggle to preserve the planet. It is for this reason that IATA promotes and enforces the goal of reducing the net CO_2 emissions in the aviation industry by 50% by 2050, and why key aircraft manufacturers -such as Airbus or Boeing- are becoming progressively more engaged in these initiatives.

According to IATA [50], the commercial aviation industry is responsible for 2% of the global CO_2 anthropogenic, that is, due to human activity, emissions. Although significant progress has been made since the beginning of the jet aviation era, it is widely understood that stronger measurements are required to minimize the emissions of greenhouse gases in the following years. For this purpose, many stakeholders in the aerospace industry have subscribed to the four-pillar strategy developed by IATA in 2007, structured around four fundamental pillars [50]:

- **Technology**: efficient aircraft, engines, and equipment, and investments in new energy sources such as solar energy or biofuel.
- **Operations**: focused on weight reduction and maximum operating efficiency.

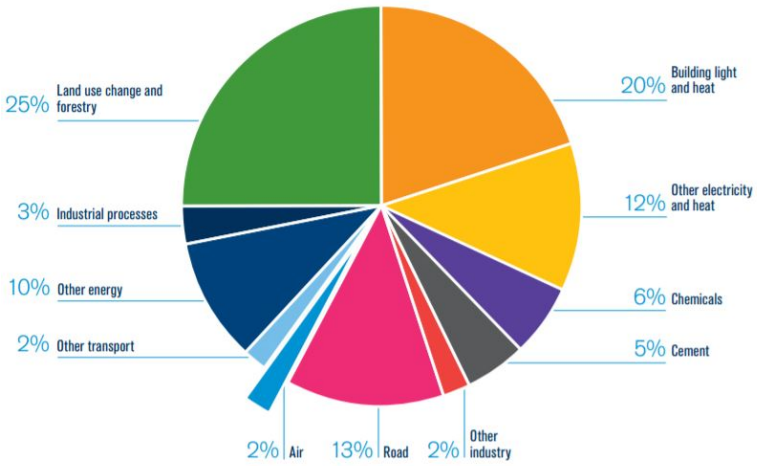

Figure 1.1: Sources of anthropogenic CO_2 emissions [50]

- **Infrastructure**: optimized routes, improved air traffic management and airport procedures, and unifying strategies such as the SES (Single European Sky) initiative.
- **Economic measures**, such as the global emissions trading, which hope to compensate and eventually lower CO_2 emissions worldwide.

Among these four pillars, technology is inarguably the most relevant. Technological advances have allowed fuel consumption to be reduced by 70% since the early jet age [50] and are expected to decrease much more in the coming years; in addition to the expected changes in CO_2 emissions, NOx emissions to the atmosphere -a group of greenhouse gases which may pose a severe threat to the ozone layer- are expected to decrease by 80% in 2020. Some initiatives currently studied or being developed include structural improvements, such as load alleviation, a greater use of composite materials, smart wing technologies and actuators, and morphing wings; system modifications, such as landing gear changes or substitutions, intelligent power units, and energy harvesting; and aerodynamic advances, including drag reduction coatings, variable camber wings, refined high-lift devices, and optimized wingtip devices, as well as a number of efficiency-focused improvements on aircraft engines. A number of innovative technological concepts, as improbable as they might seem, have been proposed as viable options for future aviation; such is the case of the hybrid wing body (HWB), electric and pulse propulsion systems, and truss-braced wings. The aim of this project is to focus on a some particular cases regarding aerodynamic optimization, through the simultaneous objectives of increasing the lift force acting on the aircraft and reducing the drag force directly related to fuel consumption.

1.2 Scope of this work

Among the vast range of improvements leading to a more efficient aviation industry, some of which have been described above, this project has been selected to focus on the potential increase in aerodynamic efficiency achievable through the use of wingtip devices. To this extent, several wingtip device shapes have been modeled and analyzed through both computational fluid dynamics and potential-flow based numerical methods. These include simple, blended, and double winglets; raked wingtips, and wingtip fences. Since, due to computational limitations, it was not possible to perform a comprehensive study of the effect of the many geometric parameters possibly affecting fluid flow, the research was restricted to the effect of cant angle Θ, winglet area, and the comparison between several models based on those existing either in real-world applications or as potentially applicable concepts.

The effect of the selected wingtip devices on the flow surrounding a given wing, and thus on the forces acting on said wing and its aerodynamic efficiency, were studied for two flight conditions simulating those of the cruise and takeoff flight phases. Since, as in the case of the geometric parameters considered, many more operating points should be included in this analysis, this project claims only to be a preliminary approach to the complex problem of wingtip devices design, and to set the foundations and tools required to conduct, in future projects, further investigation on the matter.

1.3 Objectives

There were several objectives defined at the beginning of this work, mainly related to obtaining a quality estimation of the behavior and impact of wingtip devices:

- To observe the effects of several wingtip devices on aircraft performance through the variations they caused on the aerodynamic efficiency L/D of a given wing, and to determine the role and importance of the geometric parameters involved at different flight conditions, through computational fluid dynamics (CFD) simulations.
- To find or suggest an optimum configuration to maximize aerodynamic efficiency in every flight condition.
- To investigate the validity of the three-dimensional panel method implemented in the XFLR5 software as a less time-consuming alternative to the CFD simulations.
- To conduct, if possible, experimental measurements to support or challenge the results found through numerical procedures.

Secondary objectives, oriented towards personal development, included becoming familiar with the Dassault Systèmes CATIA software and with the theoretical foundations behind computational fluid dynamics, as well as with the laboratory procedures, tools, and equipment employed for this work.

1.4 Document overview

The next chapters, describing the methodology and results employed in this work are structured in the following manner:

- **Chapter 2: Winglet Aerodynamics** explains briefly the mathematical models for basic wing and winglet aerodynamics, including the principle of induced drag reduction that led to the implementation of wingtip devices.
- **Chapter 3: State of the Art** introduces the main wingtip devices existing in the aeronautical industry nowadays, along with the socioeconomic and legal framework related to their incorporation and design.
- **Chapter 4: Wing and Winglet Geometry** presents the geometries employed in this analysis, their dimensions and characteristics, and the expectations set for each of them in terms of flow field perturbation and drag reduction.
- **Chapter 5: CFD Analysis** gathers the entire process followed to perform the computational fluid dynamics simulations, including the definition of the geometry and mesh, the observation of the quality requirements for the mesh, and the simulation setup, as well as the mathematical models employed.
- **Chapter 6: VLM and 3D Panel Method** is dedicated to potential flow-based aerodynamic numerical methods, comprising the vortex lattice method employed to find the cruise angle of attack, and the three-dimensional panel method analysis through the XFLR5 software.
- **Chapter 7: Mission Design** attempts to provide an overview of the parameters employed throughout this work to measure aircraft performance, and presents the example missions used to translate the changes in aerodynamic efficiency to real-world applications.
- **Chapter 8: Experimental Measurements** details the experimental procedure, tools, and materials, and explains the inconveniences and obstacles which arose during this process.
- **Chapter 9: Analysis of CFD Results** exhibits the results found through the computational fluid dynamics simulations and proceeds to their analysis.
- **Chapter 10: Analysis of XFLR5 Results** displays and comments, in a similar manner, the results found through the XFLR5 analyses, and compares them to those found in the previous chapter.
- **Chapter 11: Project Budget and Planning** develops the working aspects of this project, included its budget, planning, and the economic and temporal allocation of tasks and resources.

- **Chapter 12: Conclusions and Future Work** summarizes the main conclusions found in this study and mentions the general directions that it would be desirable to follow in future, related projects.

Chapter 2

Winglet Aerodynamics

2.1 Aerodynamic forces on an aircraft

Any body submerged in a fluid flow is subject to a force exerted by the effects of pressure and shear stress on its surface. For aerodynamic applications, the component of this force perpendicular to the fluid flow is termed *lift*, and that parallel to the fluid flow is named *drag*. When the body is held at an angle with the fluid flow, the lift and drag are related to the normal and axial forces over its surface through the angle of attack α, as shown in 2.1.

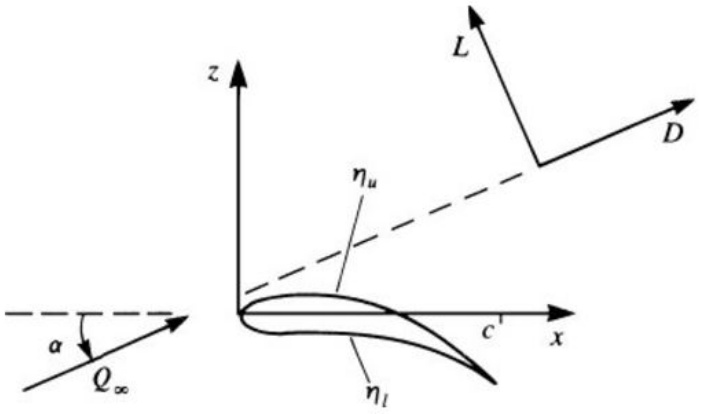

Figure 2.1: Aerodynamic loads on a cambered airfoil [17]

For a wing or aircraft in flight, the lift force is caused by a pressure difference between the upper and lower surfaces of the wing. The pressure on the upper wing surface falls to a much lower value than on its counterpart; it is this difference that counteracts the weight of the wing as a vertical force. The drag force, however, cannot be explained as the result of a single phenomenon: several sources, of varying importance depending on the aircraft characteristics and flow regime, must be considered.

2.1.1 Lift and drag coefficients

Aerodynamic loads are typically non-dimensionalized by means of the dynamic pressure of the freestream, $q_\infty = \frac{1}{2}\rho U_\infty^2$, and a reference surface, S, which is usually the wing planform area. The lift and drag coefficients are thus defined as:

$$C_L = \frac{L}{\frac{1}{2}\rho U_\infty^2 S} \tag{2.1}$$

$$C_D = \frac{D}{\frac{1}{2}\rho U_\infty^2 S} \tag{2.2}$$

Notations C_L and C_D are employed for the lift and drag coefficients of finite wings, while c_l and c_d are used for the flow over airfoils. The lift coefficient is determined by the aerodynamic characteristics of the wing and its angle of attack; for an infinite wing, $C_L = c_l$.

2.2 Sources of drag over a finite wing

Three main types of drag are usually differentiated: parasitic drag, induced drag or drag due to lift, and wave drag. The latter, which is caused by the presence of shock waves at transonic and supersonic speeds, is not considered in this analysis, which has only dealt with strictly subsonic flows. Parasitic and induced drag contribute to the total drag coefficient as $C_D = C_{D0} + C_{D,i}$.

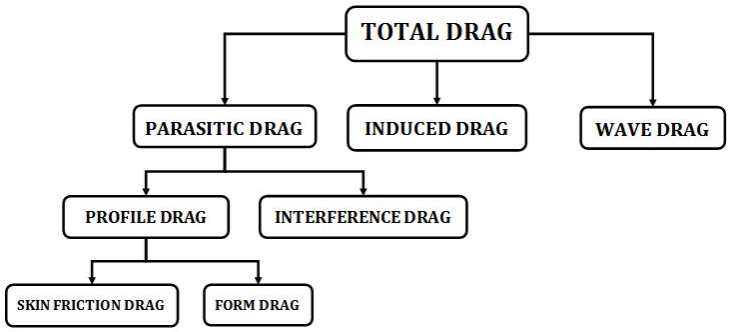

Figure 2.2: Subdivisions of drag sources

2.2.1 Parasitic Drag

Parasitic drag is said to be inherent to each aircraft, as it does not, unlike induced drag, depend on the other aerodynamic forces and moments acting on the body. It has been traditionally divided in skin friction drag, pressure or form drag, and interference drag.

Skin friction drag is due to the shear stress of the moving fluid over the surface of the aircraft; it is, thus, directly proportional to the wetted area of the aircraft. It is often estimated by multiplying this area by the skin friction coefficient

$$C_f = \frac{\tau_w}{\frac{1}{2}\rho U_\infty} \tag{2.3}$$

which can be approximated as a function of the Reynolds number: Anderson [2] gives $C_f = \frac{1.328}{Re^{1/2}}$ for laminar flow and $C_f = \frac{0.074}{Re^{1/5}}$ for turbulent flow. Skin friction drag reduction is often sought by attempting to minimize the surface roughness, through surface treatments, coatings, or careful maintenance, in order to delay the laminar-to-turbulent transition.

Form drag, on the other hand, is caused by the pressure imbalances appearing due to the separation of the boundary layer over a given region of the wing, and depends mainly on its shape; for this reason, the most effective way to reduce form drag is to modify - *streamline* - the shape of the body. It is difficult to find an adequate estimation of form drag values; they are typically included as a coefficient K in the expression corresponding to the skin friction contribution. Adding the effects of form drag and skin friction drag results in *profile drag*, dependent on the geometric characteristics of the wing.

$$C_{D,p} = KC_f S_{wet} \tag{2.4}$$

Lastly, interference drag is due to the combination of the fluid flow over the different surfaces of the aircraft, where the streamlines corresponding to the flow over the wings, fuselage, tail, and other components interfere with each other; it is particularly important at the meeting point of the wings and the fuselage, the vertical and horizontal tail surfaces, and other potentially conflicting regions on the aircraft. It is typically reduced by smoothing and rounding these unions, allowing for a better, less sharp mixing of the flow.

The total parasitic drag is given by the sum of skin friction, form, and interference drag, and is represented in the drag equation as C_{D0}, the drag coefficient for the aircraft at zero lift conditions.

2.2.2 Induced Drag

Induced drag appears in three-dimensional flows over finite wings. The same pressure imbalance between the upper and lower wing surfaces that accounts for the presence of lift causes the flow to "leak" around the wingtips, with a spanwise flow component traveling from wing root to wing tip in the lower surface, and inversely in the upper surface: the flow streamlines become *curled* upwards around the wingtips and the so-called *wingtip vortices* appear.

Trailing wingtip vortices have two main consequences: they contribute to the low-pressure region on the upper wing surface, thus favoring lift, and they cause *downwash*,

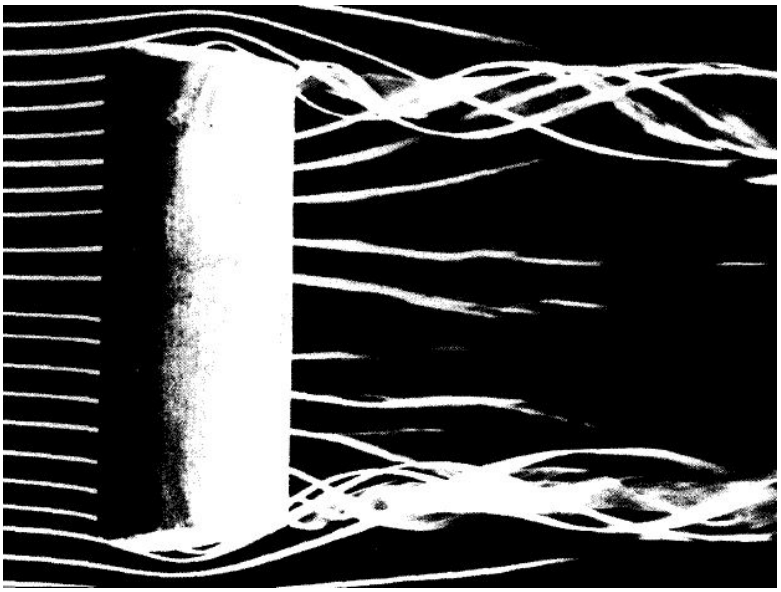

Figure 2.3: Trailing vortices for a rectangular wing [25]

a downward velocity component which, when added to the freestream velocity U_∞, creates a local relative wind at each wing section. As a result, the angle of attack of the wing is reduced, and the new *effective* angle of attack is obtained by subtracting α_i, the *induced* angle of the relative wind facing the airfoil section, so that:

$$\alpha_{eff} = \alpha - \alpha_i \tag{2.5}$$

As the aerodynamic forces are defined as perpendicular and parallel to the fluid flow, the local lift vector at each airfoil section is tilted backwards at an angle α_i. As shown in figure 2.4, a component of this local lift is oriented in the direction of the freestream velocity U_∞; when the local contributions of every airfoil section are added over the complete wing, the result is the *induced drag* or drag due to lift. Prandtl's lifting line theory provides an expression for the induced drag coefficient as:

$$C_{D,i} = \frac{C_L^2}{\pi e AR} \tag{2.6}$$

where it can be observed that the induced drag is directly proportional to the square of the lift coefficient and inversely proportional to the aspect ratio of the wing: wings with a high aspect ratio, such as those found in gliders, are better suited to reduce induced drag. Oswald's efficiency factor e accounts for the shape of the wing; for a wing with an elliptical lift distribution, which provides minimum induced drag, $e = 1$, while most general wings designed for subsonic regimes present an efficiency factor between 0.7 and 0.85.

The presence of induced drag affects not only the magnitude of the lift and drag forces, but also the proportionality of the lift coefficient to the angle of attack. While

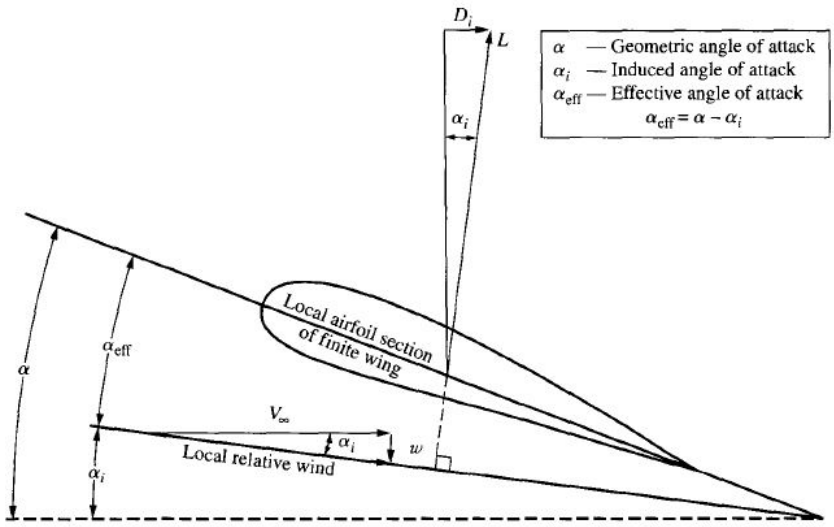

Figure 2.4: Effect of wingtip vortices on angle of attack [2]

the lift slope of an airfoil would be given by $a_0 = \frac{dc_l}{d\alpha}$, amounting to $a_0 = 2\pi$ for thin airfoil theory, in a finite wing this must be corrected to

$$a = \frac{dC_L}{d\alpha} = \frac{a_0}{1 + (a_0/\pi AR)(1+\tau)} \tag{2.7}$$

where the parameter τ is a function of the Fourier coefficients A_n employed in lifting line theory, with typical values ranging between 0.05 and 0.25 [2]. It is worth noting that the aspect ratio is, again, the key parameter affecting the lift and drag distribution over the wing: the higher the aspect ratio, the closer the lift slope becomes to that of the airfoil section, imitating an infinite wing.

The overall drag coefficient, C_D, adds together the contributions of the drag sources described as $C_D = C_{D0} + kC_L^2$, where $k = 1/\pi eAR$. The relative importance of each coefficient depends on the flight conditions and flow regime. Parasitic drag typically represents up to 75% of the total drag; induced drag amounts to 25% of the total drag in cruise conditions, but its importance is significantly increased during takeoff, where higher lift coefficient and angle of attack values are required.

2.3 The role of wingtip devices in drag reduction

Despite the wide range of wingtip devices employed in aviation nowadays [see chapter 3], their effects on flight performance can be summarized in two main points: increasing the lift generated at the wingtips and reducing the induced drag associated to the trailing vortices. These are achieved by including upwards-oriented surfaces at a given angle -Cant angle- with the wing planform. Since they interfere with the flow circulation

from the high pressure region at the lower wing surface to the low pressure region at the upper wing surface, they decrease the strength of the wingtip vortices and cause them to appear further downstream. This results on a direct decrease of the induced drag, and favors lift generation by smoothing the flow over the wingtips and creating a more uniform wake; the combination of these two effects increases the aerodynamic efficiency of lift-to-drag ratio L/D.

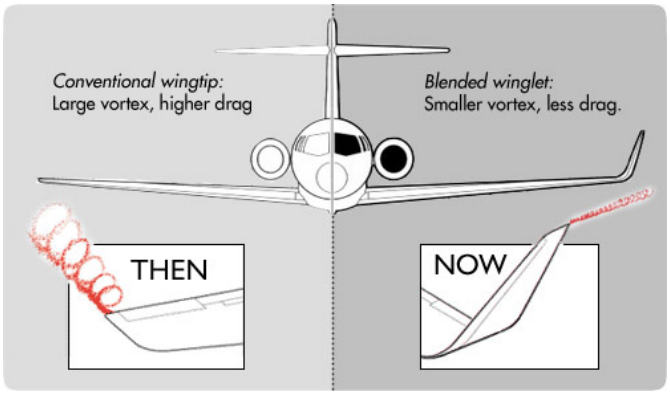

Figure 2.5: Schematic of vortex reduction at the wing tip [32]

It has been shown [43] that even the addition of two simple vertical plates at the wingtips causes a significant reduction in induced drag and a nontrivial increase in lift. The search for the most appropriate shapes and structures, however, has been a matter of discussion for the last decades. While several solutions have been proposed, none of them seem to be completely satisfactory. The fact that aircraft requirements and performance are very different at different flight phases and flow regimes only adds complexity to the wingtip devices design.

Chapter 3

State of the Art

3.1 Wingtip devices: Early Designs

Although the first wingtip devices to reduce drag were proposed early in the 20th century, they were not widely employed in the aeronautical industry until its last decades. British engineer Frederick W. Lanchester, whose contributions to the field of flight mechanics are widely known, is considered to be a pioneer in this trend, having designed a series of wing end-plates for the specific purpose of controlling wingtip vortices in 1897. The first winglets employed in an actual aircraft were patented in 1910 by William E. Somerville, who had them incorporated to some of his models. However, neither of these ideas enjoyed industrial-wide applications in the following years.

Figure 3.1: Somerville biplane with winglet-type wingtips [35]

The first functioning wingtip designs would not be incorporated to the aviation market until the 1930s, when the growing political instability that eventually led to World War II favored research in aeronautics, producing new and significant advances in the span of a few years. German engineer Alexander M. Lippisch, whose work on delta wings and ground effect would be widely employed in the future, designed a series of downwards-oriented wing endplates, known as the *Lippisch-Ohren* -Lippisch ears-, which would be installed on the Heinkel He 162A *Spatz* fighters. Although the purpose of these plates was not aerodynamic, but rather aimed to compensate for the unsatisfactory

dynamic stability of the aircraft, they proved to be quite useful at reducing induced drag. This subject was widely studied in the years after the war by Dr. Sighard F. Hoerner, who proposed a model of drooped wingtips still used for gliders nowadays. As it can be observed on figure 3.2, the beveled wingtip presents a sharp upper edge which forces the trailing vortices to appear farther downstream.

Figure 3.2: Hoerner wingtips installed on a Cessna 150h [31]

3.2 Whitcomb and winglet research

Following the 1973 oil crisis, the steep increase in fuel prices led the aeronautical industry to prioritize the role of aerodynamic efficiency in aircraft design. With this purpose, extensive research was carried out during the 1970s in order to maximize the lift-to-drag ratio and reduce fuel costs as much as possible. At the National Aeronautics and Space Administration (NASA), engineer Richard T. Whitcomb developed Hoerner's concept to show that winglets designed as a *vertical wing* at an angle -cant angle, Θ- with an aerodynamic profile could provide a significant reduction in drag while keeping bending moment values similar to those of the naked wing. Whitcomb's designs were later perfected and employed on several Lockheed and McDonnell Douglas aircraft manufactured during the 1980s and 1990s. During the same period, several companies performed their own studies on the possibilities of winglets in both business and commercial aircraft: Learjet developed its own winglet concept and had it implemented on several business jet models, claiming it had resulted on a 6.5% increase in range, and Boeing achieved a 3.5% increase in range by adding winglets to the already existing B747-300. In addition to its aerodynamic advantages, it was observed that wingtip devices were also useful to increase directional stability; a well-known application of this principle can be found in

the horizontal stabilizer of the Boeing 747 Shuttle Carrier.

Figure 3.3: Winglets being tested on a KC-135 during NASA research [38]

3.3 Wingtip devices design in the 21st century

From the beginning of the 21st century, most commercial aircraft and business jets, as well as some military aircraft, have incorporated some kind of wingtip devices to their design. Airbus employed winglets in the A320 Enhanced and incorporated wingtip fences -thin, vertical winglets extending both above and below the wing surface- to most of its commercial aircraft models, including the A320, A350, and A380 families, while Boeing added 1.8m winglets to most of its B747-400 aircraft. The most recent business jet models from Gulfstream Aerospace, Dassault Group, and similar companies have joined this trend as well.

Significant improvements over the simple, Whitcomb-type winglet have been achieved during the last years. One such example is that of Aviation Partners Boeing, whose Blended Winglets™ concept incorporated a rounded, smooth union between wing and winglet, in order to reduce the interference drag usually originated at this joint; they are now included in all B737 Next Generation (figure 3.4). Cessna's *Citation X* aircraft, shown in figure 3.5, is already equipped with Elliptical Winglets™ designed by Winglet Technology, which allegedly favor a close-to-elliptical lift distribution in the whole wing and, consequently, minimum induced drag. In 2009, Airbus presented its own blended winglet design, the Sharklet, which provides a 3.5% decrease in fuel burn and an increase of up to 100nm in range according to the manufacturer; sharklets have performed up to expectations and are now standard on the new A320neo family (figure 3.6).

Figure 3.4: Blended Winglet [32]

Figure 3.5: Elliptical Winglet [44]

Figure 3.6: Sharklet concept on an A320 rendering [26]

Further modifications to the Whitcomb winglet and early designs have been employed regularly in the aeronautical industry since the 1990s. Wingtip fences, based on the same concepts as winglets, provide an effective reduction of induced drag while avoiding the increase in wingspan, which can become troublesome for operational purposes. Due to this advantage, wingtip fences -shown in figure 3.8- were widely employed in most Airbus commercial aircraft families during the 1990s and 2000s. Several designs experimenting with double winglets have also been recently proposed, being the upper surface a classical, Whitcomb or blended winglet-type shape, and the lower a simple winglet oriented downwards, either symmetrical to or at a wider angle than its counterpart. The main goal of this concept is to employ the upper surface to increase the effective wingspan and thus the lift, while preventing flow recirculation and displacing the trailing vortices farther downstream with the lower surface; it is also meant to increase the dynamic stability of the aircraft. Split Scimitar^{TM} winglets, developed by Aviation Partners Boeing and installed on several B737 models (figure 3.9), represent yet another step in the evolution of this design.

Beyond the Whitcomb-type winglet and related designs, several wingtip devices

Figure 3.7: B737 MAX equipped with double winglets [32]

Figure 3.8: Wingtip fence, A310 [28]

Figure 3.9: Split Scimitar winglet, B737 [32]

concepts have been shown to be useful in reducing induced drag. Raked wingtips -a span extension with a sweep angle much larger than that of the wing- were a characteristic feature of Boeing commercial aircraft for many years, and are still employed in models for both commercial and military purposes. Although raked wingtips -shown in figure 3.10- have a significant improvement on aircraft performance, and may yield better results than conventional winglets during cruise, a larger wingspan increases the bending moment acting on the wing as well. However, they can still be observed on several long-range commercial as well as military patrol aircraft -including the CN235 employed as a reference for this work.

Lastly, it is worth mentioning other experimental designs not yet implemented on certified aircraft, such as the spiroid winglets (figure 3.11), which employ a closed loop shape at the end of the wing and are being tested by Aviation Partners with moderate success; or consecutive wing sections with variable cant angles forming non-planar wings with increasing dihedral. Multi-winglet designs have also been researched, with several proposals on the matter available on literature [22], imitating the long wingtip feathers present in birds of prey. Future trends include actuating winglets, which would be able to change their shape or position depending on the flight condition requirements, but

this field -and that of morphing wings and aircraft in general- is still on its early stages of development.

Figure 3.10: Raked wingtip, B767 [33]

Figure 3.11: Spiroid tip, Falcon 50 [39]

3.4 Socioeconomic framework

As it has been mentioned in previous sections, the reduction in induced drag achieved by the incorporation of wingtip devices causes both an increase in the aircraft's range and a significant reduction in fuel consumption. Airbus states a range increase of 100nm for the A320 models retrofitted with sharklets; Aviation Partners Boeing mention a 65nm increase for a 737-700 equipped with Split Scimitar Winglets (SSW) and 180nm for Blended Winglets; and Winglet Technology presents improvements between 220nm and 550nm for the Cessna Citation X aircraft including Elliptical Winglets, as shown in figure 3.13. As for the fuel consumption, Winglet Technology mentions a 6% for high speed cruise flight profiles; Aviation Partners Boeing provides 7% fuel savings with Blended Winglets, and Airbus states that sharklets yield a fuel reduction of up to 4% on the A320.

The advantages of wingtip devices, however, do not seem to be limited to these two matters. It has been shown that aircraft equipped with winglet-type designs improve their takeoff performance significantly, as could be expected since winglets operate best on high lift and low speed conditions. Due to the same reason, they have a positive impact on climb performance as well, providing an improved climb gradient, and reducing the time to climb by up to 60%: Winglet Technology mentions a reduction from 84 to 27 minutes to climb to FL450 at ISA conditions, for the Citation X with Elliptical Winglets at MTOW; this leads to higher initial cruise levels as well. Finally, the reduction in induced drag allows for increased speeds at higher altitude, and the improved control over the formation of wingtip vortices has a significant impact on the dynamic stability of the aircraft.

It must be noted as well that the reduction in fuel consumption leads to a reduction in fuel costs. This will yield a substantial benefit for airlines deciding to equip new

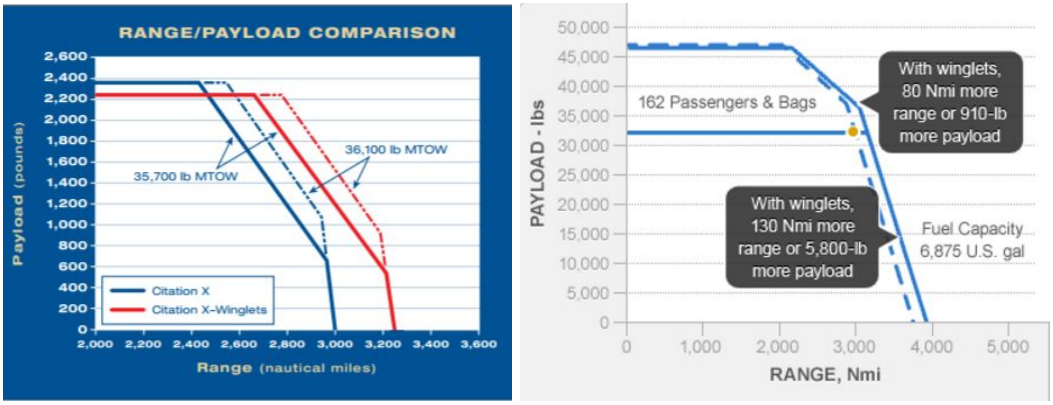

Figure 3.12: Payload-range diagrams for the Citation X (left) and B737-800 [44], [32]

aircraft with wingtip devices, or to retrofit their existing fleet to include the newest winglet designs. Another consequence, more important at a global level, is that of reduced emissions: according to an Aviation Partners estimation, Blended Winglets reduce CO_2 emissions by 6% and NOx emissions up to 8% [32]. Airbus states [26] that the incorporation of sharklets to its A320 family reduces 900 tonnes of CO_2 per year and aircraft. Noise levels at takeoff could also be reduced through wingtip devices: blended winglets for Boeing aircraft have reduced the noise-affected area at takeoff by 6.5% [32]. Consequently, finding more effective designs for wingtip devices has become a key point in the global research for more efficient, environment-friendly aircraft, and new improvements on existing concepts can be expected to appear in a close future.

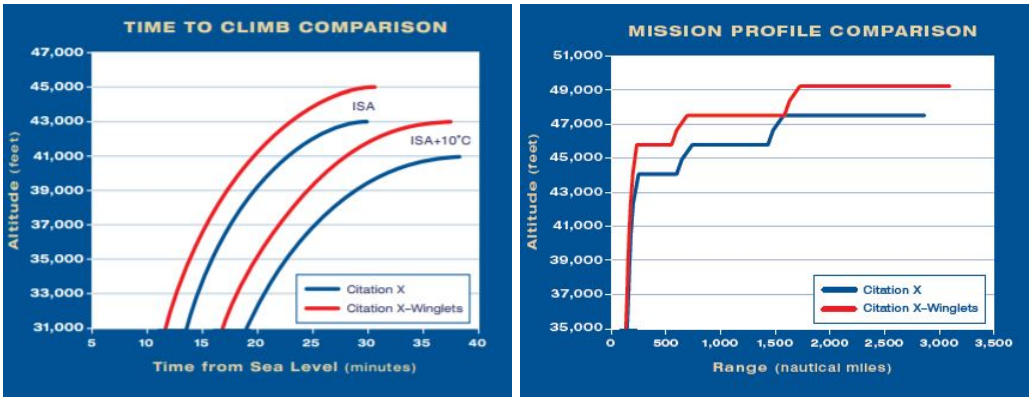

Figure 3.13: Time to climb (left) and mission profile for the Citation X [44]

3.5 Legal framework

In the aeronautical industry, both aircraft operators and aircraft manufacturers are subject to compliance with several sets of regulations typically established by national

Program	CO2 Reduction
737-700	1,163 Tons
737-800	1,374 Tons
737-900	1,585 Tons
737-300/500	1,057 Tons
757-200	3,170 Tons
767-300ER	5,284 Tons

Figure 3.14: CO_2 reduction for several Boeing aircraft [32]

or supranational agencies. These regulations depend on the country of manufacturing or operation of each aircraft, as well as its type: commercial airplanes, military aircraft, business jets, etc. The main agencies accountable for this legal framework are:

- **EASA**: the European Aviation Safety Agency, the European Union organization providing certifications, regulations, and support to aircraft manufactured or operating in European territory. It enforces the single market policy within the EU for the civil aeronautical industry, and ensures that minimum safety and environmental standards are kept. Civil aircraft operating on European grounds are subject to the Certification Specifications (CS), particularly the CS-25 for large commercial transport aircraft.

- **FAA**: the Federal Aviation Administration, EASA's counterpart in the United States of America. It provides the Federal Airworthiness Regulations (FAR), which are enforced in the USA as well as employed as a reference worldwide. FAR specifications are typically equal or extremely similar to those determined by EASA, in order to facilitate standardization at a global level.

- The **U.S. Department of Defense**, which redacted the defense standards (MIL-STD or MIL-SPECS) to which military aircraft operated by the United States must be subjected. They are typically employed as a reference for all military aircraft, especially the standards concerning maneuverability and handling qualities.

- **NATO**, the North Atlantic Treaty Organization, whose Standardization Agreements (STANAG) cover some topics related to military aviation such as air-to-air refueling procedures or UAVs.

- The United Kingdom's **Ministry of Defence**, in particular the Military Aviation Authority, whose defense standards DEF-STAN 00-970 (Design and airworthiness requirements for service aircraft) are a European reference for military aircraft requirements.

- At a national level, **AESA** -Agencia Estatal de Seguridad Aérea- is the public organization in charge of ensuring the correct application of the European and international regulations.

Wingtip devices are not usually a key element of civil or military aircraft regulations. As a matter of fact, it is difficult to find references to wingtip devices in the regulatory framework; those who do appear often reference aeroelastic or structural constraints. To name a few:

- In the Certification Specification CS 25.445, concerning outboard fins in large airplanes: "When significant, the aerodynamic influence between auxiliary aerodynamic surfaces, such as outboard fins and winglets, and their supporting aerodynamic surfaces must be taken into account for all loading conditions including pitch, roll and yaw maneuvers, and gusts as specified in CS 25.341(a) acting at any orientation at right angles to the flight path" [49]
- In the MIL-A-8867C(AS), section 3.8.3.5.14: "The frequencies and mode shapes of speed brakes, spoilers, scoop, leading edge flaps, winglets, (...) shall be measured" [51]
- In the Advisory Circular AC 23.1419-2D, from the Federal Aviation Administration, Appendix 3 (Guidelines for Supplemental Type Certificates and Amended Type Certificates on Airplanes), 1.e.10.a.4: "For unprotected winglets, flutter margins need to be addressed". [54]
- In the UAV Systems Airworthiness Requirements (draft STANAG 4671), for section USAR.445: Outboard fins or winglets:
  - a. If outboard fins or winglets are included on the horizontal surfaces or wings, the horizontal surfaces or wings must be designed for the maximum load in combination with loads induced by the fins or winglets and moment or forces exerted on horizontal surfaces or wings by the fins or winglets. (...)
  - c. The endplate effects of outboard fins or winglets must be taken into account in applying the yawing conditions of USAR.441 and USAR.443 (...) [52]
- Winglets appear on the list of significant alterations that may adversely affect fatigue critical structure, in the AC 120-93 Advisory Circular from the Federal Aviation Administration [53].

It can be observed that aeroelastic vibration and flutter, fatigue, vertical loads on the wing, and dynamic stability are the primary concerns relating to the addition of wingtip devices to the wing geometry, with little or no regard to the purely aerodynamic characteristics of these structures.

For both civil and military aircraft, the certification process involves at least three main documents: Type Certificates (TC), which are the main certification documents

for every general aircraft model; Supplemental Type Certificates (STC), Amended Type Certificates (ATC) or Approved Design Change Certificates (ADCC), which approve specific changes in the design of a given aircraft; and Airworthiness Certificates. which declare a given aircraft fit to fly. Although the incorporation of wingtip devices in the design of new aircraft would not require additional certifications, as it would be included in the Type Certificate for that given aircraft, the addition of newly-designed wingtip devices -such as the sharklet retrofitting program offered by Airbus for its A320 family- would certainly require the issue of a specific Supplementary Type Certificate for each case.

Chapter 4

Wing and Winglet Geometry

4.1 Preliminary considerations

When considering the existing winglet models currently employed in the aerospace industry -many of which were shown in the previous chapter- it was observed that they were remarkably diverse, ranging from simple endplates, as shown in figure 3.1, to complex aerodynamic shapes as seen in the Split Scimitar^{TM} winglets or the experimental spiroid designs. Given this wide range of existing wingtip devices, as well as the inevitability of time constraints, several basic models were chosen as an example of every concept for the purposes of this study, attempting to examine the main parameters considering their design at several operating points.

Figure 4.1: CN235 aircraft [36]

The necessary support for these winglet models was provided by a wing based on that employed by the CASA/IPTN CN235 aircraft, shown in figure 4.1: a medium range twin-turboprop aircraft widely employed during the last years for military transport, surveillance, and maritime patrol purposes. The CN235 was chosen for this purpose due to its characteristics as a common subsonic aircraft whose later versions, such as the CN295, have incorporated wingtip devices such as short winglets or raked wingtips.

4.2 Wing geometry

The airfoil employed for the design of this wing was the NACA 65(3)-218, a NACA model with a maximum thickness of 18% located at 39.9% of the chord and a maximum camber of 1.1% at 50% of the chord, as shown in figure 4.2. As usual in NACA 6-series airfoils, the first digit indicates the series; the second, the location of the area of minimum pressure, in this case at 50% of the chord; the third and fourth state that the airfoil provides a reduction in drag at lift coefficients 0.3 above and below the design lift coefficient of 0.2; and the maximum thickness of 18% of the chord is given by the fifth and sixth digits. NACA 6-series airfoils present substantial advantages with respect to their predecessors, series 4 and 5; among them, a high maximum lift coefficient, reduced drag for a certain range of operating conditions, and a design optimized for high speed. Despite their higher drag outside of those given operating conditions, high pitching moment, and poorer stall behavior, they are widely used nowadays for both civil and military applications. Although it is quite common to find variable airfoil wings in modern aircraft, the same airfoil was employed for all wings sections for simplicity.

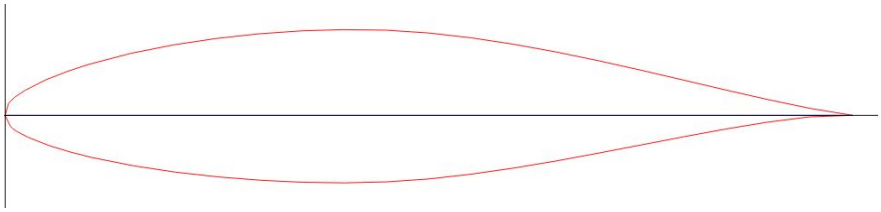

Figure 4.2: NACA 65(3)-218 airfoil [27]

The wing planform, shown in figure 4.3, comprised an inner rectangular section, which would be adjacent to the fuselage and support the engines, and an outer, swept trapezoidal section. This configuration was based on the wing of the CN235 aircraft, although some parameters were adjusted. The final wing planform was defined through a root chord, C_{root}, of 3m; a tip chord, C_{tip}, of 1.2m; a rectangular section of length 4.25m, and total semi-span $b/2 = 15.915$m. The sweep angle at the quarter chord for the trapezoidal section, defined as the angle formed by the quarter chord line with respect to a line perpendicular to the chord at the wing root, was $\Lambda_{25\%} = 3.86^{o}$, and the total wing planform area was calculated to be $S = 37.2465m^2$, as the sum of the areas of its rectangular and trapezoidal sections.

The usual geometrical parameters describing the wing, such as its mean geometric chord (MGC), its mean aerodynamic chord (MAC), and the sweep angle at the leading edge Λ_{LE} and taper ratio of its trapezoidal section, were calculated according to equations 4.1 to 4.4 and are gathered in Table 4.1. The aspect ratio of the wing, computed as $AR = b^2/S$, and employed later in the calculations involving the cruise angle of attack and induced drag coefficients, was found to be AR=6.8. Although this value is low for those typically found in this aircraft category, the higher induced drag characteristic of low aspect ratio wings would only be beneficial for this study.

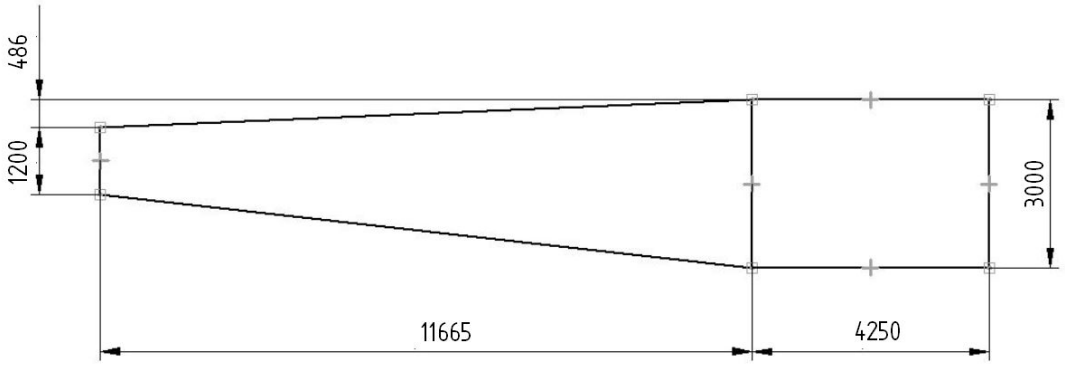

Figure 4.3: Wing geometry. Dimensions in mm

$$MGC = \frac{S}{b} = \frac{\int_0^{\frac{b}{2}} C dy}{\int_0^{\frac{b}{2}} dy} \tag{4.1}$$

$$MAC = \frac{\int_0^{\frac{b}{2}} C^2 dy}{S/2} \tag{4.2}$$

$$\Lambda_{LE} = arctan(\frac{\frac{C_{tip}}{4} - \frac{C_{root}}{4}}{b/2}) \tag{4.3}$$

$$\lambda = \frac{C_{root}}{C_{tip}} \tag{4.4}$$

b/2 (m)	S (m^2)	MGC (m)	MAC (m)	y_{MAC} (m)	λ	$\Lambda_{25\%}$ (º)	Λ_{LE} (º)
15.915	37.247	2.34	2.491	7.547	0.4	2.388	3.860

Table 4.1: Wing geometrical parameters

4.3 Short Winglets

The first wingtip devices designed were the so-called short winglets, small structures with the same aerodynamic profile as the main wing and a trapezoidal planform, with a semi-span $b_{sw}/2 = 1m$, a chord at the root of 1.2m, and the same leading and trailing edge sweep angle as the wing. Figure 4.4 shows the geometry of the winglet in detail. The detailed geometrical parameters of the wing, such as the MGC and MAC, were calculated according to the procedure described in the previous section, and are shown in Table 4.2.

In order to study the behavior of the winglet in different orientations, several wings were modeled with short winglets placed at an increasing angle with respect to the wing

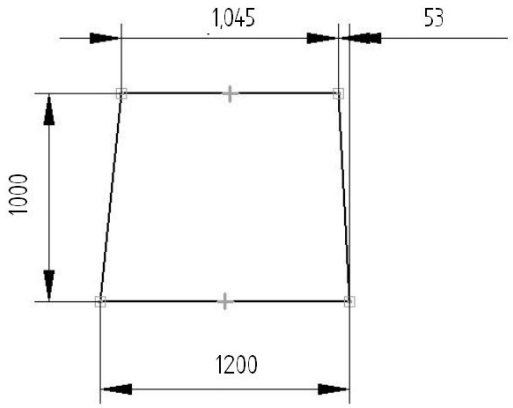

Figure 4.4: Short Winglet geometry. Dimensions in mm.

b/2 (m)	S (m^2)	MGC (m)	MAC (m)	y_{MAC} (m)	λ
1.000	1.123	1.223	1.124	0.489	0.871

Table 4.2: Long Winglet geometrical parameters

planform (Cant angle), yielding six final wing + short winglet combinations at 0º, 15º, 30º, 45º, 60º, and 75º.

4.4 Long Winglets

In order to study the effect of extending the winglet length, a new set of winglets, termed *long winglets*, were designed. They had similar characteristics to the short ones, keeping the same leading and trailing edge sweep angles as the wing, but their semi-span was increased to $b_{lw}/2 = 2m$. Their geometry and position in the wing are shown in figures 4.5 and 4.6, respectively, while their describing parameters are gathered in table 4.3.

b/2 (m)	S (m^2)	MGC (m)	MAC (m)	y_{MAC} (m)	λ
2.000	2.091	1.046	1.053	0.951	0.743

Table 4.3: Short Winglet geometrical parameters

As in the previous case, several long winglet configurations were considered, yielding six wings at cant angles 0º, 15º, 30º, 45º, 60º, and 75º.

4.5 Blended Winglets

Blended winglets were designed as an evolution of the long winglets described above, in an attempt to reduced the interference drag due to the wing-winglet joint by smoothing this area. The resulting winglets were curved, as shown in figure 4.7, by including a

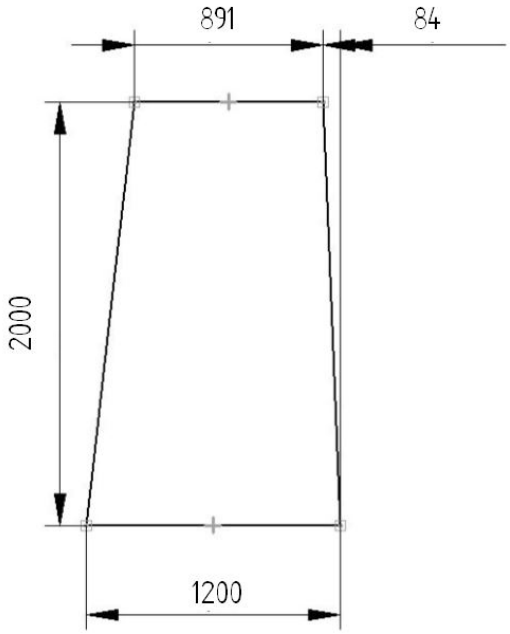

Figure 4.5: Long Winglets geometry. Dimensions in mm

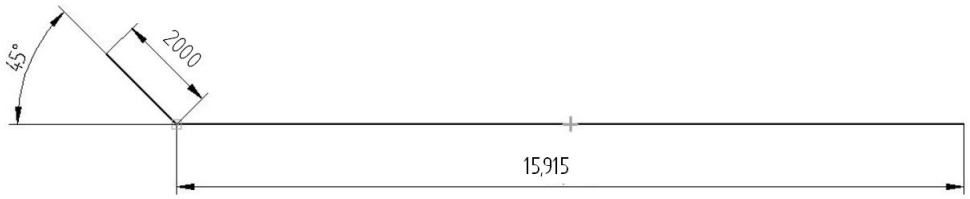

Figure 4.6: Long Winglets position in the wing, for a winglet at 45° cant angle

circular fillet between two points in the wing and winglets at a distance of 450mm from their union.

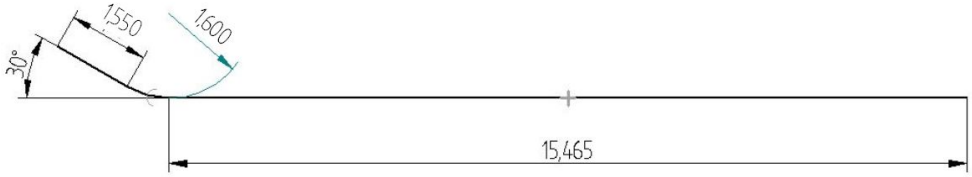

Figure 4.7: Blended winglet at 30°

Three different wing+blended winglet combinations were designed, at cant angles of 30°, 45°, and 60°, and with fillet radii of 1600mm, 1200mm, and 800mm respectively.

4.6 Double Winglets

Double Winglets, inspired by the Split Scimitar^{TM} winglets designed by Aviation Partners Boeing, were a variation of the blended winglets which incorporated a smaller, symmetrically oriented winglet on the lower surface of the wing, as shown in figure 4.8. It was intended that this additional surface would contribute to prevent the recirculation of the flow around the wingtip, thus reducing the induced drag substantially. Figure 4.9 shows the small winglet geometry, whose parameters can be found in table 4.4.

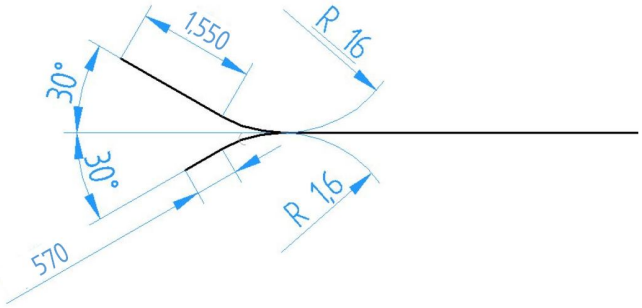

Figure 4.8: Double winglet at 30°

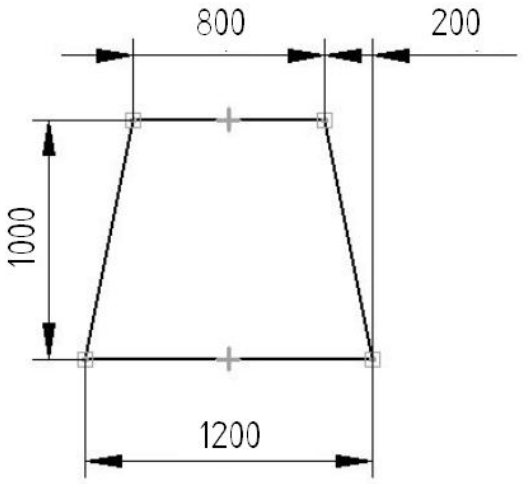

Figure 4.9: Lower double winglet geometry

b/2 (m)	S (m^2)	MGC (m)	MAC (m)	y_{MAC} (m)	λ	$\Lambda_{25\%}$ (°)	Λ_{LE} (°)
1.000	1.000	1.000	1.013	0.468	0.67	11.310	5.711

Table 4.4: Lower double winglet geometrical parameters

As in the previous case, three wing + double winglet configurations were modeled,

at cant angles of 30º, 45º, and 60º. As it can be observed in figure 4.8, the radius of the fillet employed for the lower winglet was the same as that employed for the upper one.

4.7 Raked Wingtip

Since the raked wingtip has been the default wingtip device employed in the CN235 aircraft in the last years, it seemed fitting to try at least one application of this concept. Raked wingtips, by definition span extensions with a much higher sweep angle than that of the wing, seem to provide a significant drag reduction at cruise altitudes and speeds, but may increase the bending moment of the wing beyond desirable limits. The wingtip used in this study had a span of $b_{rw}/2 = 655$mm, a sweep angle at the leading edge of $\Lambda_{LE} = 47.11^{o}$, and a taper ratio $\lambda = 0.35$, as it can be appreciated in figure 4.10.

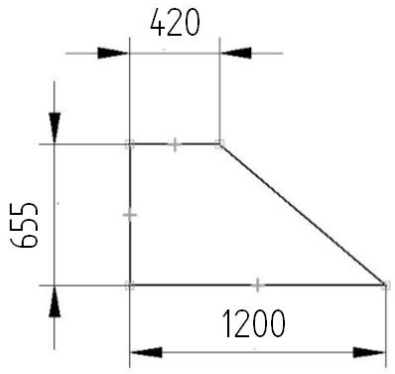

Figure 4.10: Raked wingtip geometry

4.8 Wingtip fence

The wingtip fence was another example of wingtip device widely employed in the aeronautical industry. It could be considered the counterpart of the raked wingtip, as it consists of a vertical aerodynamic profile positioned at the wingtip. While it does not provide additional lift, it contributes to reducing the induced drag by introducing a vertical disturbance in the flow. Since it does not modify the effective span of the wing, it has been employed in several commercial aircraft models, including some Airbus families, for which an increased wingspan could present some problems at airports complying narrowly with runway and taxiway width regulations.

Wingtip fences typically present a highly sweptback upper section and a smoothly curved lower section; in this example, an upper section with a leading edge sweep of $\Lambda_{LE} = 60^{o}$ was employed, along with a curved lower section with a curvature radius $R = 1600mm$. A separation of 150mm was allowed between the leading edge of the

wingtip and the beginning of the wingtip fence, as customary in commercial aviation to avoid additional drag.

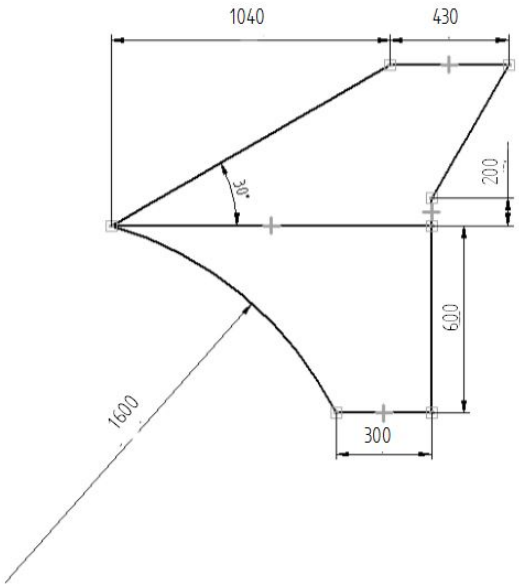

Figure 4.11: Wingtip fence geometry

4.9 Multi-winglet configuration

The last geometry considered was a multi-winglet configuration, loosely based on the experimental designs presented in [22]. While multi-winglet concepts are far from being transformed into real-world applications, this is mainly due to structural constraints rather than aerodynamic ineffectiveness.

As a matter of fact, the most common wingtip devices found in nature are the tip feathers present in raptor wings, which they can adjust at will depending on flight conditions, either to improve their aerodynamic efficiency or to reinforce aerodynamic braking. Multi-winglet designs often try to imitate this concept by including several thin winglets at different cant angles Θ. In this case, three blended winglets were located at the wingtip, with root chords measuring 300, 500, and 400mm, and placed at cant angles $\Theta = -30^o$, $\Theta = 30^o$, and $\Theta = 60^o$.

Close attention was paid to the distribution of tip feathers in the wings of several eagle, falcon, and vulture species. In an attempt to reproduce the general trends found in these observations, the blended winglet closer to the wing leading edge was oriented downwards, with the two following winglets placed at $\Theta = 30^o$ and $\Theta = 60^o$ as shown in figure 4.14.

Figure 4.12: Griffon vulture in flight [40]

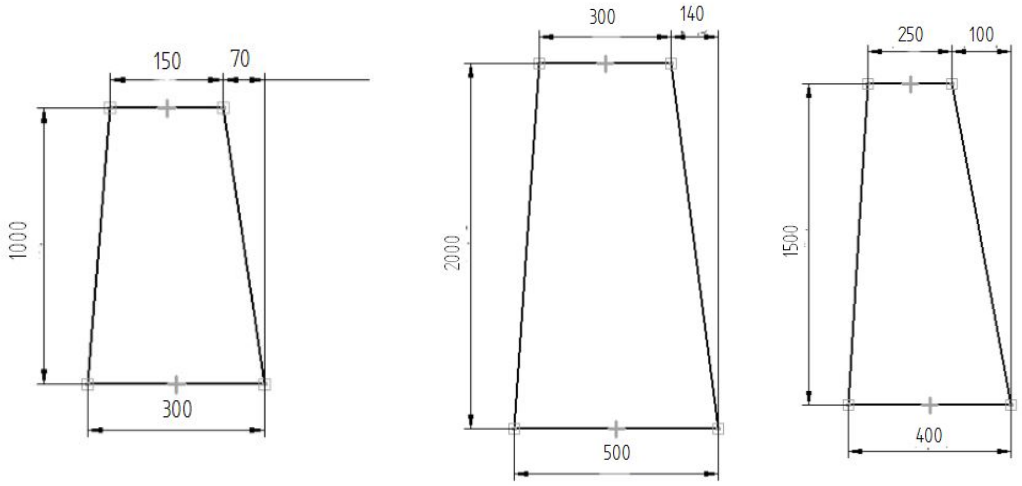

Figure 4.13: Planform dimensions from wing LE (left) to wing TE (right)

Similarly, the dimensions of each winglet were adjusted so that the shortest winglet would be the downwards-oriented winglet at the leading edge, followed by the trailing edge winglet at $\Theta = 60^{o}$. It was expected that the downwards-oriented winglet would contribute to prevent flow recirculation around the wingtip, while the two remaining winglets would help to disperse the resulting wingtip vortices into the free stream.

4.10 Software employed

All the wing designs discussed in this section were modeled using the student version of Dassault Systèmes' CATIAv5, a 3D computer-aided design software widely employed in the aerospace industry at present. The resulting 3D models for several of the wing

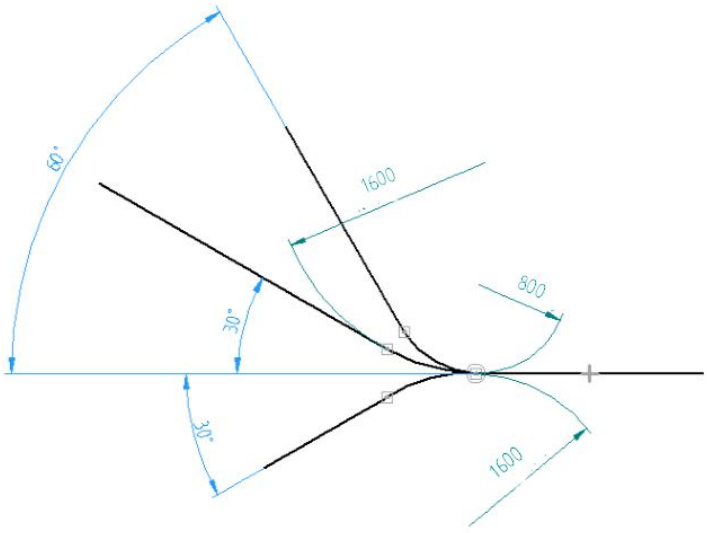

Figure 4.14: Cant angles and curvature radii for the multi-winglet configuration

and winglet configurations described are shown in figures 4.15 to 4.17.

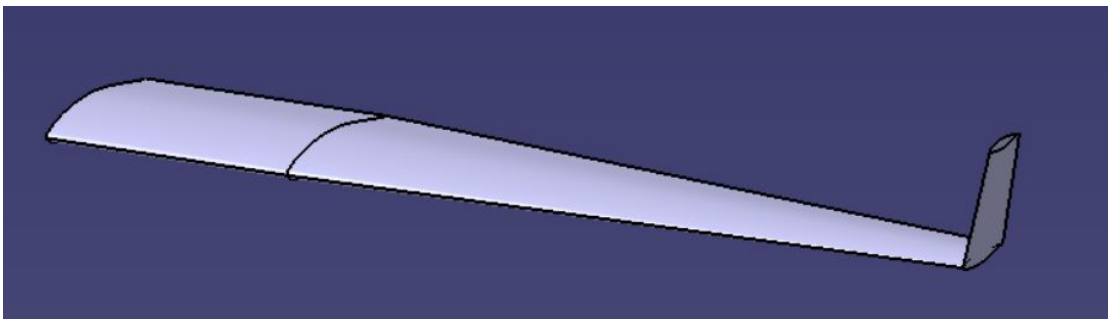

Figure 4.15: Long Winglet at 75°

As a highly versatile modeling tool, CATIA provided a flexible environment which enabled the design of complex three-dimensional features. The NACA 65_3 airfoil section employed for the wing was imported from the coordinates provided by the Airfoil Tools [27] database and scaled for every wing and winglet section, ensuring that the airfoil geometry was respected at all times. The final geometries were defined by sketches corresponding to those shown for the wing and wingtip device planforms in the previous sections, and all avoidable sharp joints were trimmed and smoothed as necessary.

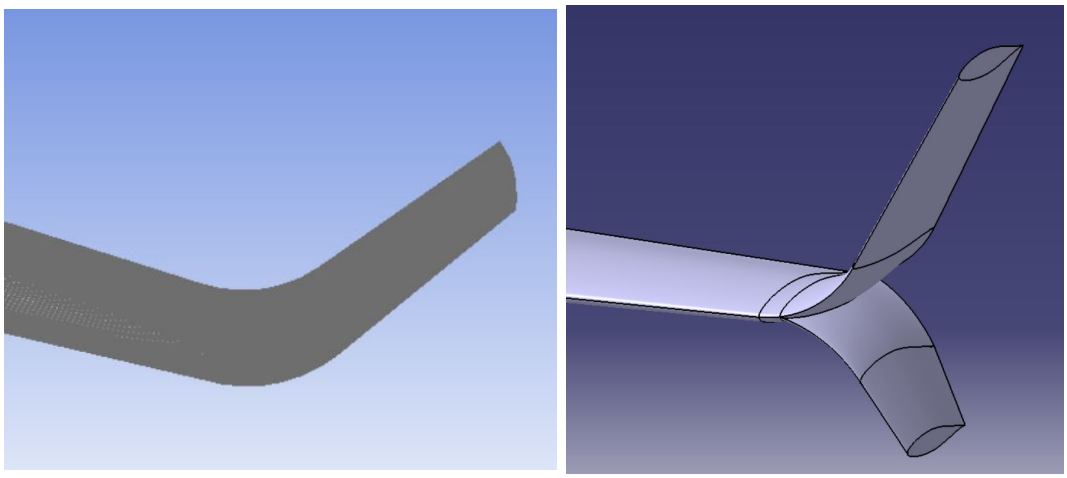

Figure 4.16: Blended Winglet at 60º and Double Winglet at 60º

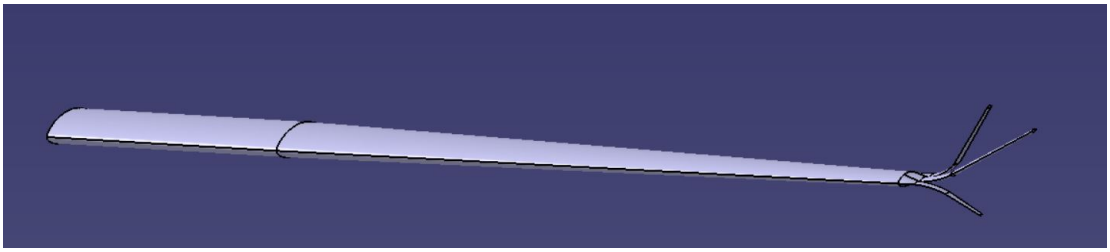

Figure 4.17: Multi-winglet final design

Chapter 5

CFD Analysis

5.1 CFD basics and applications

Computational Fluid Dynamics, or CFD, is a branch of fluid dynamics that attempts to solve the equations governing fluid motion numerically. To this extent, the flow domain is typically discretized, dividing the fluid whose behavior will be analyzed in a number of discrete elements. The governing equations of fluid mechanics -state equations and conservation laws- are then applied to each of the elements of the grid formed in this way.

There are two approaches to fluid dynamics problems: the Lagrangian approach, which traces every fluid particle throughout the flow, and the Eulerian approach, which considers the fluid as a continuous *field* where properties can be defined at every point independently of the particular fluid particles flowing past it at every moment in time, and conservation laws are applied on given control volumes defined in the flow. The wide majority of CFD applications employ the latter.

For a three-dimensional control volume in the fluid flow, the conservation laws are defined by the three Navier-Stokes equations, referring to the conservation of mass, momentum, and energy, respectively. The continuity equation, 5.1, indicates that the net outflow of mass through the surface surrounding the volume must be equal to the decrease of mass within it; the momentum equation 5.2 states that the rate of change in time of the momentum in the control volume equals that of the net force exerted on it, due to pressure, viscous, and body forces; and the energy equation 5.3 simply remarks that the change in the total energy of the control volume in time must amount to the combination of the change in added heat and the change in work done in the system.

$$\frac{\partial \rho}{\partial t} + \nabla \cdot (\rho V) = 0 \tag{5.1}$$

$$\frac{\partial \vec{u}}{\partial t} + \vec{u} \cdot \nabla \vec{u} = -\frac{1}{\rho}\nabla p + \nu \nabla^2 \vec{u} + \frac{1}{3}\nu \nabla (\nabla \cdot \vec{u}) + \vec{g} \tag{5.2}$$

$$\rho \frac{Dh}{Dt} - \frac{Dp}{Dt} = \nabla \cdot (k \nabla T) + \phi \tag{5.3}$$

The three equations are shown here in their differential form, and the expression for the conservation of energy, 5.3, corresponds to its enthalpy formulation; many more are found in literature. There are a number of ways in which they may be simplified; for instance, if the viscous terms are sufficiently small when compared to the pressure terms, they might be neglected altogether, yielding the inviscid, or *Euler*, equations. The Navier-Stokes equations are typically combined with a state equation, which defines the relationship between fluid variables such as pressure or density. When assuming that the fluid is a perfect gas, this equation becomes:

$$p = \rho RT \tag{5.4}$$

where R is the specific gas constant [2].

The division of the fluid domain in discrete elements requires, as well, a discretization of the governing equations of the flow; this will yield a particular formulation of each conservation law for every element or node in the domain, thus creating a system of equations whose solution corresponds to the value of the flow variables at every given point throughout the field. There are three main approaches to this process typically employed in numerical methods:

- Finite difference method (FDM): based on Taylor-expanding the governing equations, it requires the functions to be continuous and differentiable and can only be employed for very simple geometries.
- Finite element method (FEM): The equations are approximated by modal functions which can be differentiated analytically. It is typically employed for structural analysis applications, as it becomes costly for the large number of cells typically present in CFD.
- Finite volume method (FVM): It is the approach usually employed in computational fluid dynamics applications, and it is based on establishing a series of control volumes surrounding the discrete nodes defined throughout the domain. Conservation laws are then applied to every control volume. Although it is not as flexible in terms of geometry as FEM, it provides a simpler, far less costly approximation particularly useful for external flows in large domains.

Once both the governing equations of the flow and the numerical approach have been defined for a particular problem, there are three main stages to CFD techniques:

- Pre-processing: it includes the definition of the geometry, the generation of the grid or mesh, the establishment of the boundary conditions that will be required to solve the discretized system of equations, the definition of the fluid properties, and the selection of the physical phenomena which will be considered in the analysis (such as viscous effects, heat generation, etc).

- Solving: it refers to the process of approximating the unknowns, discretizing the given expressions, applying the boundary conditions described in previous steps, and obtaining the solution of the system of equations for every node in the domain.

- Post-processing: once a numerical solution is found, post-processing comprises the visualization, display, and analysis of the data obtained.

5.2 Software employed

The CFD simulations required for this project were performed exclusively with an academic version of the commercial ANSYS™ Workbench product suite, including its geometry and meshing tools and the ANSYS FLUENT™ fluid flow simulation software. ANSYS provides a number of computational tools widely used in engineering industries nowadays, particularly in the field of aeronautics, with customers including key automobile and aerospace manufacturers throughout the world.

ANSYS FLUENT™ employs a finite volume method algorithm with different options regarding segregation or coupling of the flow variables. It provides a number of turbulence models, including both Reynolds-Average Navier-Stokes (RANS), large eddy simulation (LES), and hybrid (RANS-LES) approaches; these are combined with a variety of near-wall treatments for wall-bounded turbulent flows, among them enhanced wall treatments and standard, scalable, and non-equilibrium wall functions. It contains solvers for two-dimensional, three-dimensional, and axisymmetric flows, for both stationary and moving reference frames, and can process both single-phase and multiphase flows. These, along with the number of options for spatial and temporal discretization and the availability of pressure-based and density-based solvers, were among the many advantages presented by this software when compared to similar tools existing in the market.

As for the geometry and meshing tools, they were considered particularly suitable for the purposes of this work given their versatility. The geometry editor accepts a variety of inputs, including both standard (step, igs) and product-specific (CATpart) formats, and it can easily perform 3D boolean operations and geometry repairs. The meshing tool, on the other hand, allows for the configuration of a significant number of mesh parameters, including the creation of spheres of influence, body sizings, and inflation layers, and provides tetrahedral, hexahedral, hybrid, and quad-cell structured and unstructured grids.

Lastly, the post-processing of the results obtained was performed in CFD-Post: a simple, intuitive program from the ANSYS suite which allows for the visualization and display of flow variables, as well as computations concerning fluid properties and mesh statistics.

5.3 Cases studied

Simulations in ANSYS FLUENT^{TM} were carried out for every geometry described in the previous chapter, for two particular cases:

- Cruise conditions: based on the cruise conditions described in [16] for the CN235 aircraft, the wing was modeled as if flying at an altitude of 4,575m with velocity $U_\infty = 125$m/s.
- Takeoff conditions: In an attempt to recreate a state similar to takeoff, in which winglets and wingtip devices in general are commonly thought to be most effective, the angle of attack was set to $\alpha = 10^o$, with a velocity $U_\infty = 50$m/s at sea level standard conditions.

The reference density ρ, pressure p, and dynamic viscosity μ were found through the International Standard Atmosphere (ISA) model, assuming a null temperature deviation from the reference values (ISA+0). The angle of attack for cruise conditions was found through a vortex lattice method algorithm implemented in MatLab, as described in chapter 6. The resulting flight conditions for every case are gathered in Table 5.1

Case	$U_\infty(m/s)$	α (°)	h (m)	ρ (kg/m^3)	p (Pa)	T (°C)	μ (kg/m s)	Mach
Cruise	125	4.26	4575	0.77084	57184	-14.72	$1.6423 \cdot 10^{-5}$	0.388
Takeoff	50	10	0	1.225	101325	15	$1.7894 \cdot 10^{-5}$	0.1469

Table 5.1: Flight conditions for the CFD simulation cases

A total of 44 simulations were performed, corresponding to the short, long, blended, double, and multi winglets described in chapter 4; the reference case of the wing without any wingtip devices; the wing with the raked wingtip; and the wingtip fences.

The Reynolds numbers of the flow around the wing, considering the mean aerodynamic chord (MAC) of the basic wing as the characteristic length, were:

- $Re_{cr} = 1.4615 \cdot 10^8$ for cruise conditions.
- $Re_{to} = 8.2801 \cdot 10^7$ for takeoff conditions.

As both Reynolds numbers were considerably high, the flow over the wings was expected to be fully turbulent, requiring the use of an adequate turbulence model and near-wall approach.

5.4 Definition of the fluid domain geometry

The size of the fluid domain was determined by the need to model a flow as similar to that of the open atmosphere as possible, while keeping in mind computational limitations. These considerations led to the definition of a 24x12x22m enclosure surrounding the wing; taking the chord at the wing root as a reference, it corresponded to a distance of

$2C_{root}$ before the leading edge, $6C_{root}$ behind the trailing edge, $2C_{root}$ above and below the wing and $2C_{root}$ beyond the wing tip. The inner wall of the enclosure, corresponding to the wing root, was defined as a plane of symmetry in order to simplify the simulation, ensuring that employing only the wing semi-span would yield results akin to those of the whole wing within a much smaller domain. The resulting geometry can be observed in figure 5.1.

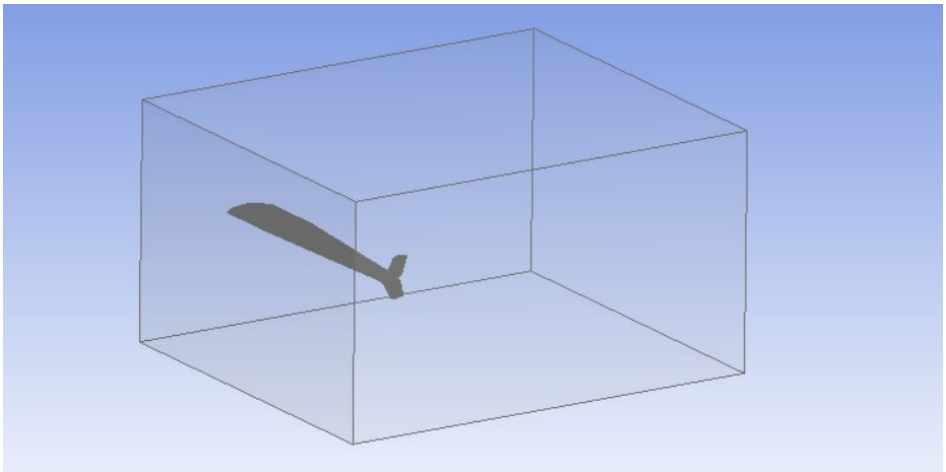

Figure 5.1: Enclosure for the wing + double winglet. ANSYS geometry editor

In order to include a more refined region in the mesh immediately surrounding the wing, a smaller body was defined with dimensions 6x15x19m, corresponding to C_{root} before the leading edge, $4C_{root}$ behind the trailing edge, C_{root} above and below the wing, and C_{root} beyond the wing tip. The fact that the domain was significantly larger behind the trailing edge of the wing was due to the need to evaluate the behavior of the flow in the wake left behind the wing, where the trailing vortices would appear. In front of the leading edge, however, the distance was selected as the minimum required to provide a homogeneous flow at the desired angle of attack. Although, ideally, the flow domain might have been considerably larger, thus eliminating all possible interferences, this would increase the computational time to an unreasonable extent.

5.5 Mesh geometry and sizing

Once the geometry of the fluid domain was defined, it was necessary to decide on the mesh parameters. As mentioned in Section 2, ANSYS FLUENT provides a variety of options ranging from the geometry of the basic grid elements to the addition of local refinements on chosen regions. For the three-dimensional mesh required in this case, an unstructured grid with tetrahedral elements was chosen. Although more accurate results can be achieved for the same number of elements with a hexahedron-based mesh, the tetrahedral configuration provided greater versatility for successive mesh adaptations,

as well as suitability for the more complicated geometries. For all cases, the mesh was defined through the same parameters, gathered here as presented in the ANSYS meshing tool interface:

- **Sizing**: the mesh was refined based on curvature, in order to increase the number of cells in the immediate surroundings of the wing. The relevance center was chosen as medium and the curvature normal angle set to 12^o instead of the default 18^o. The minimum element size was set to 0.005m, while both the maximum element size and the maximum face size chosen as 0.80m. Medium smoothing, slow transition, and the recommended growth rate of 1.2 completed the general setup, with the remaining parameters set as default.

- **Inflation**: in order to obtain an accurate model of the fluid flow near the surface of the wing, an inflation layer was added to the mesh. Its dimensions were conditioned by the characteristics of the boundary layer, whose behavior in the turbulent regime might be the cause of some computational problems.

  The boundary layer, defined as the thin layer of fluid flow over the surface of the submerged body where viscous effects cannot be ignored even in inviscid flow, varies significantly over the surface of a wing or airfoil, presenting an initial laminar region, a later turbulent region, and eventual separation. It is this turbulent region, or the particular approach to near-wall turbulence modeling employed in each simulation, what determines the local Reynolds number y^+ and, in turn, the dimensions of the inflation layer.

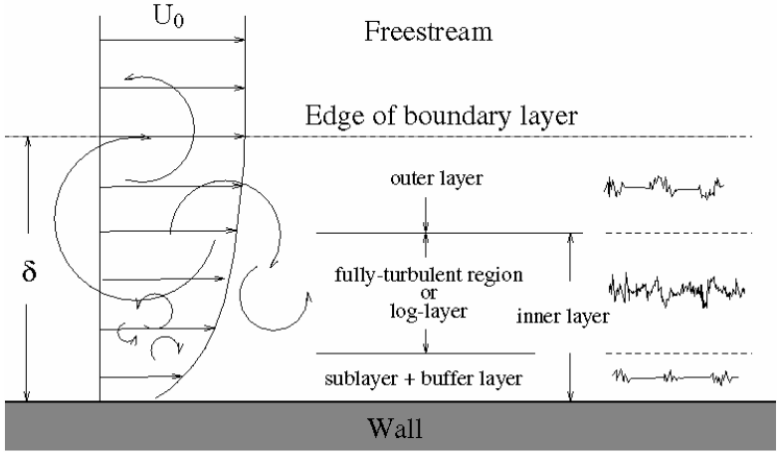

Figure 5.2: Subdivisions of the turbulent boundary layer [34]

As found in Cebeci [5], it is typically assumed that a turbulent boundary layer can be divided in two main regions: an inner region, comprising 10-20% of the boundary layer's thickness, and the remaining outer region. The inner region is, in turn, formed by two differentiated regions: a viscous sublayer, where the velocity

profile is conditioned by viscous, unsteady, non-uniform wall shear forces, and a fully turbulent region, separated by a transitional region or buffer layer. According to the so-called *law of the wall*, the velocity profile is given by $u^+ = y^+$ in the viscous sublayer, and $u^+ = \frac{1}{k}ln(y^+) + B$ in the turbulent or logarithmic layer, where k and B are constants. The non-dimensional wall distance, y^+, is given by

$$y^+ = \frac{u_\tau y}{\nu} \tag{5.5}$$

where ν is the kinematic viscosity of the fluid, y the distance from the wall, and u_τ is the friction velocity given by the wall shear stress τ_w and the density ρ as

$$u_\tau = \sqrt{\frac{\tau_w}{\rho}} \tag{5.6}$$

Acceptable values of y^+ for the height of the first inflation later in near-wall turbulence modeling range from 11.06 to 300 in Fluent, in order to set this layer on the fully turbulent region of the inner boundary layer. Considering these requirements, and aiming for an approximate y^+ value of 50, the reference height of the first inflation layer was computed from the skin friction coefficient, C_f, as:

$$C_f = \frac{0.058}{Re^{0.2}} \tag{5.7}$$

approximating the flow over the airfoil to a turbulent boundary layer over a flat plate, and

$$\tau_w = \frac{1}{2}\rho U_\infty^2 C_f \tag{5.8}$$

for the wall shear stress. The Reynolds number employed for the friction coefficient computation considered the mean aerodynamic chord (MAC) as its characteristic length. This yielded a reference first inflation layer height of $y = 0.0005$m, which was employed both for an initial estimation and as a definitive value once the mesh generated in this way was proven satisfactory. A total of ten inflation layers with prismatic elements were added to the mesh, with a growth rate of 1.2, and over the entire surface of each wing.

- **Body sizing**: In order to obtain a better grid refinement in the region surrounding the wing, the additional body described in the previous section was employed to define a new sizing. Within this region, the element size was limited to 0.1m, with the growth rate set to 1.2 and the minimum element size established as 0.005m, as in the rest of the domain.

The parameters described here were assigned the same values for all the wing + winglet cases considered, in an attempt to eliminate all possible differences between

simulations which might appear due to dissimilarities in the grid. An example of the final mesh geometry can be observed in figures 5.3 to 5.5.

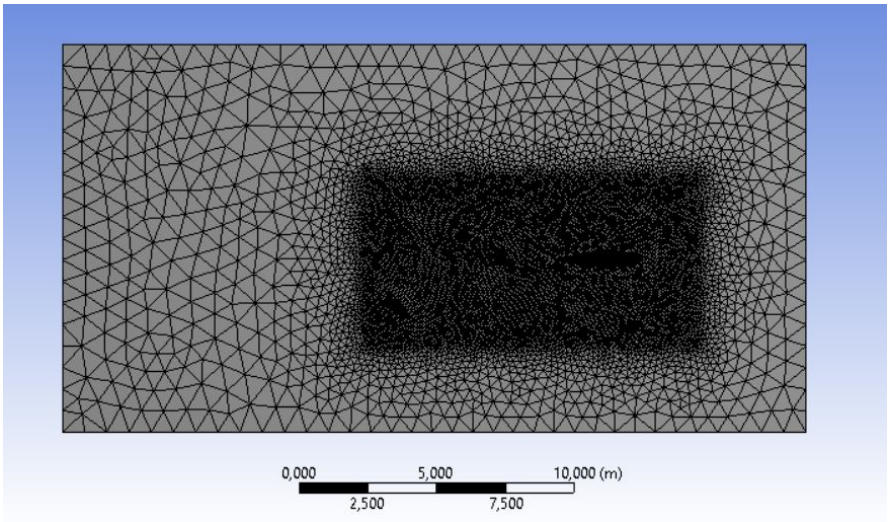

Figure 5.3: Final mesh as seen from the plane of symmetry

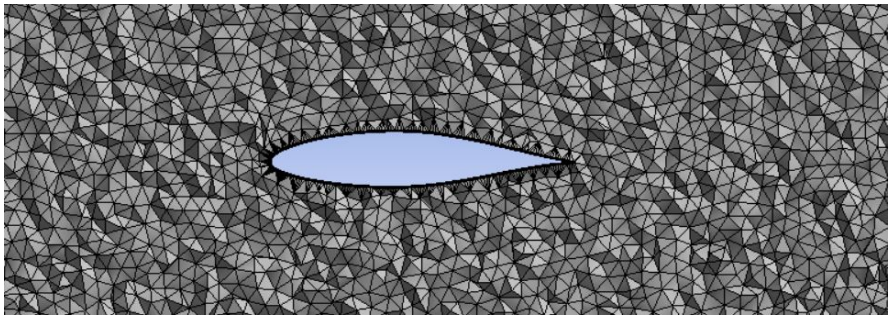

Figure 5.4: Section plane of the three-dimensional mesh surrounding the wing

Validation of the mesh was performed through a series of standard parameters. The number of nodes and elements was limited by the computational power available, while the y^+ value was monitored for every mesh in order to ensure the validity of the inflation layer. The results for every case considered are shown here in Table 5.2. Two more simulations for a more refined mesh, covering a larger domain of 60x20x20m, and refined in proximity and curvature, were run; as an difference of less than 1% was observed between the new and original results, the coarser mesh was employed to reduce the computational time.

As it can be observed in the table above, three main parameters were employed to determine the quality of the mesh, as common in Fluent analyses:

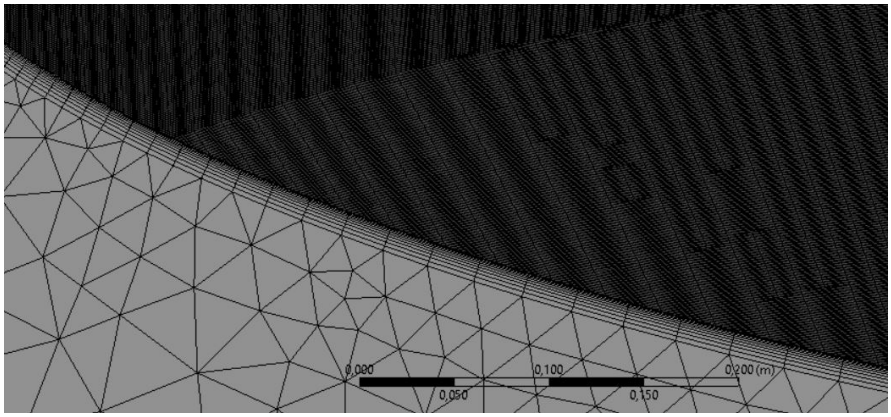

Figure 5.5: Inflation layer near the leading edge of the wing. Detail

Case	**Elements**	**Mean AR**	**Mean OQ**	**Mean Skewness**	y^+
Basic	12,286,578	7.89	0.8324	0.2484	[12.81, 141.60]
Short 00°	14,062,587	3.89	0.8698	0.2081	[19.76, 143.90]
Short 15°	14,116,468	3.89	0.8702	0.2077	[22.33, 142.30]
Short 30°	12,949,636	8.02	0.8320	0.2491	[15.51, 142.00]
Short 45°	13,008,571	8.00	0.8322	0.2492	[16.27, 142.40]
Short 60°	12,956,746	8.05	0.8322	0.2491	[22.57, 143.10]
Short 75°	13,689,766	3.87	0.8694	0.2082	[19.18, 143.30]
Long 00°	14,149,190	7.79	0.8319	0.2493	[22.63, 137.50]
Long 15°	14,021,2717	3.90	0.8697	0.2077	[32.22, 142.20]
Long 30°	13,808,011	7.94	0.8308	0.2508	[16.96, 145.10]
Long 45°	14,181,874	7.81	0.8317	0.2500	[21.55, 139.20]
Long 60°	13,897,993	7.94	0.8307	0.2511	[15.49, 143.90]
Long 75°	13,958,297	3.92	0.8691	0.2034	[22.35, 144.20]
Blended 30°	13,729,196	8.00	0.8299	0.2507	[17.28, 142.30]
Blended 45°	13,799,277	7.95	0.8298	0.2508	[17.89, 140.70]
Blended 60°	13,848,704	7.88	0.8298	0.2510	[20.22, 142.10]
Double 30°	14,620,949	4.26	0.8694	0.2104	[22.33, 143.30]
Double 45°	14,309,833	4,05	0,8680	0.2109	[12.17, 143.50]
Double 60°	14,647,909	4.08	0.8681	0.2112	[18.43, 145.30]
Raked	13,697,063	3.87	0.8699	0.2078	[20.04, 140.70]
Fence	14,684,132	4.05	0.8709	0.2085	[24.11, 144.90]
Multi	17,278,137	4.51	0.8674	0.2177	[16.30, 133.10]

Table 5.2: Mesh quality parameters for all cases

- **Aspect Ratio**: for a mesh formed by tetrahedral elements, it is calculated for each cell as the radius ratio of the circumscribed to inscribed circle. Although ideally it should be as close to one as possible, values below ten can be considered acceptable. The high average values shown in Table 5.2 present some influence from the elongated prismatic elements employed in the inflation layer, and lie, overall, within a reasonable range.

- **Orthogonal Quality**: it is a metric for cell geometry calculated as the minimum

value between:

– The scalar product of the area vector and a vector joining the centroid of the element to that of that face, normalized:

$$\frac{\vec{A_i} \cdot \vec{f_i}}{|\vec{A_i}||\vec{f_i}|} \tag{5.9}$$

– The scalar product of the area vector of a face and a vector joining the centroid of the element to that of an adjacent face, normalized:

$$\frac{\vec{A_i} \cdot \vec{c_i}}{|\vec{A_i}||\vec{c_i}|} \tag{5.10}$$

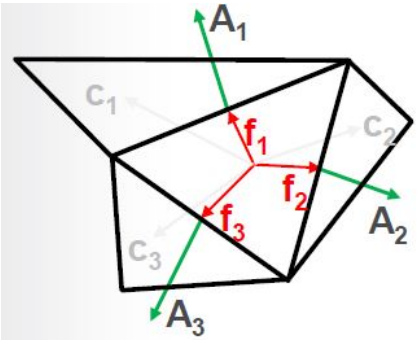

Figure 5.6: Vectors employed in the orthogonal quality computation [29]

computed for each face i. Values of orthogonal quality range from 0 to 1, with 0 indicating the worst possible quality and 1 being the ideal. Intermediate values in the range of [0.70, 0.95] are considered indicators of a very good quality. As shown in figure 5.7, the standard deviation was quite low, with typical values of 0.01, and all elements were located above the acceptable minimum of 0.10.

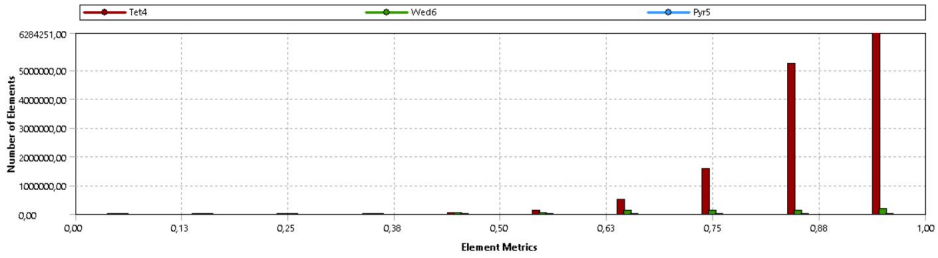

Figure 5.7: Orthogonal quality for the wing+double winglet at 45º

- **Skewness**: for tetrahedral elements, it is computed as the deviation of the cell from an equilateral cell of equal volume, as:

$$\frac{V_{equivalent} - V_{actual}}{V_{equivalent}} \tag{5.11}$$

As the minimum deviation from the equivalent, optimal cells is preferred, the values for an ideal mesh in terms of skewness would tend to zero. Values presented in this table fall in the range of 'very good' (0.25-0.50) or 'excellent' (0-0.25) according to ANSYS standards (source). Figure 5.8 shows the typical distribution of skewness values for the mesh elements, which presented a standard deviation of approximately 0.12 for all cases.

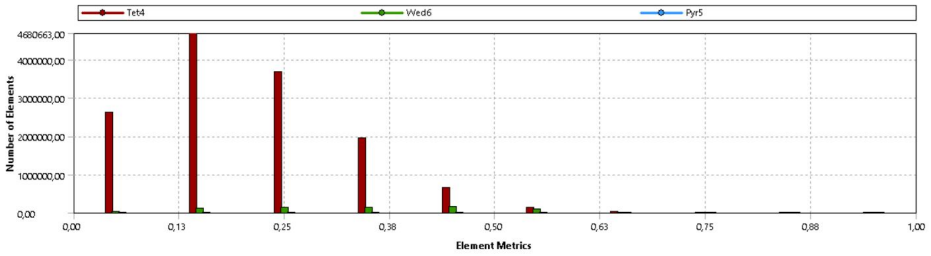

Figure 5.8: Skewness for the wing+double winglet at 45°

The range of y^+ values shown in the table was calculated in CFD-Post at the first inflation layer height, according to the method described in equations 5.5 to 5.8.

5.6 Solver setup

After an adequate mesh was generated for every wing, as described above, the parameters governing the simulation were established in ANSYS Fluent. Each wing was analyzed for the two cases mentioned in section 3, at conditions similar to those found at the cruise and takeoff flight phases. The simulation setup is described here in detail, distributed as it appears on the ANSYS Fluent interface:

- **General**: A density-based solver was chosen for both cases. Although the flight Mach number were quite low and compressibility effects are typically not considered at $M \leq 0.3$, they could not be completely discarded for cruise conditions. The velocity formulation was chosen as absolute, with steady flow conditions. As usual in aerodynamic flows, the Froude number, describing the ratio of flow inertia to gravity effects, was large for both cases, such that:

$$Fr = \frac{U_\infty}{\sqrt{g l_c}} >> 1 \tag{5.12}$$

  employing the mean aerodynamic chord as a characteristic length, and thus the effects of gravity could be disregarded.

- **Models**: Since the aim of this study did not consider heat transfer effects, the energy equation 5.3 was not included in the analysis. The turbulence model employed was the realizable $\kappa-\epsilon$ model with non-equilibrium wall functions (NEWF).

Many turbulence models are *statistical*: as computational power rarely allows for a detailed simulation of the behavior of the flow in turbulent regime, they attempt to emulate the effects of turbulence by considering the variables to have a time-averaged and a time-fluctuating component, such that a variable U would become $U = \bar{U} + u$, with

$$\bar{U} = \frac{1}{\Delta t} \int_{t}^{t+\Delta t} U dt \tag{5.13}$$

This assumption leads to the modification of the Navier-Stokes equations, creating the Reynolds-Averaged Navier-Stokes (RANS) equations. In this way, the continuity and momentum equations become:

$$\frac{\partial \rho}{\partial t} + \nabla \cdot (\rho \vec{U}) = 0 \tag{5.14}$$

$$\frac{\partial \rho \vec{U}}{\partial t} + \nabla \cdot (\rho \vec{U} \wedge \vec{U}) = \nabla \cdot (\tau - \rho \vec{u} \wedge \vec{u}) + \vec{S}_M \tag{5.15}$$

where the time-fluctuating turbulent terms -the Reynolds stresses and Reynolds flux- indicate the increased mixing action of the convective transport terms due to turbulence. The time-fluctuating components, then, become additional variables in these expressions, requiring further equations describing their behavior.

Both the standard and realizable $\kappa - \epsilon$ models belong to the so-called two-equation RANS models, since they incorporate two additional transport equations for the turbulent kinetic energy κ and its dissipation rate ϵ. These two variables allow for the computation of the turbulent velocity and length scale, which yield, in turn, the turbulent viscosity. For the standard $\kappa - \epsilon$ model:

$$\mu_t = C_\mu \rho \frac{\kappa^2}{\epsilon} \tag{5.16}$$

where C_μ is a constant, and the two additional equations become:

$$\frac{\partial (\rho \kappa)}{\partial t} + \nabla \cdot (\rho \vec{U} \kappa) = \nabla \cdot [(\mu + \frac{\mu_t}{\sigma_k}) \nabla \kappa] + P_k - \rho \epsilon \tag{5.17}$$

$$\frac{\partial (\rho \epsilon)}{\partial t} + \nabla \cdot (\rho \vec{U} \epsilon) = \nabla \cdot [(\mu + \frac{\mu_t}{\sigma_\epsilon}) \nabla \epsilon] + \frac{\epsilon}{\kappa} (C_{\epsilon 1} P_k - C_{\epsilon 2} \rho \epsilon) \tag{5.18}$$

where $C_{\epsilon 1}$, $C_{\epsilon 2}$, σ_k, and σ_ϵ are constants, and P_k is a source term indicating the turbulence production due to viscous and buoyancy forces.

As these models assume the turbulent flow to consist of unsteady, small eddies in constant change, the Reynolds stresses are considered to be proportional to the

mean velocity gradients through the gradient diffusion hypothesis, which establishes a relationship analogous to that found between the stress and strain tensors in laminar flow. In a similar way, the Reynolds fluxes are related to the mean scalar gradient of each variable through the eddy diffusivity.

The realizable $\kappa - \epsilon$ model presents some improvements when compared to the standard $\kappa - \epsilon$: it provides a better performance for flows with strong adverse pressure gradients or boundary layer separation, flows with a strong streamline curvature, and flows where rotation and recirculation are significant. Mathematically, it employs the same turbulent kinetic energy equation as the standard model, a slightly modified turbulent dissipation rate equation, and a variable C_μ computed from the flow properties to calculate the turbulent viscosity. Although it is computationally more time-consuming, it was considered that it would be more suitable to the geometries and flow regimes studied in this work.

There are two main approaches to modeling the turbulent flow in the vicinity of walls: wall functions and near-wall modeling. While the latter is based on including the effects of viscosity in the viscous and buffer sublayers of the turbulent boundary layer in the governing equations, wall functions provide an estimate of the effects of the wall proximity to avoid increasing the complexity of the mathematical model. For wall functions approaches, such as that employed in this work, inflation layers become particularly important, and y^+ values must be ensured to lie on the established range $y^+ \in (11, 300)$.

Standard wall functions are based on the work of Launder and Spalding, and, as described in the ANSYS Fluent theory guide [30], they provide a series of approximations for key flow variables on the near-wall region. The law-of-the-wall for mean velocity, for example, is formulated as:

$$U^* = \frac{1}{\kappa} ln(Ey^*) \tag{5.19}$$

Where U^* and y^* are the dimensionless velocity and distance from the wall, respectively, and κ and E are constants. For $k - \epsilon$ models, the turbulent kinetic energy is solved with the boundary condition $\frac{\partial k}{\partial n} = 0$ at the wall, and assuming that the dissipation rate ϵ is equal to the production of k in equilibrium.

Non-equilibrium wall functions provide some improvements over the standard wall functions approach. They incorporate more detailed considerations for turbulent kinetic energy in the wall-neighboring cells, as well as including pressure-gradient effects in the log-law for mean velocity. Overall, non-equilibrium wall functions yield a better performance for flows where boundary layer separation and adverse pressure gradients might be important. When combined with the realizable $k - \epsilon$ model, they provided a solid, reliable turbulence model for the problem at hand.

- **Materials**: Air was chosen as the default material for the whole domain. Its properties were modified for every case to account for variations with altitude

according to the International Standard Atmosphere model, as shown in section 3.

- **Boundary conditions**: The characteristics of every surface in the fluid domain were defined through a default boundary condition, as follows:
  - The surface of the enclosure closer to the leading edge of the wing was defined as the **velocity inlet**, with a uniform velocity equal to U_∞ for every case oriented along the direction defined by the angle of attack α. The turbulent kinetic energy was set to 1% and the turbulent viscosity ratio established as 5%.
  - The opposite surface, beyond the trailing edge, was defined as a **pressure outlet**; its reference pressure was set as equal to the atmospheric value, while its turbulent kinetic energy and turbulent dissipation values were established as 5%.
  - The remaining external surfaces of the enclosure were defined as a **symmetry**, that is, a stationary wall for which wall shear is fixed as zero.
  - The internal boundary of the fluid domain, adjusted to the shape of the wing, was defined as a stationary, non-slip **wall**.
- **Solution methods**: Although a first-order upwind scheme was employed to facilitate convergence of the numerical solution, a second-order upwind scheme would probably be desirable for subsequent research.
- **Monitors**: The reference value of the residuals to determine convergence was set to 10^{-5} for all variables. The drag and lift forces were defined as directed in the parallel and perpendicular directions to the fluid flow, respectively, as determined by the angle of attack α.

After all these parameters were set, the simulations were run for approximately 3000 iterations until sufficiently small residual values were reached.

5.7 Post-processing

The analysis of the results obtained in the Fluent simulations focused on the key indicators of the presence and modification of wingtip vortices:

- Forces: lift and drag forces were obtained directly from CFD Post. Their non-dimensional coefficients, C_D and C_L, were calculated employing the planform area projected on the plane of fluid motion as defined by the angle of attack α.
- Contours of flow variables: The pressure, velocity, and vorticity were mapped through the domain in order to study the presence of the wingtip vortices on the wake and the changes on their behavior caused by the incorporation of wingtip devices.

- Performance parameters: The aerodynamic efficiency or lift-to-drag ratio, L/D, was the main parameter considered to analyze the effect of wingtip devices, as described in later chapters.
- Mesh quality: values of y^+ were monitored for every simulation in order to ensure a valid geometry for the inflation layer.

The results of the Fluent simulations, as well as their similarity to those found through other methods, will be presented later in this work.

5.8 Parasite drag estimation

As it has been mentioned in previous chapters, the drag coefficient of a general aircraft is typically assumed to follow a parabolic model, such that it can be split into a *parasitic* component C_{D_0}, related to the aircraft geometry and surface characteristics, and an *induced* component, directly proportional to the square of the lift coefficient. Since the role of wingtip devices is almost exclusively restricted to reducing the induced drag coefficient, it was deemed appropriate to perform a number of CFD simulations aiming to obtain the parasite drag coefficient for a number of wings. This would help to understand which percentage of the drag force was due to parasite drag in different flight conditions, and whether the presence of wingtip devices caused a significant increase in this coefficient.

The simplest way to obtain an estimation of the parasite drag coefficient was to run a CFD simulation for zero-lift conditions, so that the induced drag contribution to the total drag would disappear. For this purpose, and given that the lift coefficient depends exclusively on the angle of attack α, such that:

$$C_L = C_{L_\alpha} \cdot \alpha + C_{L_{\alpha=0}} \tag{5.20}$$

the lift coefficients obtained at takeoff and cruise conditions were linearly interpolated for every wing geometry to obtain the lift coefficient slope, C_{L_α}, and the lift at zero angle of attack, $C_{L_{\alpha=0}}$. Although the C_L/α curve is typically far more complex, for low angles of attack it can be approximated as linear, as long as the angle of attack does not approach the stall limit. Once these values were calculated, zero-lift simulations were run for the basic wing, wing+long winglet at $\Theta = 60^o$, and wing+double winglet at $\Theta = 30^o$ for cruise conditions, and basic wing at takeoff conditions.

Chapter 6

VLM and 3D Panel Method

6.1 Numerical Methods in Aerodynamics

The first analysis of the effect of wingtip devices on wing performance was based on a panel method, while the computation of the cruise angle of attack employed for the computational fluid dynamics analysis was conducted through a vortex lattice method. Both of them are derived directly from the conclusions of potential flow theory applied to aerodynamics, and, although more complex numerical methods -such as those described in the following chapters- are typically preferred, they can provide an initial estimation of the aerodynamic forces and moments acting on a given body.

The term "potential flow" refers to a particular fluid flow for which the velocity may be expressed as the gradient of a "velocity potential", ϕ, so that $\vec{V} = u\vec{e}_x + v\vec{e}_y + w\vec{e}_z = \nabla\phi$. For the fluid flow over a body to be considered potential, its governing equations must undergo two sets of simplifications. The first one transforms the Navier-Stokes equations [17] into the Euler equations when the following conditions are fulfilled:

- High Reynolds number, $Re >> 1$, indicating that viscous forces can be considered negligible when compared to pressure terms.
- Negligible body forces, with Froude number $Fr >> 1$: the effects of gravity can be neglected.
- Adiabatic flow, with Prandtl number of order 10^0, $Pr \sim O(1)$.

In addition to these characteristics, a potential flow must be:

- Steady, $\frac{\partial\phi}{\partial t} = 0$; the characteristics of the flow must not be affected by time.
- Irrotational: the vorticity, or curl of the velocity, must be null in the whole domain, such that $\vec{\omega} = \nabla \wedge \vec{V} = 0$.

It these requirements are met, the continuity equation -conservation of mass- becomes the Laplace equation for the velocity potential, such that:

$$\nabla^2 \phi = 0 \tag{6.1}$$

and the potential itself can be expressed as the sum of the contributions of several solutions of the Laplace equation, or singularity elements. Three main point singularities are typically employed for both two-dimensional and three-dimensional flows:

- **Sources**: elements from which the fluid flow springs equally in all directions, with a potential $\phi = -\sigma/(4\pi r)$ in a spherical coordinate system. σ refers to the volumetric rate at which fluid is introduced; it is positive for a source and negative for a sink.
- **Doublets**: they can be considered a combination of a source and a sink of equal strengths σ at a distance $\vec{l}$, such that $\vec{l} \to 0$, $\sigma \to \infty$, and $\vec{l}\sigma \to \vec{\mu}$, with the doublet strength $\vec{\mu}$ thus directed along the source-to-sink direction or doublet axis. In a spherical coordinate system, their potential is defined as $\phi = -\vec{\mu} \cdot \vec{r}/(4\pi r^3)$.
- **Vortices**: the velocity due to these elements is purely tangential in a polar coordinate system, with the velocity potential given by

$$\phi = \frac{-\Gamma}{2\pi}\theta + C \tag{6.2}$$

  where Γ refers to the circulation around the vortex.

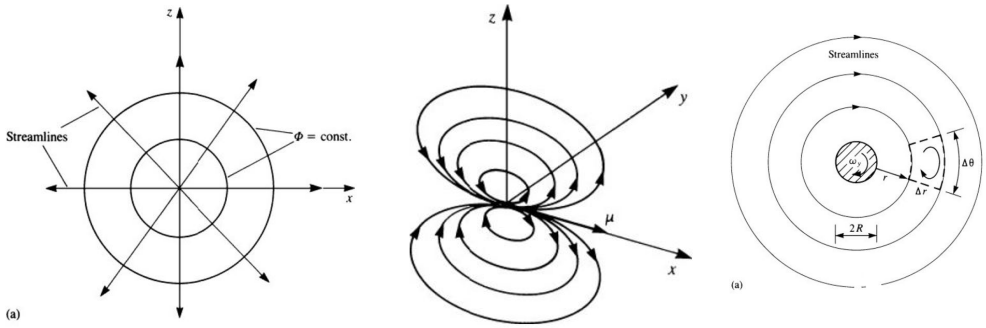

Figure 6.1: Common singularity elements: source (left), doublet, and vortex [17]

In three-dimensional applications, singularity elements are typically assumed to be distributed throughout the surface of the given body, and are considered to present a simple -usually quadrilateral- geometry and constant, unknown strength.

- A three-dimensional quadrilateral source element with a strength σ per area, located at (x_0, y_0, z_0) produces a contribution to the total potential at a point (x,y,z) of:

$$\phi(x, y, z) = \frac{-\sigma}{4\pi} \int_S \frac{dS}{\sqrt{(x - x_0)^2 + (y - y_0)^2 + (z - z_0)^2}} \tag{6.3}$$

- Similarly, a three-dimensional quadrilateral doublet element with a strength μ, oriented in the z direction, and located at $(x_0, y_0, 0)$ causes, at point (x, y, z), a velocity potential:

$$\phi = \frac{-\mu}{4\pi} \int_S \frac{z dS}{[(x-x_0)^2 + (y-y_0)^2 + z^2]^{3/2}} \tag{6.4}$$

- It has been shown [17] that the velocity induced by a vortex ring with circulation Γ at any point (x, y, z) of a fluid flow is equal to that induced by a doublet element with strength μ located at the same point (x_0, y_0, z_0), given that $\Gamma = \mu$. This vortex-doublet analogy is widely employed to model doublet distributions through arrangements of vortex rings, leading to the horseshoe-vortex wing model explained below.

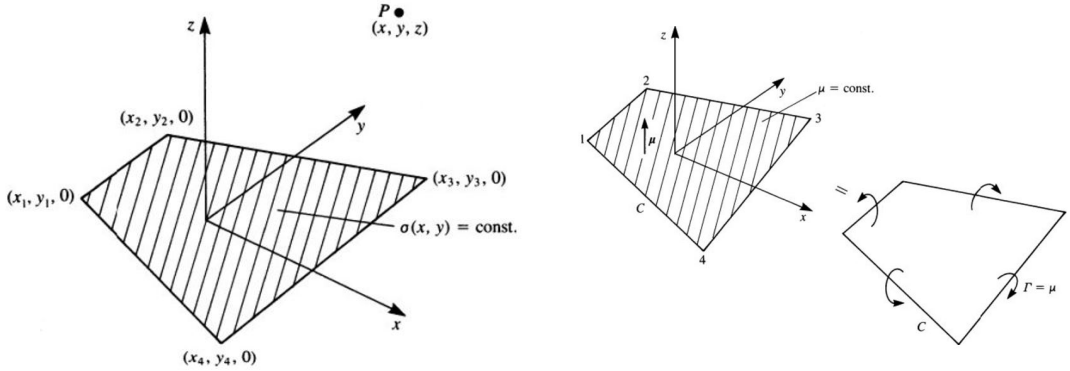

Figure 6.2: Quadrilateral source element (left) and quadrilateral doublet element (right) with its vortex ring equivalent [17]

Both the three-dimensional panel method and the vortex lattice method are based on Green's identity,

$$\phi^*(x,y,z) = \frac{1}{4\pi} \int_{wing} (\frac{1}{r}\frac{\partial \phi}{\partial n} - \phi \frac{\partial}{\partial n}\frac{1}{r}) dA + \frac{1}{4\pi} \int_{wake} -\phi \frac{\partial}{\partial n}\frac{1}{r} dA \tag{6.5}$$

which establishes that the perturbation potential caused by a given aerodynamic body can be modeled as a combination of three elements:

- A distribution of doublets over the wing surface.
- A distribution of sources over the wing surface.
- A distribution of doublets on the wake trailing behind the body.

to which the required boundary conditions are added: no fluid flow should be able to cross the solid boundary of the body, the perturbation potential must vanish in

the far field where $r \to \infty$, and the fluid velocity at the upper and lower wing surfaces must become equal at the trailing edge (Kutta condition). Taking these considerations into account, the wing and wake can then be divided in a number N of panels defined by collocation points k, on which the selected singularities of unknown strength that will define the perturbation potential of the body are located.

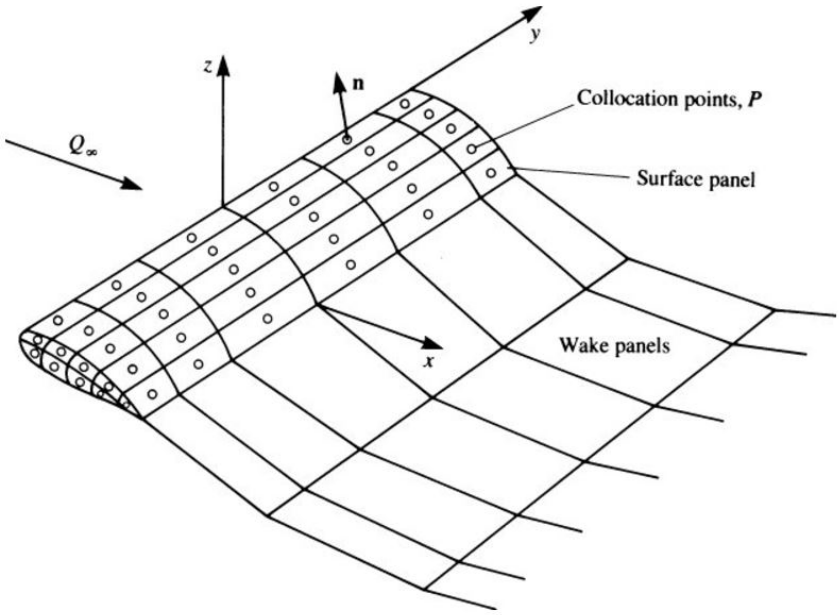

Figure 6.3: Panel distribution over the wing and wake surface [17].

The strength of the singularities distributed at the collocation points is usually calculated by assigning *influence coefficients*, C_k, which correspond to the influence that a singularity element with unit strength would have on every point of the flow field, and which are determined exclusively by the geometry of each element. Then, the influence of each panel on every other panel in the body, for every point P, is given as a function of:

$$\Sigma_{k=1}^{N} C_k \mu_k \tag{6.6}$$

being μ_k the strength of every singularity at every collocation point k. The strength of the singularities established in this way are, then, linked to the required velocities over the wing and wake through Green's identity, and then to the boundary condition for the geometry of the wing itself, by ensuring that the vertical velocity or downwash, w, for a thin wing is given by:

$$w'(x, y, 0^{\pm}) = U_\infty(\alpha + \frac{\partial \eta_c}{\partial x} \pm \frac{\partial \eta_t}{\partial x}) \tag{6.7}$$

where α, η_c, and η_t refer to the angle of attack, camber, and thickness of the wing, respectively. At this point, the problem is typically split into the *angle of attack and camber* problem, related to the doublet distribution on the wing and wake, and the *thickness* problem, linked to the source distribution on the wing.

6.2 Vortex lattice method

Vortex ring-based methods are employed to solve the angle of attack and camber problem, disregarding the thickness of the wing and applying the boundary condition:

$$w'(x, y, 0^{\pm}) = U_{\infty}(\alpha + \frac{\partial \eta_c}{\partial x}) \tag{6.8}$$

The doublet-vortex analogy is then employed to solve the simplified Green's identity through a distribution of horseshoe vortices on the wing and wake, where the wake is modeled by the *legs* of the horseshoe vortices located on the wing. The downwash is related to the strength of these vortices through:

$$w'(x_P, y_P) = \Sigma_{k=1}^{N} C_k(x_P, y_P)\Gamma_k \tag{6.9}$$

at every point $P(x_P, y_P)$. These vortices are divided in vortex segments with equal, constant circulation as established by Helmholtz's laws for vortex filaments, and the velocity induced by each of these segments can be obtained from the Biot-Savart law as:

$$\vec{\Delta} q = \frac{\Gamma}{4\pi} \frac{d\vec{l} \wedge \vec{r}}{r^3} \tag{6.10}$$

and the contributions of every segment to the velocity at a point P are then added for all the horseshoe vortices distributed throughout the wing.

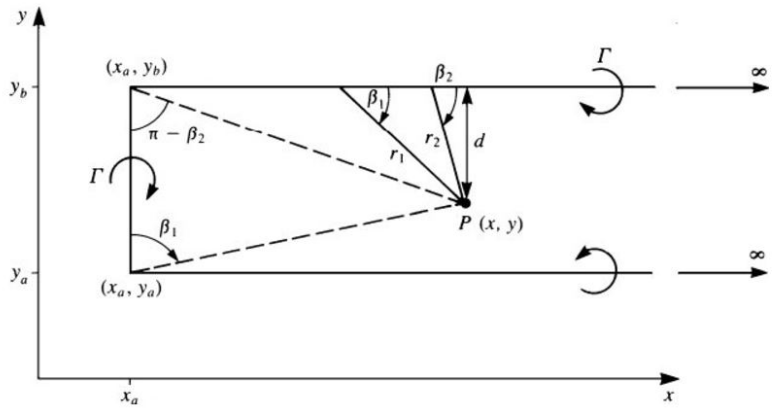

Figure 6.4: Horseshoe vortex with finite "head" and infinite "tails" [17]

For the purposes of this work, a vortex lattice method was employed to approximate the angle of attack at which the aircraft should fly in order to keep steady level flight

conditions during the cruise flight phase. The basic wing without wingtip devices was taken as a reference, and a vortex ring algorithm based on those presented by Katz [17] was developed and implemented in MatLab. The main steps of the process were the following:

1. Geometry **discretization**. The geometry of the wing was defined according to the parameters defined in Chapter 3, and a number of panels were located along the chordwise and spanwise axes. In order to guarantee that the solution was not affected by the number of panels employed, a grid independence study was performed until a relative difference $\Delta < 0.5\%$ was achieved between lift coefficient results. The final number of panels was 50x50=2500, distributed equally along the chordwise and spanwise directions. The collocation points were defined by the average of the spanwise and chordwise position of the corner points of every panel, as shown in figure 6.5.

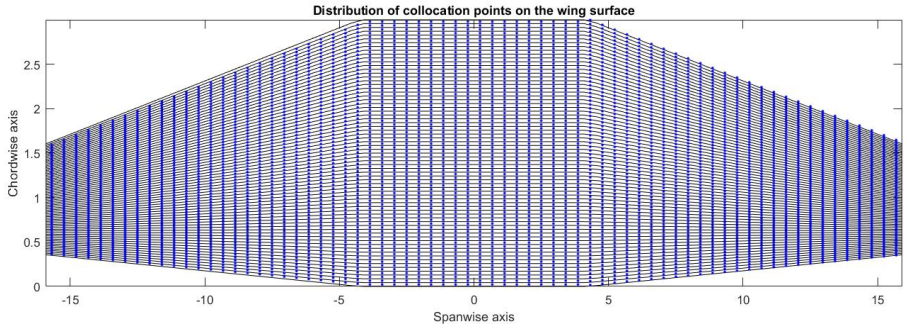

Figure 6.5: Panels and collocation points over the wing surface, not to scale

As recommended by Katz [17], the "head" segment of the horseshoe vortices was located at 1/2 the distance between the panel limit closer to the leading edge of the wing and the collocation point defining the panels.

2. Computation of the **influence coefficients** C_k. This was performed through a vortex ring algorithm, defining the two vortex ring points farther from the leading edge at a distance of 10^6m downstream; this created the illusion of the horseshoe vortices presenting infinite vortex legs. A matrix of influence coefficients was obtained, representing the effect of every vortex element on every given point over the wing.

3. Obtaining the **circulation** Γ for every horseshoe vortex element through equation 6.9. As the cruise angle of attack was not yet known, a range of angles of attack from 0^o to 15^o was analyzed in order to obtain the lift coefficient slope. Being merely an approximation, the small contribution of the airfoil's camber was neglected for simplicity in this calculation. The pressure coefficient at every point in the wing could then be obtained through the circulation and the freestream velocity, as:

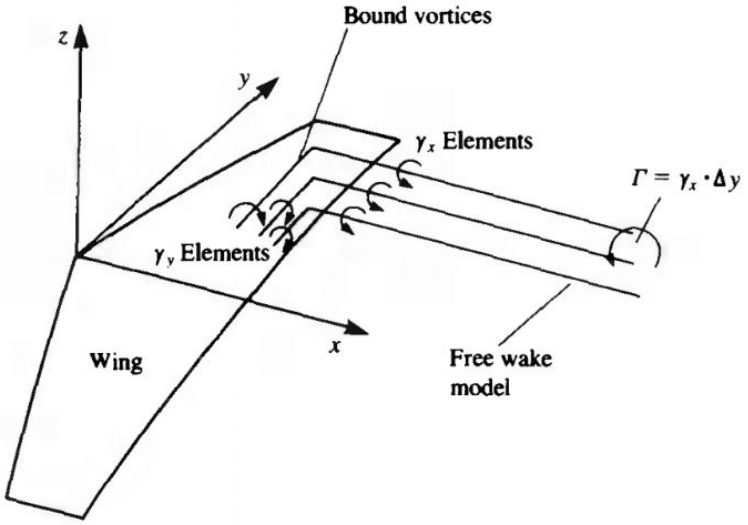

Figure 6.6: Horseshoe vortices distributed on a wing's surface [17]

$$C_p = \frac{-2\Gamma_k}{U_\infty} \tag{6.11}$$

and, finally, the lift coefficient was calculated for every angle of attack from the contributions to the pressure coefficient of every vortex element. In this way, it was possible to calculate the lift coefficient slope with respect to the angle of attack, $C_{L\alpha}$, for the following steps.

4. Finding the **cruise angle of attack** α_{cr}. Once the lift slope $C_{L\alpha}$ was known, the angle of attack could be found from the required value of the lift force to compensate for the weight of the aircraft, at cruise altitude and velocity, thus maintaining steady level flight conditions. For a reference aircraft mass of m=15,000kg, estimated from the nominal masses for the CN235 aircraft discussed in chapter 7, the lift coefficient calculated through

$$C_L = \frac{2mg}{\rho U_\infty^2 S} \tag{6.12}$$

yielded an angle of attack of $\alpha_{cr} = 4.26^o$, which was employed as the cruise angle of attack for all ANSYS Fluent cruise conditions simulations.

6.3 3D Panel method and XFLR5 analysis

Three-dimensional panel methods, unlike the vortex lattice method discussed above, do consider the thickness of the wing and its effect of the fluid flow, and thus are

more likely to provide an accurate result for a cambered airfoil, where the contribution of the source distribution to the total lift cannot be neglected based on symmetry considerations anymore. For this reason, and aiming to obtain a second, independent estimation of the effect of wingtip devices on the aerodynamic efficiency of the wing, the three-dimensional panel method embedded in XFLR5 was employed to perform a series of analyses for some of the geometries described in chapter 3.

XFLR5 is an open source, free software oriented to the analysis and design of model sailplanes. Although its use for any other aeronautical applications is strongly discouraged, it can be employed for some preliminary, merely informative estimations such as those required for this work. It allows for the definition of virtually any airfoil geometry, and, although its wing and body design can be quite limited for some applications, it provides the user with sweep, taper, and dihedral options for the wing and tail. Its three-dimensional panel method is based on source and doublet distributions over the wing surface; its wake model, however, consists of flat plates extending beyond the trailing edge and far downstream, providing a flat wake that is often far from accurate. The strength of the doublets distributed throughout the wake is calculated as the difference between those of the upper and lower panels of the wing surface at the trailing edge. These limitations, particularly those concerning the wake shape, would most certainly prevent the result from being close to those found through computational fluid dynamics or experimentally; however, it was expected that the comparison between the different wing+winglet combinations would provide a qualitative estimation of the main parameters affecting the aerodynamic efficiency when wingtip devices are concerned.

The first step in the XFLR5 analysis was to import the airfoil that would provide the cross-section of the wing, the NACA 65_3-218. As recommended by the XFLR5 guidelines [48], a global refinement was performed, increasing the number of points defining the airfoil to 300. Afterwards, a batch analysis was conducted, yielding the airfoil polars for lift and drag coefficients at a range of angle of attack of $\alpha \in [-5^o, 12^o]$ and Reynolds number $Re \in [500,000; 30,000,000]$, at both takeoff and cruise conditions. Although a wider range of angles of attack would be useful for the analysis, convergence problems prevented the computations beyond those values. These polars would be the basis for the complete wing analysis, and, as XFLR5 is not quite prepared to compute parasite drag in three-dimensional flows, they would provide an estimation of two-dimensional viscous drag that would later be extrapolated to the 3D case.

Once the data for the given airfoil was acquired, the selected wing geometries were model on XFLR5's "Wing and Plane design" mode. As the options for non-conventional designs are quite limited, it was not possible to model wingtip devices with any sort of curvature. This excluded most of the designs presented in chapter 3, restricting the analysis to the straight winglets and raked wingtip. A total of fourteen wings were analyzed, including the basic wing without wingtip devices, the raked wingtip, and the short and long winglets (with a semispan of 1m and 2m respectively) at Cant angles of 00^o, 15^o, 30^o, 45^o, 60^o, and 75^o. The geometries were chosen to mimic as closely as

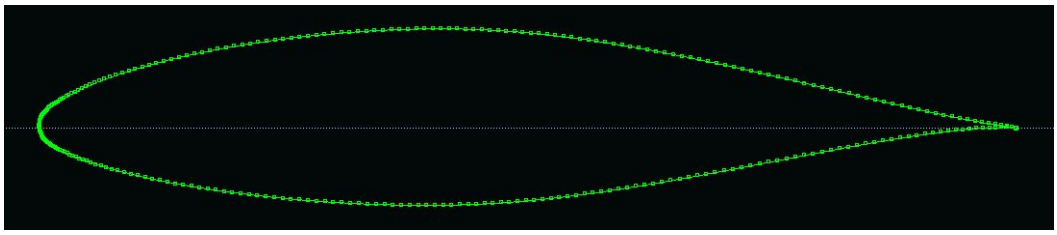

Figure 6.7: NACA 65_3-218 airfoil imported in XFLR5

possible those created in CATIA, in order to observe and compare any possible trends with those found through CFD analysis.

Along with the geometry, the number and distribution of panels employed in every wing section had to be selected. It was found that, while a higher number of panels provided results closer to being grid-independent, it also led to difficulties computing the solution, sometimes limiting the values computed to a very narrow range. A compromise had to be reached with the maximum possible number of panels which allowed the software to compute the solution at least for the range $\alpha \in [-2^o, 11^o]$. For most cases, this number could be estimated as approximately 600 panels in the rectangular section, 600 panels in the trapezoidal section, and 200 panels for the winglet surface, amounting to a total number of panels in the range [2200, 2800] for the whole wing. The panel distribution was chosen to minimize the panel size at key areas throughout the wing, such as the leading edge, the wing and winglet tips, and the wing-winglet union. For this purpose, cosine and -sine distributions were selected along the chordwise and spanwise directions, respectively. The resulting wing geometry, as well as the panel distribution over its surface, can be observed in figure 6.8.

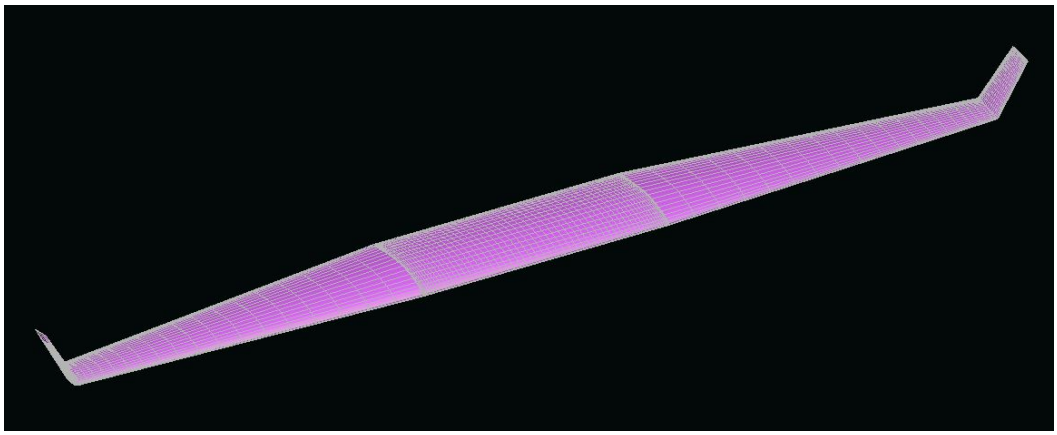

Figure 6.8: Wing+long winglet combination, at a Cant angle of 60^o, as shown in the XFLR5 geometry editor

All the wings defined in this manner were, as it was stated before, analyzed for the

same conditions considered in the ANSYS Fluent simulations, namely:

- Cruise conditions, at an altitude h=4,575m and velocity $U_\infty = 125m/s$, ISA+0.
- Takeoff conditions, at sea level and velocity $U_\infty = 50m/s$, ISA+0.

However, in order to gain a better understanding of the effects of velocity and altitude in the aerodynamic efficiency for different wingtip devices, two more cases were added to each flight condition and geometry, at $U_\infty = 100m/s$ and $U_\infty = 80m/s$, respectively. Overall, a total of 84 analyses were performed, each corresponding to a different geometry-speed-altitude combination, and for a range of angles of attack $\alpha = [-5^o, 12^o]$.

It has been mentioned before that the validity of the results obtained in XFLR5 was questionable, particularly those concerning viscous forces and the parasitic component of drag. Since parasitic drag cannot be computed through potential flow theory, values of C_{d0} cannot be trusted to correspond to reality. A similar problem appears with the induced drag. The computation of this component in XFLR5 is performed through the Trefftz plane method, which is based on the concept that, sufficiently far downstream, the variations in circulation of the doublet distribution in the wing along the chordwise coordinate can be neglected. At this point, it is possible to define a plane perpendicular to the fluid flow, delimiting a control volume upon which conservation laws can be applied in a simplified manner. XFLR5 ensures this independence from the chordwise direction by locating the Trefftz plane at a distance of 100MAC downstream from the trailing edge. However, it is not possible to compute wake relaxation in this software -an iterative process through which the shape of the wake matches that determined by the streamlines trailing behind the wing-: the wake is modeled as a collection of flat panels extending far behind the wing up to the selected plane. This also eliminates the effect of wake roll-up behind the wingtips, even if downwash values clearly indicate flow recirculation. These inconveniences lead to the conclusion that the results obtained through these analysis are merely illustrative, and will likely be much more reliable in terms of the additional lift generated by the wingtip devices than the reduction in drag force they may provide.

6.4 Compressibility corrections

The equations gathered in this chapter have been, until now, expressed for potential, incompressible flow. This is the flow regime that has been considered for the vortex lattice method (VLM) analysis, since the higher Mach number found in the cases considered is $M = 0.388$ in cruise conditions. It is generally accepted that fluid flows at $M < 0.3$ can be safely assumed to be incompressible, with $M_\infty \to 0$. Being the cruise Mach number, as it is, in the limit for this consideration, the Prandtl-Glauert compressibility correction was applied to the vortex lattice method described above in order to examine whether the cruise angle of attack was largely affected by its incorporation.

The Prandtl-Glauert compressibility correction is derived from the equation for potential, compressible flow,

$$(1 - M_\infty^2)\frac{\partial^2 \phi}{\partial x^2} + \frac{\partial^2 \phi}{\partial y^2} + \frac{\partial^2 \phi}{\partial z^2} = 0 \tag{6.13}$$

whose boundary conditions are the same as those employed in the incompressible problem, and it is based on a variable transformation such that:

- $\tilde{x} = x$
- $\tilde{y} = y\sqrt{1 - M_\infty^2}$
- $\tilde{z} = z\sqrt{1 - M_\infty^2}$

which lead, in the end, to the conclusion that an equivalent wing with a reduced span, $\tilde{b} = b\sqrt{1 - M_\infty^2}$, can be analyzed in incompressible regime to yield the same results as the actual wing would in compressible flow. This introduces a factor $\sqrt{1 - M_\infty^2}$ in the expressions for the aerodynamic load coefficients, such that:

$$C_{L,i} = \frac{C_{L,c}}{\sqrt{1 - M_\infty^2}} \tag{6.14}$$

As the computation of the cruise angle of attack was based on the geometry of the wing and its lift coefficient, it was considered that compressibility corrections could have an effect on the resulting value of α. However, among the series of estimations already related to the computation of this parameter, the changes introduced by the compressibility correction at such a low Mach number were not as significant as to be taken into account for future analysis.

Chapter 7

Mission Design

7.1 Performance parameters

While the data obtained from the computational fluid dynamics simulations and XFLR5 analysis would show the general trends for the changes concerning the performance of the wing when different wingtip devices were added, it would do so in terms of aerodynamic loads -lift and drag- exclusively. To obtain a better insight on how the changes in these two magnitudes would affect flight performance, a number of parameters were employed:

- **Lift-to drag ratio** or aerodynamic efficiency, L/D. As mentioned in previous sections, it was the main parameter considered to estimate general, clear changes in performance, as it affects the range and endurance. Since the main advantage of wingtip devices is the alleged drag reduction, and given that some of them act as span extensions, providing additional lift, the aerodynamic efficiency was expected to increase with respect to the basic configuration for most of the designs considered.

  The effect of Cant angle Θ on this parameter was unclear, although studies [10, 20, 22] seem to suggest that the L/D ratio increases slightly with the Cant angle, to reach a maximum and decrease at a variable value of this parameter. A doubtful case was that of the blended winglets [32], which were supposed to reduce the interference drag at the wing-winglet union; it was not clear whether the quality of the mesh would suffice to observe this phenomenon, or whether the effects of this type of drag were significant in the flow regimes considered. Values of L/D ratio, as observed in Kundu [18] could be typically expected to be in the range of [9, 17] depending on the characteristics of the aircraft.

- **Lift and drag coefficients**: the non-dimensional approach to the aerodynamic loads, they were employed to observe the effects of winglets in the lift and drag forces independently of the speed and altitude determined by the flight phase. According to the usual model as presented in Anderson [2], the lift coefficient should only be a function of the angle of attack, with an additional term included in cambered airfoils to account for the lift generated at $\alpha = 0^{o}$, as:

$$C_L = C_{L_\alpha} + C_{L_0} \tag{7.1}$$

while the drag coefficient would be usually modeled through a parabolic drag polar, such that:

$$C_D = C_{D_0} + kC_L^2 \tag{7.2}$$

It was expected that the results obtained through the Fluent simulations would allow for the computation of k and C_{D_0}, which would most likely change for every geometry: while C_{D_0} is influenced by the wetted area of the wing, k is directly related to its aspect ratio. Although the drag polar can be modified to consider the effect of the cambered airfoil, adding a term $C_{L_{md}}$ corresponding to the lift coefficient at the point of minimum drag such that

$$C_D = C_{D_0} + k(C_L - C_{L_{md}})^2 \tag{7.3}$$

this contribution is often sufficiently small to be neglected altogether, particularly for airfoils with a small camber such as the one employed in this work.

- **Range**: range is defined as the maximum distance that the aircraft can travel for a given fuel mass. It is typically computed through the Breguet range equation, which establishes that the range depends not only on the fuel consumed, but also on the flight speed V, specific fuel consumption C, and aerodynamic efficiency L/D, as:

$$R = \int_{W_1}^{W_2} -\frac{V}{C}\frac{L}{D}\frac{dW}{W} \tag{7.4}$$

The term $-\frac{V}{C}\frac{L}{D}$ is commonly referred to as the *range parameter*, and it is employed as a measure of the performance of the aircraft at a given flight condition. In this case, it was expected to be affected directly by the presence of wingtip devices, since they would most certainly modify the lift-to-drag ratio. The specific fuel consumption, $dW/dt = -CT$, is typically related to the flight velocity through

$$C = k_C V^n \tag{7.5}$$

where k_C is a constant and the exponent n depends on the type of engine, being usually closer to 0 for turbofans and 1 for turboprops; the latter usually employ a specific fuel consumption per unit of power delivered, C_{power}, independent of the speed, such that:

$$\frac{dW}{dt} = -C_{power}P_D \tag{7.6}$$

and the value of C can be obtained from the relationship between trust and power delivered, yielding $C = C_{power}V/\eta_p$ for a propeller efficiency η_p. For the purposes of this work, the specific fuel consumption C was estimated from the typical values provided by Howe [14] for a generic turbuprop at 15,000ft and Mach $M = 0.388$, yielding a value of $C = 0.38$ 1/h for cruise conditions.

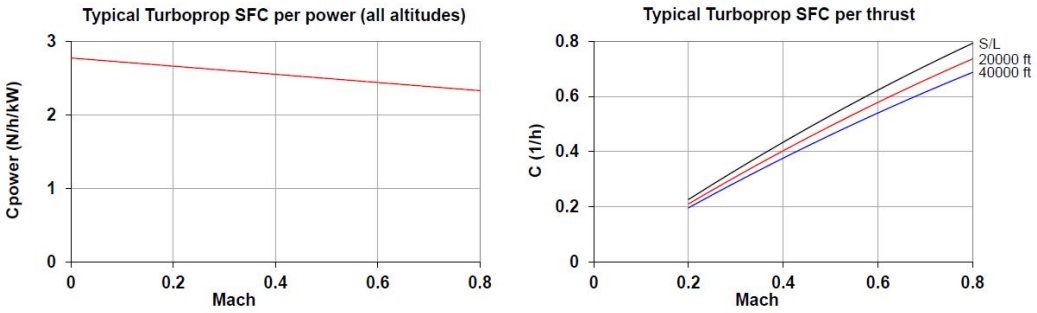

Figure 7.1: C_{power} and C trends for generic turboprops [14]

In the range calculation performed for the mission designs and described in the next section, the range parameter P_R was kept constant for simplicity. In a real-world application, this would result on a cruise-climb flight path: with constant lift coefficient and speed, the aircraft would need to increase its altitude to compensate for the decrease in weight while maintaining steady level flight conditions. Although cruise-climb profiles are typically not allowed, since pre-determined flight levels are fixed for every flight path, it has been considered here for estimation purposes.

- **Endurance**: similarly to range, endurance is defined as the maximum time the aircraft can stay in flight for a given velocity, C, fuel mass, and aerodynamic efficiency; it is computed as:

$$E = \int_{W_1}^{W_2} -\frac{1}{C}\frac{L}{D}\frac{dW}{W} \tag{7.7}$$

As in the case of range, endurance is directly affected by changes in the aerodynamic efficiency caused by the presence of wingtip devices. The particular effect of these changes in two given example missions will be described in the following section.

7.2 Configuration of typical missions

The usual mission profile for a general aircraft consists of a number of segments -takeoff, climb, cruise, descent, loiter, and landing- representing the different phases in the flight path of the aircraft from one point to another. Virtually any mission configurations can be designed, by extending the simple cruise mission through additional diversion

cruise or loiter phases, including two cruise phases at different altitudes, or through any other required modifications to the standard profile. An example of such an extended mission, including an additional cruise and loiter, is shown below in figure 7.2.

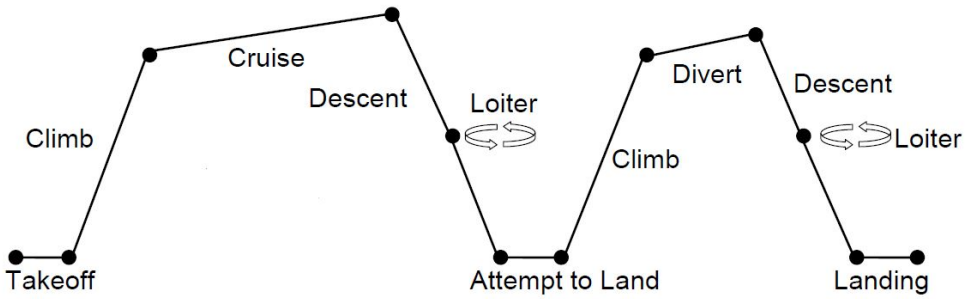

Figure 7.2: Example of an extended mission profile [12]

In order to calculate a certain design variable or performance parameter, such as the range or the required fuel mass at takeoff, the mission segments are defined by their start and end points and treated independently; all required calculations are based on the mass fraction for each segment, which is defined as the ratio of aircraft mass at the start and end of the segment, and it provides the amount of fuel burnt. In this way, for a segment A starting at a point n in the flight path, and ending at $n+1$, the mass fraction is

$$k_A = \frac{m_{n+1}}{m_n} \tag{7.8}$$

The mass fractions for some segments present approximately the same value for most aircraft and mission configurations, and thus these standard values are often employed for a quick design. This is the case of the takeoff, climb, and landing mass fractions, which are gathered here as shown by Raymer [21]:

- $K_{TO} = 0.99$
- $K_{CL} = 0.985$
- $K_{LD} = 0.995$

The mass fraction for the loiter and holding segments are usually calculating by linking the fuel consumed to the endurance equation, as:

$$K_{LR} = e^{\frac{E \cdot C_{power} V}{\eta_p L/D}} \tag{7.9}$$

for a propeller aircraft, assuming that the aerodynamic efficiency and velocity remain constant during the segment. In a similar way, the cruise mass fraction can be expressed through the Breguet equation for range, for constant V and L/D:

$$K_{CR} = e^{\frac{R^* \cdot C_{power}}{\eta_p L/D}} \tag{7.10}$$

where R^* refers to the reduced range, understanding that a part of the total range was already covered during the climb phase, such that:

$$R_{total} = R^* + \frac{H_c}{tan\gamma_c} \tag{7.11}$$

where H_c refers to the cruise altitude reached during the climb, and γ_c to the average climb angle. The total mass fraction, indicating the overall amount of fuel burnt during the whole mission, can then be calculated as the product of the mass fractions for every mission segment. For a simple mission with a single cruise and loiter, then:

$$K_{total} = K_{TO}K_{CL}K_{CR}K_{LR}K_{LD} \tag{7.12}$$

Given that the performance of the aircraft, and particularly its range and endurance, are clearly linked to its mass, and especially to the percentage of total mass represented by the fuel, it is common to measure the capabilities of the aircraft by studying the effect that varying the payload and fuel mass produces on range. This is the idea behind the payload-range diagram, which establishes three performance points between which the payload/range relationship is defined as linear. For this purpose, key aircraft masses are defined:

- **Maximum Takeoff Mass** (MTOM): it is the maximum total mass permissible for flight; it is usually determined by structural constraints.
- **Operating Empty Mass** (OEM): it is the mass of the aircraft with all the equipment required to fly onboard, excluding payload and fuel.
- **Payload Mass** (PLM): it is the mass of everything not essential to the flight, such as passengers or cargo.
- **Maximum Zero Fuel Mass** (MZFM): it is usually computed as the sum of the operating empty mass and the maximum allowable payload, and it may be limited by structural and spatial constraints.
- **Maximum Fuel Mass** (MF): the maximum amount of fuel that can be carried onboard, restricted to the volume of the fuel tanks and pods.

The takeoff mass m_0, then, must be found as the operating empty mass plus a combination of fuel and payload mass, and it cannot exceed the given maximum takeoff mass of the aircraft. The key points on the payload-range diagram R_1, R_2, and R_3, correspond to the values of range achieved for a given mission with three standard payload/fuel combinations:

- R_1 corresponds to the range with maximum takeoff mass and maximum payload, where the fuel mass is calculated as $m_f = MTOM - MZFM$.
- R_2 is the range with maximum takeoff mass and maximum fuel, with the payload mass calculated as $MPL = MTOM - MF$.

- R_3, also termed the *ferry range*, is achieved with maximum fuel and null payload, so that the takeoff mass is given by $m_0 = OEM + MF$.

An example payload-range diagram showing the typical proportion between the segments defined by R_1, R_2, and R_3, is shown in figure 7.3. The location of the key points, as well as the slope of the curves interpolated between them, is subject to change as a result of design modifications. As it was already observed in chapter 3, an increase in aerodynamic efficiency -such as that expected from the addition of wingtip devices- results on an increase in range for all three points, although the additional mass of these devices would likely raise the OEM and decrease the maximum allowable payload. A similar effect was expected to appear when studying the payload-range diagram for the proposed mission.

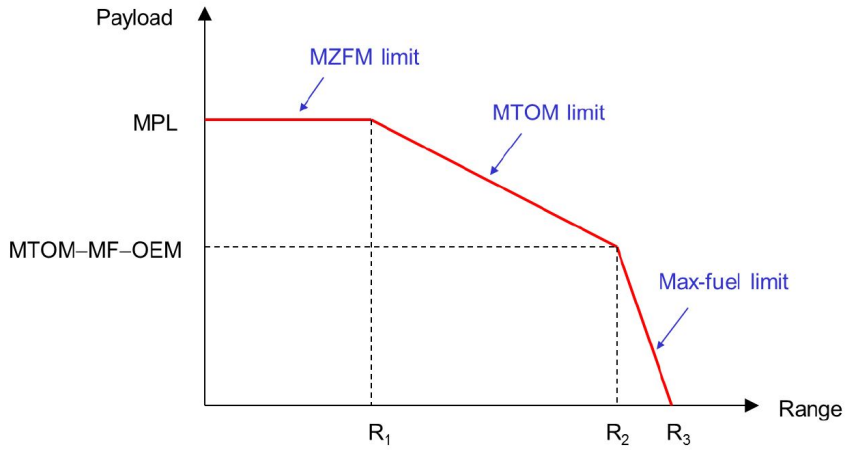

Figure 7.3: Example of a payload-range diagram [12]

7.3 Range Assessment Mission

The first mission designed for the theoretical aircraft employing the wing geometries presented in chapter 4, and loosely based on the CN235 aircraft, aimed to study the alleged increase in range that could arise from incorporating wingtip devices in the wing design. In order to provide a simple overview of this improvement, two wing+wingtip device geometries were chosen to be compared to the reference wing. Since it was not possible to find a convincing estimate of the wingtip device mass, the effect of its addition on the aircraft masses was not observed; however, since it would most likely amount to a very small percentage of the total OEM, the reduction in maximum payload mass is assumed to be quite small. All data employed for this section was derived from the ANSYS Fluent simulations presented in chapter 5.

The mission chosen as an example was a simple cruise mission with the following characteristics:

- Takeoff phase with a mass fraction $K_{TO} = 0.99$.
- Initial climb to cruise altitude, $H_c = 4,575m$, at an average climb angle $\gamma_c = 3^o$ and mass fraction $K_{CL} = 0.985$..
- Cruise phase at an altitude $H_c = 4,575m$, speed of $V = 125m/s$, and ISA+0 conditions, with an unknown range to be determined by the fuel fraction corresponding to this segment and a specific fuel consumption $C = 0.38$ 1/h estimated from the charts shown in figure 7.1.
- Loiter for 30 minutes at 2,000m, with an estimated specific fuel consumption $C = 0.5$ 1/h as observed in typical trends for turboprops.
- Approach and landing phase with a mass fraction K_{LD}=0.995.

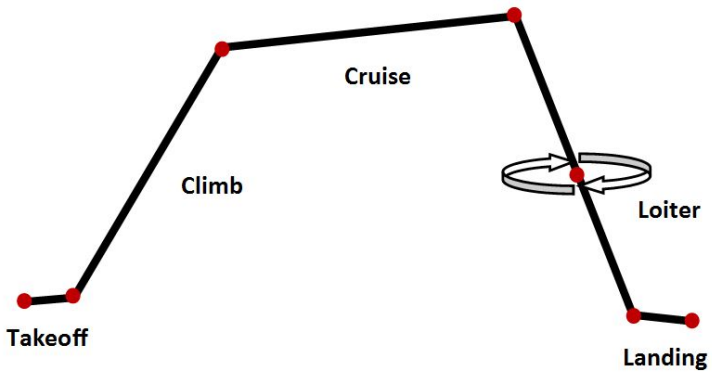

Figure 7.4: Mission profile for the range assessment

As the mass fractions for takeoff, climb, and landing, were estimated from those found in Raymer [21] and Kundu [18], the only unknowns were the mass fractions for the loiter and cruise segments. The loiter mass fraction, K_{LR}, was found from the endurance equation 7.9 as shown in section 2. As the ANSYS Fluent simulations did not provide aerodynamic efficiency results for loiter conditions, the loiter L/D was based on the usual percentages for a generic aircraft: the L/D ratio at cruise was considered to be 99% of the maximum, and the loiter aerodynamic efficiency was computed as:

$$(\frac{L}{D})_{LR} = 0.87(\frac{L}{D})_{max} = 0.88(\frac{L}{D})_{CR} \tag{7.13}$$

Once the mass fractions corresponding to all mission segments except cruise were known, the total mass fraction, defined as the ratio of final to initial aircraft mass, was calculated as:

$$K_{total} = \frac{1}{1 + c_t}(c_t + \frac{m_{final}}{m_{TO}}) \tag{7.14}$$

where c_t refers to the contingency fuel percentage, indicating the fuel mass typically added to account for unforeseen circumstances, unexpected weather conditions, air traffic issues or headwinds. In this case, a typical value of $c_t = 6\%$ was employed, together with mass values similar to those found in Jane's [16] for the CN235 aircraft:

- Maximum Takeoff Mass, MTOM=16,500 kg
- Maximum Zero-Fuel Mass, MZFM=15,000 kg
- Operational Empty Mass, OEM=9,450 kg
- Maximum Fuel Mass, MF=4,230 kg

From these values, the total mass fraction K_{total} was calculated for every key point in the diagram. The cruise mass fraction, K_{CR}, could then be calculated from equations 7.12 and 7.14, such that:

$$K_{CR} = \frac{K_{total}}{K_{TO}K_{CL}K_{LR}K_{LD}} \tag{7.15}$$

and the range corresponding to the cruise phase was found through the Breguet equation as shown in 7.10. Adding the range credited to climb provided the total range value for every point in the payload-range diagram.

7.4 Endurance Assessment Mission

A similar calculation to the range assessment detailed above was performed for the endurance, aiming to study the alleged increase in flight time that could be achieved with the improved aerodynamic performance provided by the addition of wingtip devices. To this extent, a double cruise mission was designed for an aircraft similar to a CN235 on a maritime patrol mission. A cruising range of 200km, roughly the distance from a takeoff location in the Seville province to the Straits of Gibraltar, was established for the mission profile shown in figure 7.5.

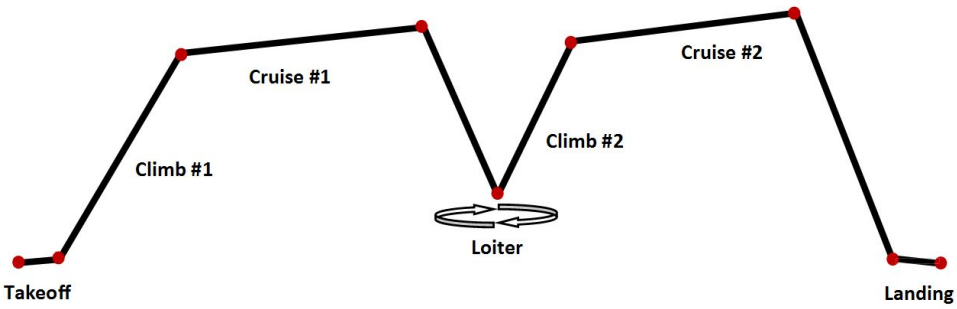

Figure 7.5: Mission profile for the endurance assessment

In this case, the mass fraction for the cruise phases was calculated from the Breguet range equation for the known range, accounting for the range credited to both climb phases with an average climb angle $\gamma = 5^o$. The total mass fraction was calculated from equation 7.14, and the mass fraction for the loiter phase was found as:

$$K_{LR} = \frac{K_{total}}{K_{TO}K_{CL1}K_{CR1}K_{CL2}K_{CR2}K_{LD}} \tag{7.16}$$

from which the endurance could be obtained through the endurance equation as in 7.9, performing the same approximation for the loiter aerodynamic efficiency as in the previous section. The mass values employed corresponded to maximum takeoff mass with maximum fuel, in an attempt to maximize the endurance without neglecting the required payload.

7.5 Takeoff Field Length and Landing Distance

The range and endurance assessments were based on the aerodynamic efficiency values found in Fluent for cruise conditions. In a similar way, the lift and drag values found for takeoff conditions were employed to estimate the effect of winglets on the maximum lift coefficient, stall velocity, takeoff field length, and landing distance. Since

$$L = \frac{1}{2}\rho U_\infty^2 S C_L \tag{7.17}$$

and given that the maximum lift coefficient should be logically found at the stall velocity, such that

$$L = \frac{1}{2}\rho V_{stall}^2 S C_{L_{max}} \tag{7.18}$$

Considering that the initial stall speed defined for the CN235 aircraft is $V_{stall} = 43.3 m/s$ and that the wing velocity at takeoff conditions was set to $V_{TO} = 50 m/s$, and assuming the load factor at takeoff conditions to be the same for a slightly lower speed, it can be concluded from the above equations that

$$C_{L_{max}} = (\frac{50}{43.3})^2 C_L = 1.33 C_L \tag{7.19}$$

from which it can be easily deduced that the maximum lift coefficient is directly proportional to the lift coefficient at takeoff. Since the incorporation of wingtip devices would allegedly increase the lift coefficient for a given angle of attack, it is logical to think that in that case the square of the stall velocity would decrease proportionally, thus broadening, even if slightly, the flight envelope.

The main purpose of computing the maximum lift coefficient is to study its effect on the takeoff field length and landing distance. The takeoff field length, or TOFL, is usually defined as proportional to the so-called takeoff parameter, TOP, so that $TOFL = k_{TOP} \cdot TOP$, where

$$TOP = \frac{m/S}{\sigma C_{L_{max}} T/W} \tag{7.20}$$

where m/S is the wing loading, σ refers to the density ratio in the International Standard Atmosphere model (at sea level and standard conditions, $\sigma = 1$), and T/W is the thrust-to weight ratio provided by the engines. It can easily be observed that an increase on the lift coefficient caused by the addition of wingtip devices will cause the takeoff field length to decrease proportionally. A similar effect can be observed in the landing distance, given by:

$$S_{LD} = \frac{5}{3}[\frac{5m/S}{\sigma \cdot C_{L_{max}}} + S_a] \tag{7.21}$$

where S_a represents the *approach* distance and the fractional term represents the *ground roll* distance, multiplied by a standard safety factor of 5/3. In this case, only the ground roll distance would be affected by an increase in the lift coefficient, and so the effect on the total landing distance would not be as noticeable.

Chapter 8

Experimental Measurements

8.1 Aim and objectives

After several wing geometries were analyzed through computational fluid dynamics in Ansys FLUENT and a three-dimensional panel method in XFLR5, as described in previous chapters, it was decided that a set of experimental measurements could be useful to complete the insight on the impact of wingtip devices in the lift and drag forces acting on the wing. For this purpose, several geometries among those presented in chapter 4 were modeled at a scale of 1:100 and 3D printed in ABS plastic, namely: the reference basic wing, the wing+long winglet at $\Theta = 30^o$, $\Theta = 45^o$, and $\Theta = 60^o$; the wing+double winglet at $\Theta = 60^o$; the wing+blended winglet at $\Theta = 45^o$, and the wing+raked wingtip. In order to reduce the roughness of the surface and eliminate defective areas, they were thoroughly filed and polished with acetone.

The aim of the experimental measurements was to study the behavior of different wing+wingtip devices configurations at lower Reynolds numbers than those employed in the CFD and panel analyses. For this purpose, the recirculating water channel from the Department of Thermal and Fluids Engineering at Universidad Carlos III de Madrid was employed to create the external flow field for the model wings. With an approximate capacity of $2.5m^3$ and a test section measuring 0.7m in length and 0.25x0.25m in area, and equipped with grids and honeycombs to minimize fluctuations within the flow, it provided a flow domain similar to that considered in the CFD simulations, with a constant freestream velocity U_∞ regulated through two pumps with adjustable frequencies.

Since the effect of wingtip devices was studied through the changes they provoked on the lift and drag forces, it was necessary to find the means to measure the forces exerted on the model wings by the water stream in the channel. The Department of Bioengineering and Aerospace Engineering at Universidad Carlos III de Madrid provided a Kyowa LAT-10KA-1 six-degree load cell, able to measure forces and moments about three-dimensional Cartesian axes, coupled with an amplifier with a gain $k = 2,000V$, and a National Instruments NI-cfp1804 Compact FieldPoint module. The model wings would be fixed to the load cell and submerged in the fluid; the transducer signal, too

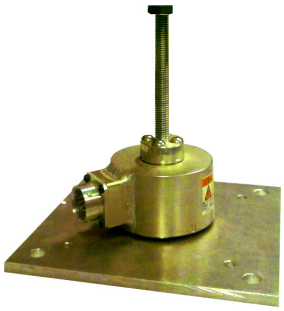

Figure 8.1: Six-degree transducer employed to measure forces and moments

low to be read with a conventional voltmeter, would be amplified and sent to the Field-Point module, which would, in turn, provide the final voltage data to be analyzed and processed through the National Instruments LabView software. As described in the following sections, several changes were applied to this strategy due to unexpected inconveniences.

8.2 Experimental setup

In order to avoid oscillations and measurement inaccuracies, it was necessary to fix the model wings to the load cell firmly and safely, while preventing any alterations of the flow around the wings. This was achieved by designing and 3D printing two supporting pieces, shown in figures 8.2 and 8.3: a flat plate that would be screwed to the transducer, and a versatile piece with an airfoil-shape enclosure that would act as a container for the wing. Both pieces were be fastened together, and adjustable screws helped to keep the model wings in place.

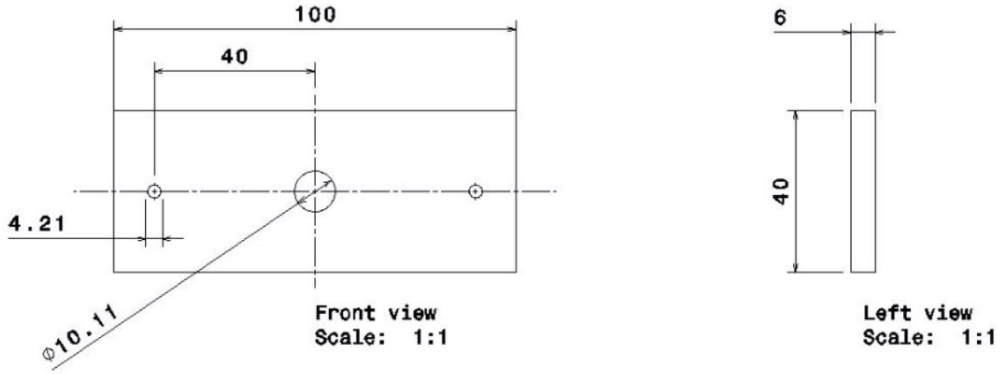

Figure 8.2: Flat plate support

Once the wings were securely fixed to the transducer, they were placed on a sup-

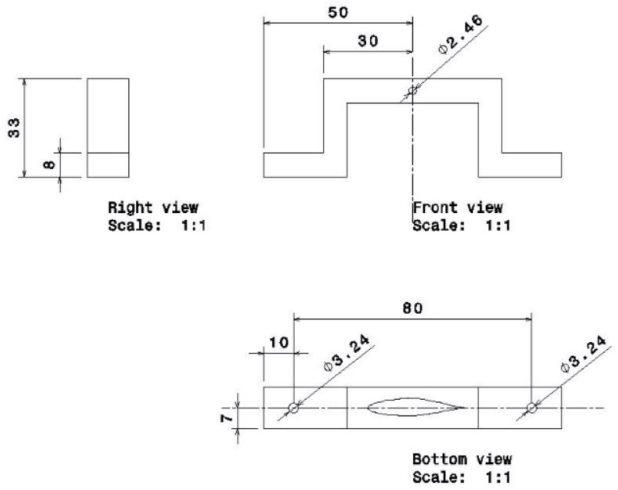

Figure 8.3: Wing support

porting structure over the water channel, ensuring that the whole wing was submerged. The transducer was then connected to the amplifier, which was powered by a desktop computer through a miniUSB-USB cable. The six amplifier outputs were, in turn, connected to the FieldPoint module, which gathered the data and transferred it to a desktop computer via a local Ethernet connection. The LabView 2017 Measurement and Automation Explorer (MAX) software was employed to check that data was being gathered and transferred correctly. A 15V computer power source was used to provide energy to the FieldPoint module.

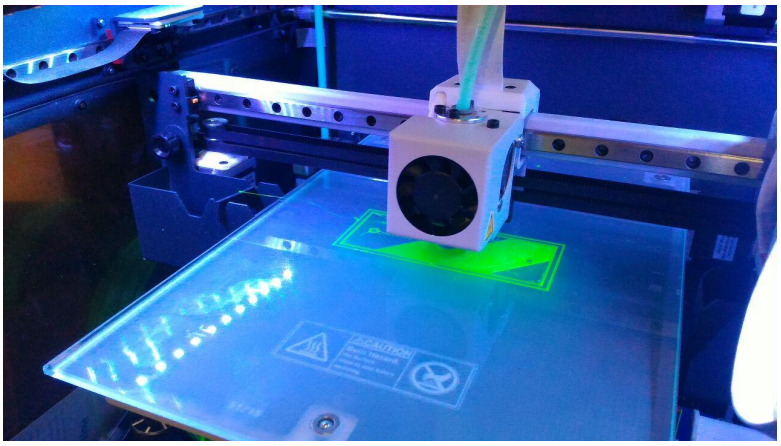

Figure 8.4: 3D printer at the initial stage of printing the wing supports

8.3 Experimental procedure

Given that the installation described until this point functioned properly, the following steps would include the processing and storage of data through the LabView 2017 software, which offered a freely distributed academic version, and the manipulation of the voltage data obtained from the transducer and amplifier to obtain the values of the forces and moments exerted on the model wings by the fluid flow. This last task required the use of the calibration matrix of the load cell, provided by the manufacturer as:

$$X = \begin{bmatrix} 2274.29 & 22.34 & 8.58 & -8.25 & -722.96 & 7.15 \\ 4.13 & 3078.84 & 9.27 & -1261.32 & -4.11 & 7.08 \\ -1.19 & -2.22 & 3395.34 & -0.54 & 3.34 & -3.77 \\ 0.14 & 347.56 & -8.44 & 1385.92 & 6.35 & 0.4 \\ -238.84 & -6.62 & 3.50 & -3.33 & 1566.56 & -1.48 \\ -3.64 & -6.67 & 5.33 & -3.43 & -3.79 & 891.37 \end{bmatrix} \tag{8.1}$$

and which, for a set of voltage data $A = (V_{fx}, V_{fy}, V_{fz}, V_{mx}, V_{my}, V_{mz})$, would provide the force vector $B = (F_x, F_y, F_z, M_x, M_y, M_z)$ such that:

$$\vec{A} \cdot \bar{X} = \vec{B} \tag{8.2}$$

as long as a 2,000V factor was included in the matrix to account for the gain of the amplifier, as described in more detail in [15]. The value of the forces for each wing at rest would then have to be subtracted from every set of forces, finally yielding the net forces and moments acting on the wing models. The remaining step would be to identify the axis corresponding to the lift and drag forces, obtaining the corresponding aerodynamic efficiency to be compared among wing+winglet configurations as in the previous analyses.

Several measurements were taken for each wing at rest. Although the amplifier was supposed to provide a stationary signal of 2.5V in every axis for an unloaded transducer [15], it was likely that the cumulative errors of the Wheatstone bridges in the load cell, voltage drops in the connected cables, and connection problems within the amplifier would modify this value substantially. In a similar effort to eliminate error due to noise or localized interferences, five measurements of forty seconds each were performed for every wing configuration, for a fixed frequency of 30Hz in each of the water channel pumps. Data amounted to a total of 50,000 points -comprising three forces and three moments each- for every wing configuration considered. The voltage signals fed to the calibration matrix were obtained as the mean of these data points for every force or moment, which allegedly provided a reliable, solid voltage value to be processed.

8.4 Problems encountered during the measurements

The empirical analysis of the effect of wingtip devices on the forces acting on the wing faced several major problems, most of which were related to defective, obsolete, or insuf-

ficiently precise instrumentation and software. Although some of them were overcome during the project by proposing alternative solutions, others were eventually proved to pose an unsolvable obstacle to the correct development of the experimental research. The most remarkable of these challenges are briefly stated below:

- Lack of a **supporting structure** for the wing and load cell over the water channel: In order to keep the load cell fixed and avoid vibrations and displacements, a temporary structure was built from aluminum profiles to provide stability and regulate the position of the load cell + wing assembly.

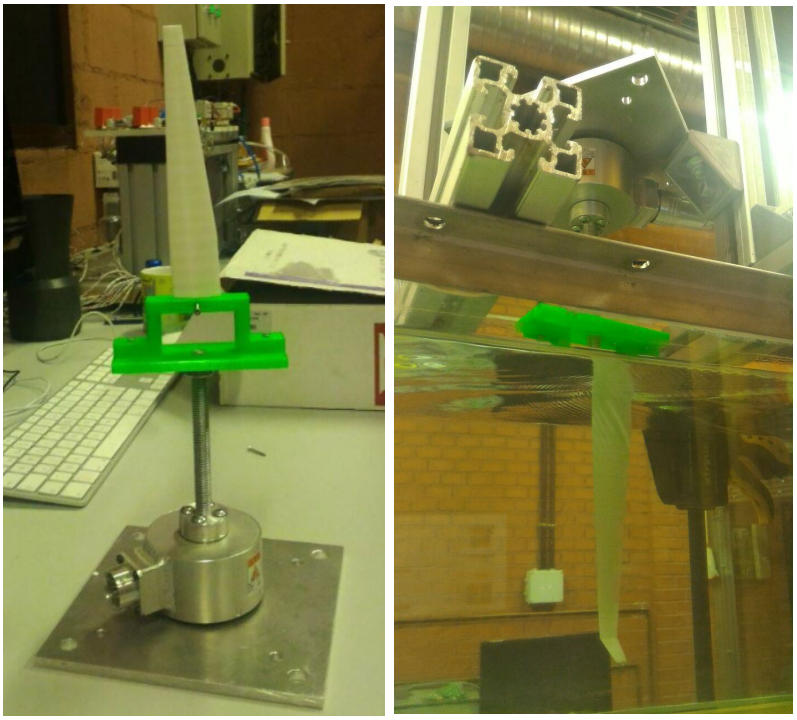

Figure 8.5: Load cell+wing assembly: a. on ground b. partially submerged

- Lack of **information concerning the load cell**, including the orientation of each of the axes for the forces and moments. They were eventually located by measuring the effect of exerting specific forces and moments along each direction, following 45º lines delimited by the position of the transducer with respect to its base. The only information available for the transducer was a page from the manufacturer found in [15], containing the maximum allowable forces and moments and the calibration matrix. Since this particular load cell is no longer in production, it was not possible to find support from the manufacturer itself.

- An **obsolete FieldPoint device**. Although the National Instruments module provided with the load cell to gather data from the transducer was able to transmit voltage values to the LabView 2017 Measurement and Automation Explorer

(MAX), it was not possible to read, process, or store this data in any way through LabView 2017. Once all errors related to the local Ethernet connection were fixed, and the proper FieldPoint driver was installed, an error message appeared stating that the FieldPoint module was no longer compatible with the current LabView versions available in the market. Considering the elevated cost of FieldPoint modules, which typically escalates beyond 1,000€ [45], the four-channel digital oscilloscope shown in figure 8.6 was chosen as an alternative.

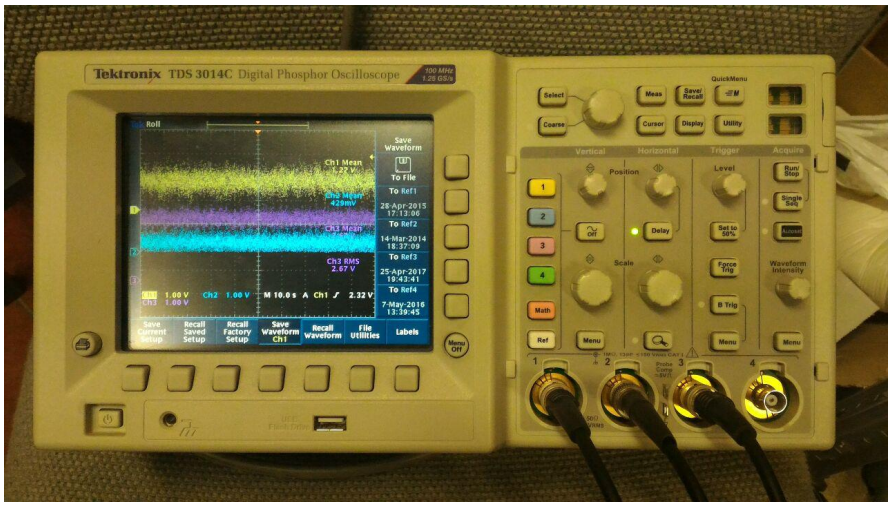

Figure 8.6: Tektronix TDS 3014C Digital Phospor oscilloscope

Although the oscilloscope presented several drawbacks -among them, the impossibility to measure the three forces and three moments at once, requiring two measurements and twice the time for each set of data points-, it provided an immediate way to display and observe the signals, and it allowed for the storage of up to 40s of data on a USB memory device, which could later be used to transfer the resulting .csv files to a computer for processing.

- Incoherent values for **load cell measurements**, with severe differences in the order of magnitude of the aerodynamic loads with respect to the expected results, and strangely aligned forces leading to negative lift or drag values. Initially thought to be due to an incorrect application of the calibration matrix, several attempts at correcting this problem were performed. The axes assigned to the direction of every force and moment were review and changed in a number of occasions, with no impact whatsoever on the behavior of the results; even a trial-and-error analyses of the 36 possible combinations for the axes corresponding to each force and moment could not provide reasonable solutions for any case. Considering that the calibration matrix might not be well adjusted to the current circumstances of the load cell, including the presence of the amplifier, several trials were conducted as well with the experimental calibration matrix proposed in [15], to no avail. The final attempt to derive a new calibration matrix by following

the method detailed in [15] -employing a number of weights to exert controlled forces and moments in given directions, and performing a least squares fitting to relate the voltage data read by the oscilloscope to the known forces and moments for every weight- was not successful, either, in reaching a satisfactory result.

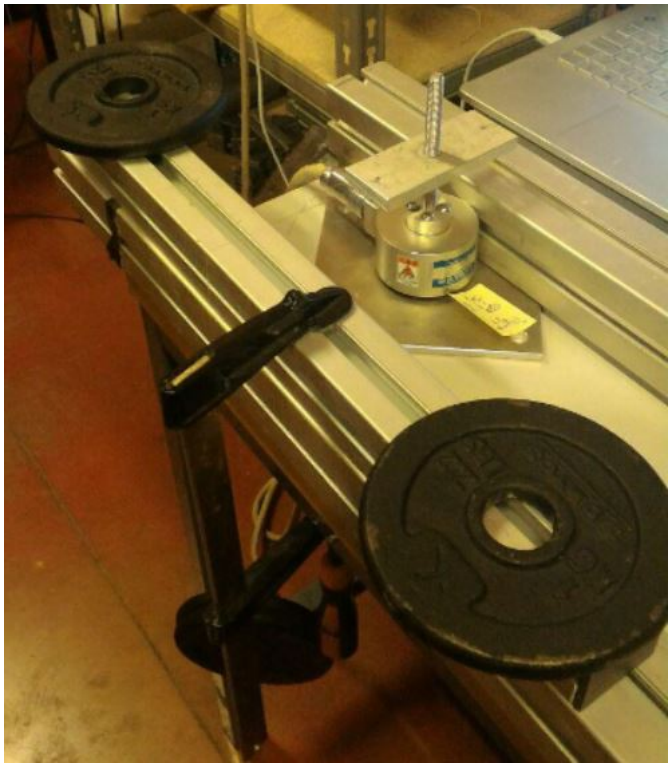

Figure 8.7: Calibration attempt. Application of known weights.

After several failed attempts to obtain values reflecting the actual forces exerting on the wing models, the experimental measurements had to be halted in favor of devoting more time and efforts to the CFD and XFLR5 analyses. The only clear conclusion derived from the experimental study was that changes in wing geometry did, indeed, have an effect on the loads exerted on the wing by the fluid; but it was not possible to distinguish in which ways those changes affected the wing performance, or whether they were due to actual perturbations in the flow caused by the wingtip devices, or appeared as a result of the measurement and calibration errors described above. It is considered that a non-negligible part of the error is due to the amplifier itself: far from the reference output value of 2.5V for an unloaded transducer, data for the three force components oscillated between 1.78 and 2.89V.

8.5 Considerations for future research

Given the extensive challenges encountered during the experimental part of this project, some of which, as described above, led to the paralysis of all empirical research, it is highly recommended that some modifications on the laboratory equipment and practices are applied in the future. Some time and effort should be devoted to preserving and expanding the documentation associated to every instrument, in order to avoid unnecessary delays and confusion in future projects. Software updates and support should be checked regularly, and cleaning and maintenance works for the water channel should not be overlooked. Finally, it is important to remark that the Kyowa LAT-10KA-1 load cell should undergo careful revision, aiming to identify any possible defects or damages on the transducer itself, or to conduct a re-calibration study if necessary.

Figure 8.8: Kyowa LAT1030-KA-1 six-degre force transducer

The purchase of a high-precision voltmeter is strongly recommended, as it would eliminate the error associated to the amplifier; the latter presents, at the moment, the only viable option to measure the signal provided by the load cell. More recent models of six-degree force transducers could also be considered for this task, as many of them include a signal processing unit able to eliminate error due to interference and provide an amplified, clear voltage signal. One such example is found in the Kyowa LAT1030-KA-1 (figure 8.8), rated at 300N, which is particularly suitable for high-precision applications with simultaneous forces on several axes. The data sheet containing the main features and capabilities of this device is included in [47] for reference.

Chapter 9

Analysis of CFD Results

9.1 Aerodynamic efficiency

As it was stated on chapter 5, a total of 22 geometries were modeled, based on existing designs either already employed in the aeronautical industry or undergoing some kind of research towards this purpose. For each of them, at least two simulations were performed in ANSYS Fluent, corresponding to the estimated cruise and takeoff conditions for an aircraft employing a similar wing. Cruise conditions corresponded to a speed of 125m/s at an altitude of 4,575m and an angle of attack $\alpha = 4.26^{o}$, while takeoff conditions were defined by a speed of 50m/s at sea level and angle of attack $\alpha = 10^{o}$. Although significant differences were expected between the results for each of these geometries, three clear observation groups could be defined:

- Distinct geometries, such as the raked wingtip and wingtip fence: unique designs based on known models which were expected to yield small improvements over the aerodynamic efficiency of the basic wing.
- Similar geometries with cumulative modifications: the basic short winglet design was extended in length in order to observe how the L/D ratio was affected by an increase in winglet area; blended winglets aimed to smooth the long winglet geometry to reduce interference drag, and double winglets incorporated a small, downwards winglet to the blended winglet design to prevent more effectively flow recirculation around the wingtip.
- Parameter changes within the same geometry, as it is the case of the Cant angle: short and long winglets were analyzed at six different Cant angles (0^{o}, 15^{o}, 30^{o}, 45^{o}, and 60^{o}), while three values (30^{o}, 45^{o}, and 60^{o}) were employed for the blended and double winglet models.

The first analysis of the results, consequently, was based on how these geometrical differences affected the fluid flow and aerodynamic efficiency for every case, and whether they were affected by changes in altitude and speed. Figure 9.1 shows the aerodynamic efficiency of the wings with short and long winglets, at cruise and takeoff conditions, with the L/D ratio of the basic wing shown for reference.

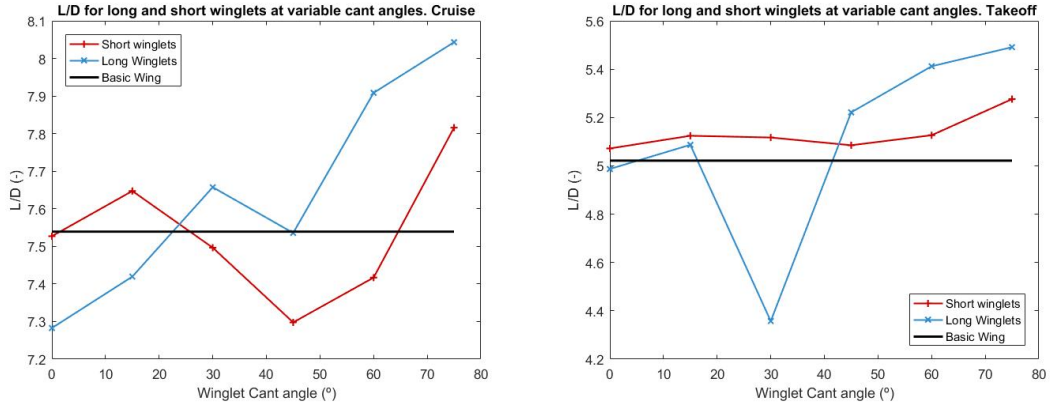

Figure 9.1: Short and long winglet performance at cruise and takeoff conditions

Several conclusions can be drawn from a first observation. Most evidently, there seems to be a significant difference between winglet performance at cruise and takeoff conditions: while in cruise conditions only a given number of geometries display a superior performance to that of the basic wing, in takeoff conditions there are only two configurations falling below the reference L/D. These results seem to confirm the observations repeatedly found in literature that wingtip devices are most effective for takeoff configurations, and might even worsen cruise performance if they are not carefully designed. In both cases and geometries, winglets show an increased aerodynamic efficiency for very low Cant angles, but the L/D ratio undergoes an abrupt fall at intermediate Cant angle values, to rise again at the higher dihedral points. The local maxima and minima seem to vary as well: long winglets at cruise conditions present a local maximum at Cant angles $\Theta = 30^o$ and $\Theta = 45^o$, respectively, but at takeoff conditions these values fall to 15^o and 30^o. Short winglets, however, show a more consistent trend, and seem to be less affected by the change in flight conditions. This seems logical when considering that long winglets cause a stronger disturbance on the flow; the decrease in the Cant angles Θ at which the local maxima and minima are obtained may be due to the higher angle of attack employed in takeoff conditions.

The increase in aerodynamic efficiency observable in the higher Cant angle winglets is quite interesting, since it is a key indicator of the actual effectiveness of wingtip devices in drag reduction. Winglets at high Cant angles cannot increase significantly the lift force on the wing by acting as a span extension, as their counterparts at $\Theta = 0^o$ and $\Theta = 15^o$. This means that the higher aerodynamic efficiency must be caused by a considerable decrease in the drag force acting on the wing: higher Cant angle winglets are more effective in disrupting the wingtip vortices. This behavior can be observed later on the lift and drag coefficient analysis. As for the comparison between short and long winglets, it is undeniable that winglet area plays an important role on aerodynamic efficiency; it is doubtful, however, whether short or long winglets would be more convenient for a general aircraft. Short winglets provide a modest increase in aerodynamic efficiency in takeoff conditions; perhaps they would be more suitable for

short-range aircraft in cases where a greater span extension or changes in structural mass are not desirable. Long winglets at high Cant angles, on the other hand, seem to yield a significant increase in aerodynamic efficiency both in the cruise and takeoff phases, but may cause an excessive increase the bending and torsion moments on the wing. From the point of view of aerodynamic efficiency exclusively, nonetheless, long winglets at Cant angles of $\Theta = 60^o$ or $\Theta = 75^o$ seem to provide by far the best results.

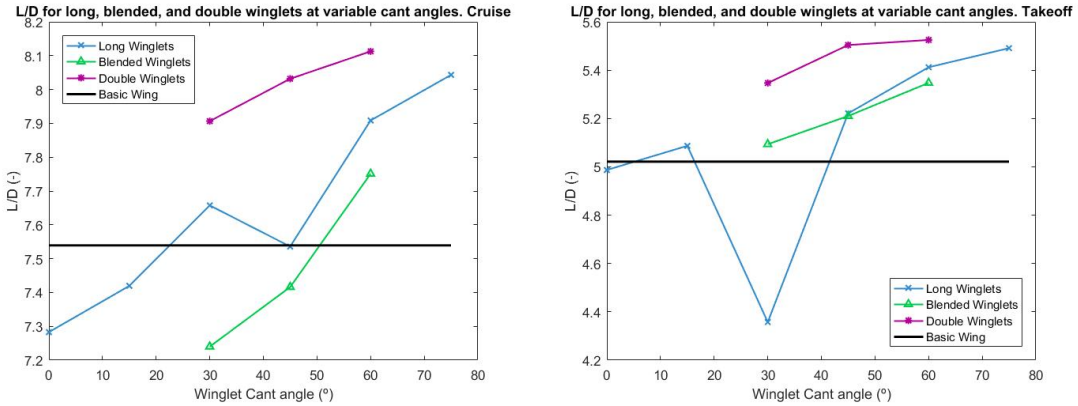

Figure 9.2: Long, blended, and double winglet performance at cruise and takeoff

The comparison of blended winglet to long winglet performance yielded surprising results. Blended winglets, with a curve root design to smooth the union between the wingtip and the winglet, were especially designed to reduce interference drag; they were expected to provide a slightly higher aerodynamic efficiency, with a similar trend. However, as it can be observed in figure 9.2: the L/D ratio decreased significantly for all conditions; as a matter of fact, only the blended winglet at 60^o seemed to provide a better performance than the basic wing at cruise conditions. Although the trend observed in the long winglets is partially maintained, with a higher Cant angle implying a higher aerodynamic efficiency, this sub-par performance was difficult to explain. It was concluded that the effect of interference drag at the wing-winglet union was much lower than initially estimated, and that the curvature imposed on the geometry had a negative effect on the generation on lift. It is also possible that the quality of the mesh was insufficient to account for the effects of interference drag, and that further analysis with a highly refined mesh should be conducted.

As for double winglets, which were an experimental model loosely based on some new designs incorporated by Boeing in civil aircraft, they surpassed initial expectations by providing a significantly high aerodynamic efficiency, overtaking all previous designs. The double winglet at a cant angle of $\Theta = 60^o$ yielded a 9.6% increase in aerodynamic efficiency with respect to the basic wing at cruise conditions and 10% at takeoff conditions, compared to 6.97% and 7.77% for a long winglet at the same cant angle. The most likely explanation for this improvement is the effect of the smaller winglet at a negative cant angle, which, despite not contributing to the lift force, must have been

responsible for preventing flow recirculation much more effectively than positive cant angle winglets, thus reducing induced drag significantly. The increased parasite drag due to this additional surface, which might have hindered its performance, was surely compensated by this effect.

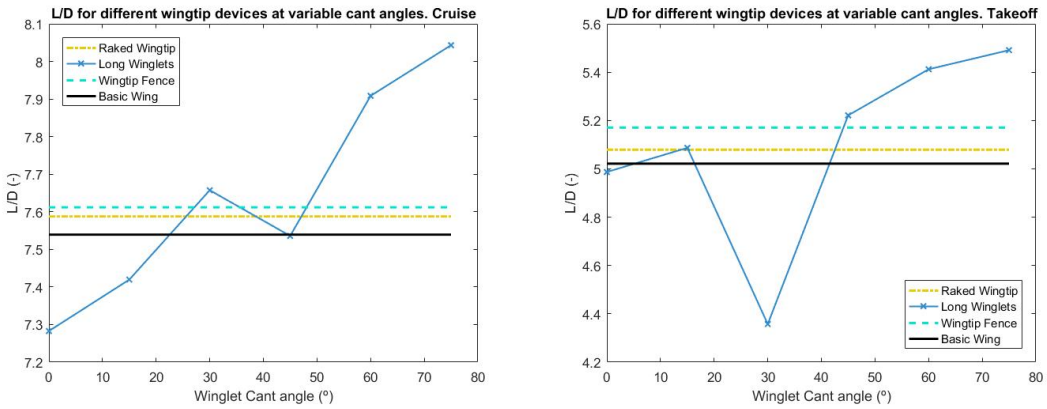

Figure 9.3: Raked wingtip and wingtip fence performance at cruise and takeoff

In figure 9.3, the performance of the raked wingtip and the wingtip fence are shown, along with that of the long winglets and the basic wing for reference. It is quite clear that both designs provide a higher aerodynamic efficiency than the basic wing in both cruise and takeoff conditions, with the wingtip fence yielding a slightly better performance than the raked wingtip in both cases. This difference sets a good example for the importance of the two main factors affecting the aerodynamic efficiency: while the wingtip fence fails to provide additional lift, as it consists of a vertical aerodynamic profile, it effectively prevents the recirculation of the flow. The raked wingtip, on the other hand, acts as a span extension, contributing to the generation of lift, but it performs poorly when attempting to reduce induced drag. The wingtip performance is quite remarkable, since it is comparable to that of the long winglets at $\Theta = 30^o$ in cruise and $\Theta = 45^o$ in takeoff while allowing the wing to maintain the same span. Given that span extensions often entail some complexity for civil aircraft, as they might conflict with the legal framework, it is understandable why wingtip fences have been the default wingtip device in several Airbus families for the last years, as seen in chapter 3. It is important to remark here that the wingtip fence employed in this analysis is an arbitrary design based on those found in the market, and that surely much better results can be obtained with a carefully designed model.

For all the cases shown in this section, it is easy to observe that the aerodynamic efficiency at takeoff conditions is significantly lower than at cruise conditions. This is not due to the reduction in flight velocity or to atmospheric considerations, but to the lift and drag coefficient dependencies on the angle of attack. While the lift coefficient is directly proportional to the angle of attack, adding the contribution for the lift at $\alpha = 0^o$ found in cambered-airfoil wings, the induced drag coefficient is directly proportional to

C_L^2, so that the effect of increasing the angle of attack will be much stronger on the drag force. These changes can be clearly appreciated in figures 9.5 to 9.8 and table 9.1.

To conclude the discussion on aerodynamic efficiency, the results for all the geometries analyzed are shown together for comparison in figure 9.4, where it can be clearly observed that the double winglet at a cant angle $\Theta = 60^o$ yields the best performance in both cruise and takeoff conditions, followed by the long winglet at $\Theta = 75^o$.

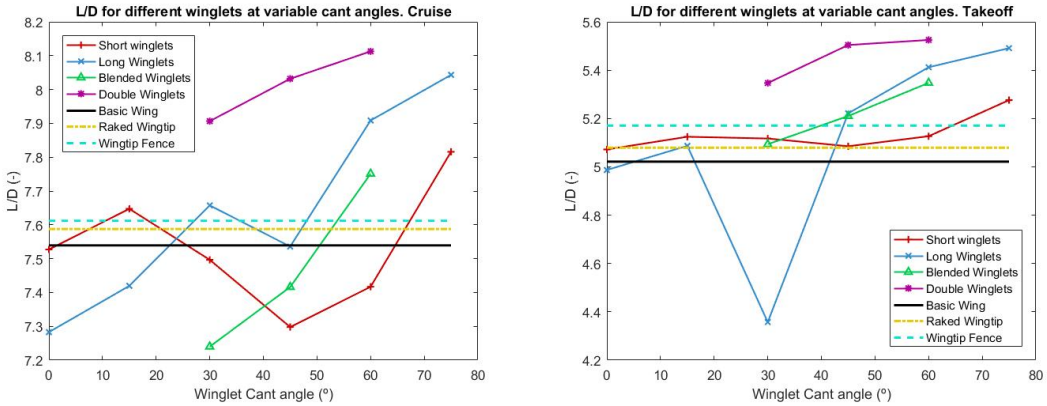

Figure 9.4: Aerodynamic efficiency for all wings at cruise and takeoff

9.2 Lift Coefficient

In order to understand the changes in lift coefficient derived from the addition of wingtip devices, it is necessary to recall the multiple effects of wingtip vortices on the aerodynamic loads acting on the wing. While disturbing these vortices contributes directly to the reduction of induced drag, it also affects directly the lift distribution, since preventing flow recirculation increases the pressure difference between the upper and lower wing surfaces at the wingtips, and thus the net lift force exerted on the wing. This phenomenon provides the explanation for the ascending tendency observed for all variable cant angle wingtip devices: although it would seem logical to see the lift decrease with increasing Θ, this is compensated by a greater pressure difference between wing surfaces, since the closest to 90^o a winglet is located, the more it acts as a *barrier* for the flow.

Figure 9.5 shows a clear example of this effect. The lift for the long winglets increases quite consistently until a cant angle of $\Theta = 60^o$ is reached; at this point, the increase in pressure difference is not enough to compensate for the loss of effective span, and the lift coefficient drops. A similar effect is observed for the short winglets, which, however, show a sharp drop in lift at $\Theta = 45^o$ for cruise conditions and $\Theta = 30$ for takeoff conditions. There are two possible explanations for this anomaly: either the same effect described above applies, and at that value of Θ the regulation of the pressure difference

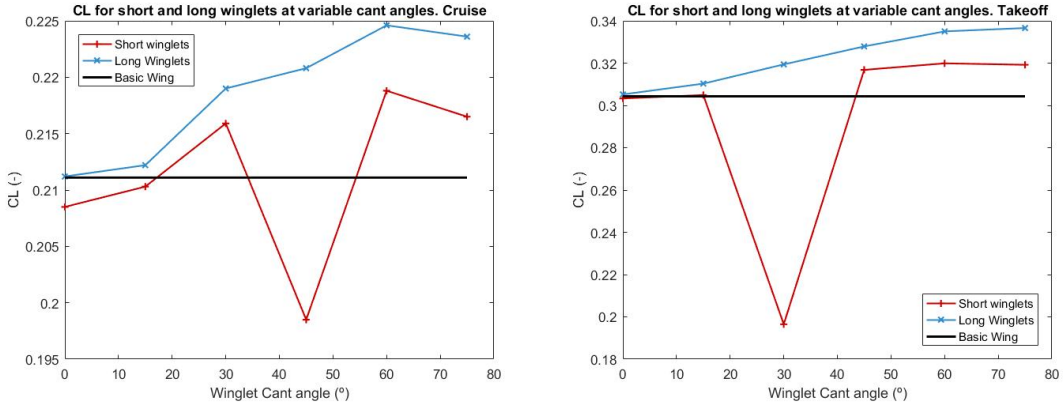

Figure 9.5: Lift coefficient for short and long winglets at cruise and takeoff

is not enough to compensate for the losses, or, most likely, the combination of angle of attack and cant angle causes a part of the wing or winglet to enter stall; but further research would be needed in this regard. As expected, long winglets provide more lift than short winglets for all cant angles and flight conditions, and the lift coefficient of the wing with winglets is higher than for the basic wing in all cases except for the sharp drops mentioned above.

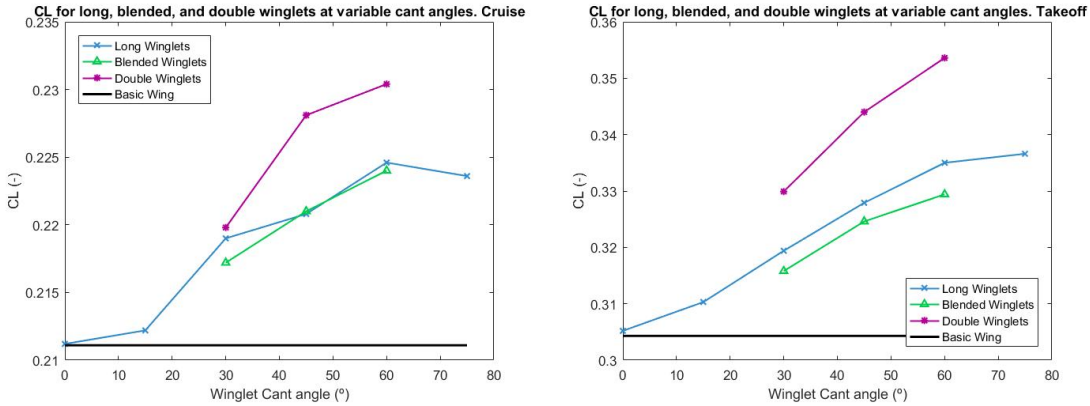

Figure 9.6: Lift coefficient for long, blended, and double winglets at cruise and takeoff

The same ascending tendency is observed in figure 9.6 for the blended and double winglets, although there are insufficiency samples of this geometry to venture further in their discussion. It can be observed that both provide lift coefficient values significantly higher than those of the basic wing, and that double winglets, again, seem to cause a significant improvement over long and blended winglets; this is probably due to their ensuring a higher pressure difference in addition to the increase in effective span. As for blended winglets, they seem to fall behind long winglets in terms of lift as well, perhaps due to their curvature.

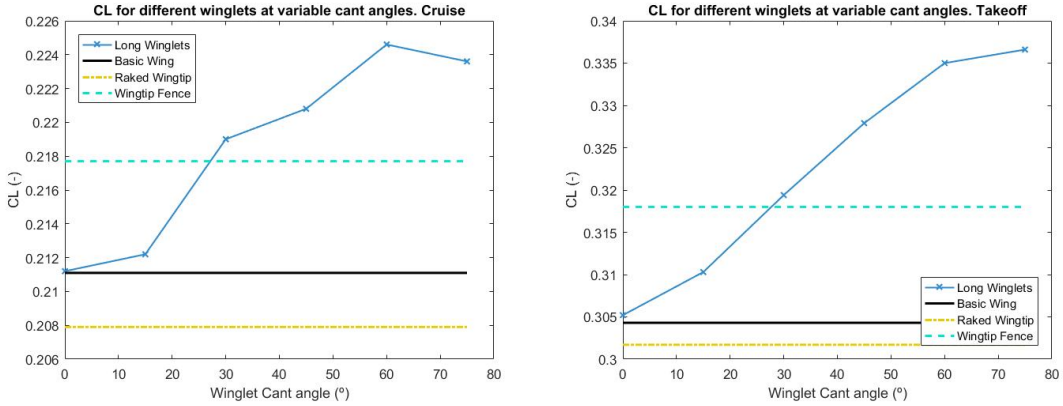

Figure 9.7: Lift coefficient for raked wingtip and wingtip fence at cruise and takeoff

Figure 9.7 offers another example of this phenomenon. The wingtip fence, which does not act as a span extension unlike all other wingtip devices considered in this work, provides a higher lift coefficient than the basic wing, even if slightly, due to its preventing flow recirculation around the wingtip. The raked wingtip, on the other hand, fails to keep this pressure difference, and thus presents a slightly lower value.

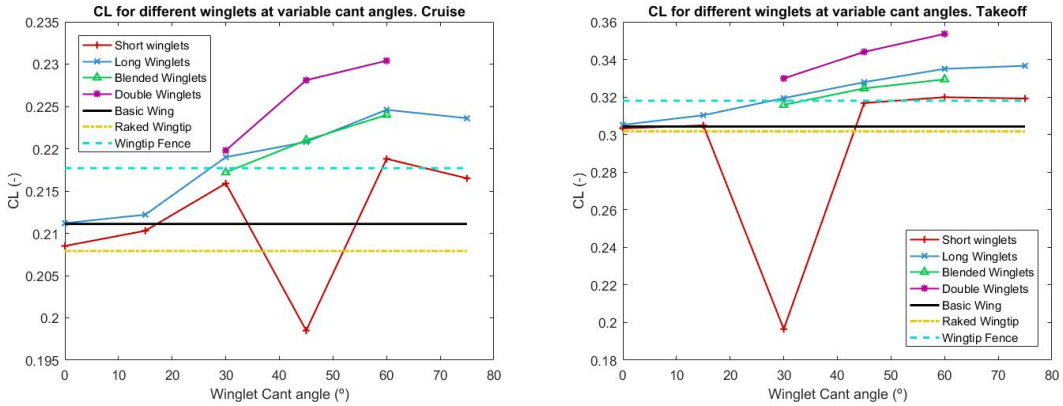

Figure 9.8: Lift coefficient for all geometries at cruise and takeoff

The evolution of the lift coefficient for all wingtip devices is gathered in figure 9.8, where it can be observed that, as in the case of the aerodynamic efficiency, the double winglet at $\Theta = 60^{o}$ provides the best performance for all conditions, followed, in this case, by the long winglet at $\Theta = 60^{o}$. Finally, it is useful to give some thought to the fact that the lift coefficient is significantly higher at takeoff conditions than in the cruise cases. As it was stated before, this is due to the higher angle of attack employed in the takeoff case, which affects the lift coefficient directly. Takeoff conditions also seem to provide smoother C_L vs. Θ curves for all winglets.

9.3 Drag coefficient

The drag coefficient values presented in this section might seem counterintuitive at first sight. Up to this point, the role of wingtip devices on reducing drag has been emphasized repeatedly, being the driving concept behind the motivation for winglet design. However, when studying the drag coefficient values obtained from the Fluent simulations, it can be observed that, for most cases, the drag coefficient increases when compared to the basic geometry. Such is the case of the short and long winglets, shown in figure 9.9, which seem to exhibit a quite chaotic behavior with drag coefficients generally higher than the reference value for the basic wing.

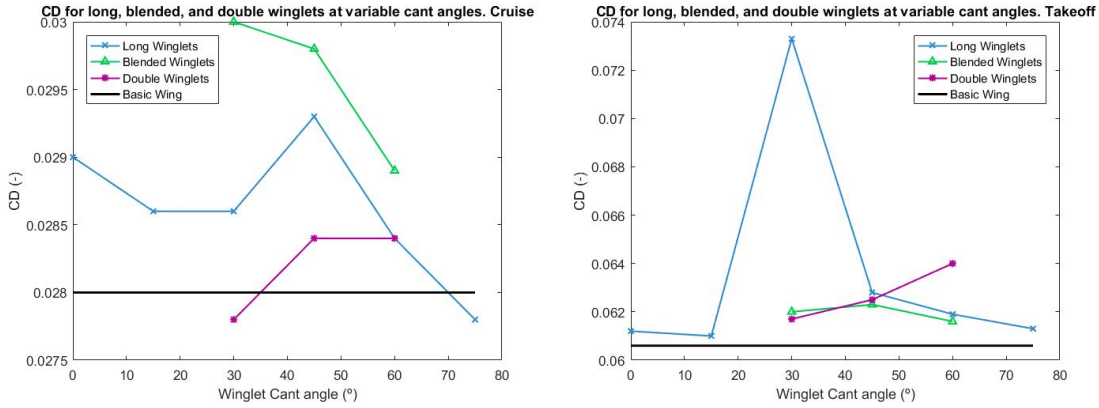

Figure 9.9: Drag coefficient for long, blended, and double winglets at cruise and takeoff

However, to find an explanation to this behavior it is necessary to remember that the parabolic drag polar states that the drag coefficient is formed by the sum of parasitic and induced drag, where the parasitic drag is a constant for every wing geometry and the induced drag coefficient C_{D_i} is given by:

$$C_{D_i} = C_{D_0} + kC_L^2 \tag{9.1}$$

While the parasitic drag value does vary with the wing geometry, the simulations performed for several wings at their zero-lift angle of attack, $\alpha_{C_L=0}$, yielded variations of the order of 0.001, with parasitic drag coefficient values ranging from $C_{D_0} = 0.0140$ for the basic wing to $C_{D_0} = 0.0154$ for the wing with a long winglet at $\Theta = 60^o$. The main parameter affected by the addition of wingtip devices was k. As a matter of fact, for the parasitic drag coefficient value just presented, the value of k decreased from 0.3225 for the basic wing to 0.2784 for the wing with a double winglet at $\Theta = 60^o$. Thus, the main consequence of the incorporation of wingtip devices is a decrease in the *impact* of the induced drag component on the total drag; and the higher drag values shown in the figure above are due to the increase in lift coefficient, which appears as a second order term on the parabolic drag equation. On a side note, it was found that parasitic drag amounted to approximately 50% of the total drag in cruise conditions, and approximately 23% in takeoff conditions, which seems quite consistent with the

typical percentages found in literature and emphasizes the importance of induced drag during the takeoff phase.

Case	$C_{L_{CR}}$	$C_{D_{CR}}$	L/D_{CR}	$C_{L_{TO}}$	$C_{D_{TO}}$	L/D_{TO}	$\Delta L/D_{CR}$ (%)	$\Delta L/D_{TO}$ (%)
Basic	0.2111	0.0285	7.40	0.3043	0.0606	5.02	-	-
SW00	0.2085	0.0277	7.53	0.3033	0.0598	5.07	1.81	1.00
SW15	0.2013	0.0275	7.64	0.3049	0.0595	5.12	3.24	2.08
SW30	0.2159	0.0288	7.41	0.1965	0.0384	5.12	1.43	2.03
SW45	0.1992	0.0272	7.32	0.3168	0.0623	5.08	-1.13	1.22
SW60	0.2188	0.0295	7.42	0.3199	0.0624	5.13	0.25	2.18
SW75	0.2165	0.0277	7.82	0.3192	0.0605	5.28	5.67	5.12
LW00	0.2112	0.0290	7.29	0.3052	0.0612	4.99	-1.49	-0.60
LW15	0.2122	0.0286	7.41	0.3103	0.0610	5.09	0.20	1.31
LW30	0.2190	0.0286	7.65	0.3194	0.0733	4.35	3.38	-13.25
LW45	0.2208	0.0293	7.53	0.3279	0.0628	5.22	1.70	4.01
LW60	0.2246	0.0284	7.92	0.3350	0.0619	5.41	7.04	7.82
LW75	0.2236	0.0278	8.06	0.3366	0.0613	5.49	8.86	9.29
BW30	0.2172	0.0300	7.24	0.3158	0.0620	5.10	-2.17	1.50
BW45	0.2210	0.0298	7.42	0.3246	0.0623	5.21	0.26	3.71
BW60	0.2240	0.0289	7.75	0.3294	0.0616	5.35	4.80	6.56
DW30	0.2198	0.0278	7.91	0.3299	0.0617	5.35	6.84	6.54
DW45	0.2281	0.0284	8.04	0.3440	0.0625	5.50	8.70	9.66
DW60	0.2304	0.0284	8.12	0.3536	0.0640	5.53	9.67	10.08
Raked	0.2079	0.0274	7.59	0.3017	0.0594	5.08	2.58	1.23
Fence	0.2177	0.0286	7.60	0.3180	0.0615	5.17	2.74	3.02
Multi	0.2164	0.0267	8.12	0.3253	0.0596	5.46	9.69	8.69

Table 9.1: Lift and drag coefficient and aerodynamic efficiency values for all geometries

The results presented in Table 9.1 are quite promising: several wing+winglet configurations provided increments in aerodynamic efficiency of more than 5% in both cruise and takeoff conditions, as is the case of the short winglets at $\Theta = 75^{o}$, the long winglets at $\Theta = 60^{o}$ and $\Theta = 75^{o}$, all double winglets, and the multi-winglet. These values prove the convenience of incorporating wingtip devices to aircraft design from an aerodynamic standpoint, as it has become commonplace in the aeronautical industry in the last years.

Some comments must be dedicated to the multi-winglet geometry, which has not been mentioned up to this point in this analysis. This is mainly due to its being an experimental, largely arbitrary model whose structural validity is still questionable. However, it is necessary to remark here that its results in terms of aerodynamic efficiency have been surprising, showing a L/D ratio equal to that of the double winglet at $\Theta = 60^{o}$ at cruise conditions and among the highest for takeoff conditions. While it yielded a very modest lift coefficient, its drag coefficient ranked among the lowest at takeoff conditions and was the minimum C_D at cruise conditions, indicating a greater ability to disturb the wingtip vortices than most single winglet models. It is likely that an actuated, variable

cant angle multi-winglet design, closer to the tip feathers found in raptor wings, would cause a much more significant drag reduction.

9.4 Wingtip vortex reduction

Figures 9.10 to 9.13 show the contours of vorticity, $\omega = \nabla \wedge \vec{V}$, at a plane perpendicular to the chordwise direction, located at a distance $x = 8m$ from the leading edge at the wing root. The initial wingtip vortex can be observed quite clearly in figure 9.10, appearing as a high vorticity region just above the wingtip; farther downstream, an increase in radius along with a decrease in core strength can be observed, until it finally vanishes in the wake.

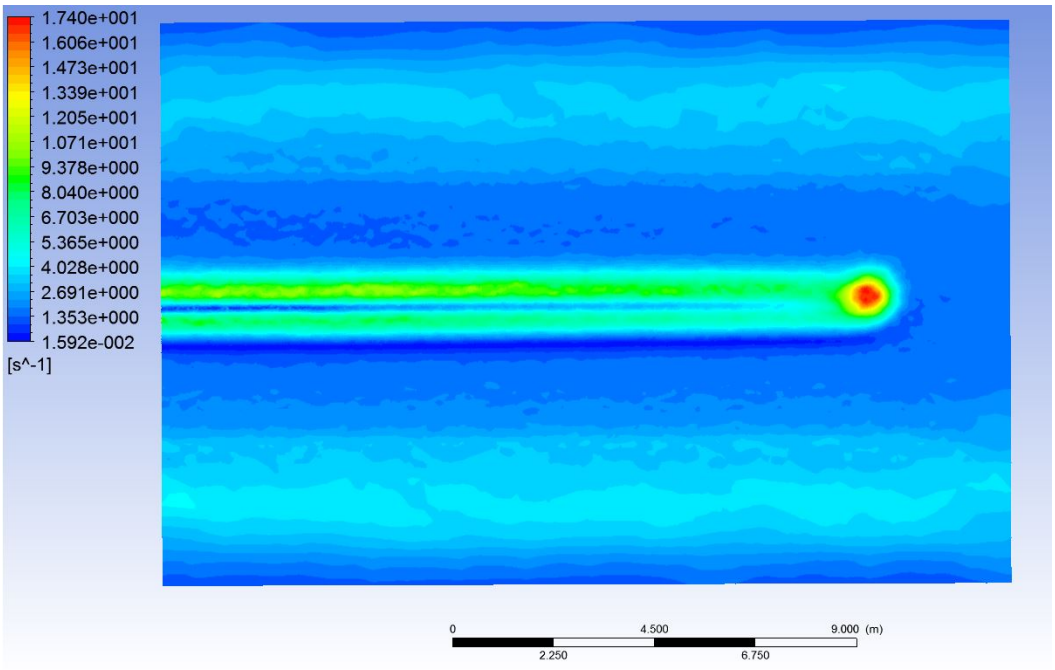

Figure 9.10: Contours of vorticity for the basic wing

The effect of incorporating a winglet in the geometry is very clear, as it can be observed in figures 9.11 and 9.12. In the long winglet at $\Theta = 60^o$, the wingtip vortex is disturbed in such a way that two smaller vortices appear, with a similar radius but a much lower strength; the vorticity at their core is comparable to some found on some regions of the wake near the wing root, and its overall value has decreased. This effect is enhanced for the double winglet at $\Theta = 60^o$, for which the vorticity at the wingtip vortex core is much lower than in the near-root wake. The double winglet has the additional effect of spreading out these vortices over its lower surface, weakening them significantly. The best example of this behavior is the multi-winglet geometry shown in figure 9.13, for which the vortices become as weak as to partially disappear in the surrounding flow.

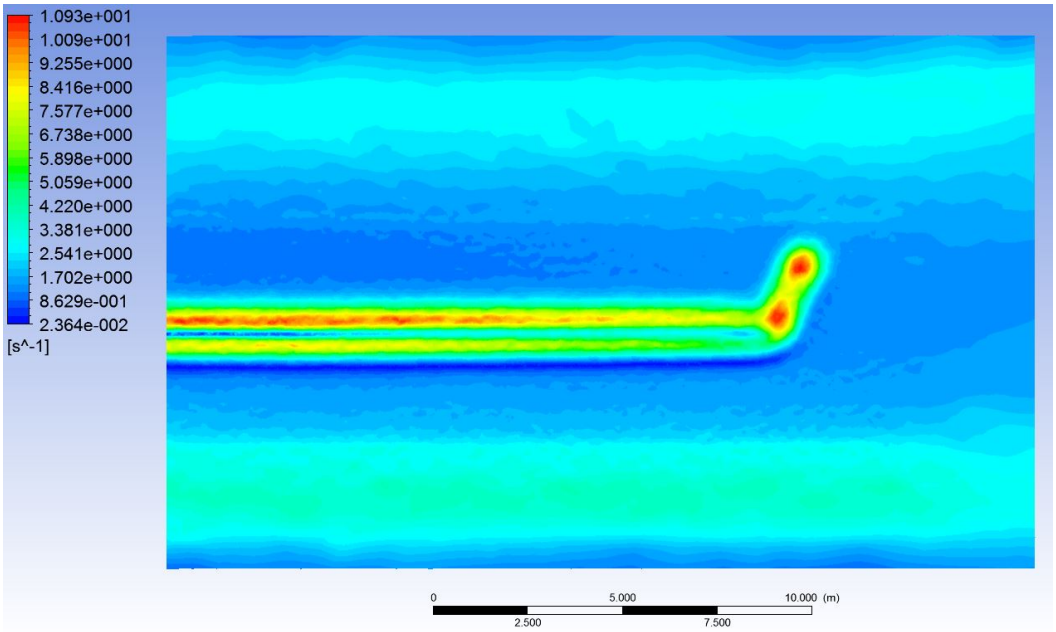

Figure 9.11: Contours of vorticity for the wing + long winglet at $\Theta = 60^{o}$

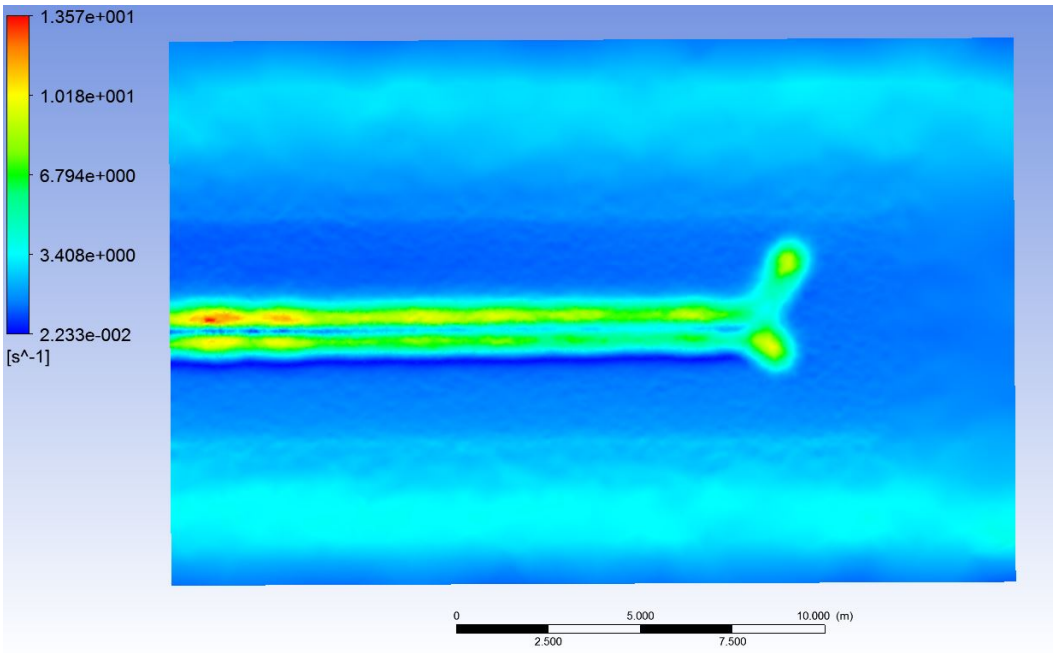

Figure 9.12: Contours of vorticity for the wing + double winglet at $\Theta = 60^{o}$

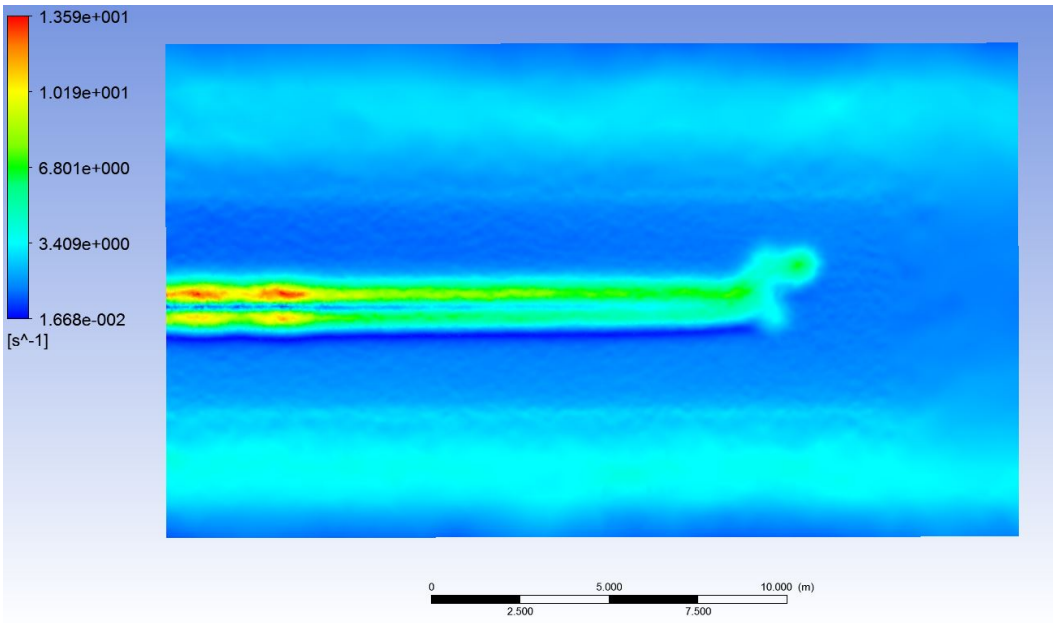

Figure 9.13: Contours of vorticity for the wing + multi-winglet

9.5 Mission performance

Although the data corresponding to the lift and drag coefficients and aerodynamic efficiency has been presented in previous sections, it seemed necessary for this study to consider the effect that variations on these parameters might have on real-world applications. For this purpose, as it was described in chapter 7, several example missions were designed for an aircraft employing the wing geometries considered.

- **Range assessment mission**: a simple cruise mission created to study how an increase in aerodynamic efficiency would affect the maximum range attainable by the aircraft, with reference masses MTOM=16,500 kg, MZFM=15,000 kh, OEM=9,450kg, and MF=4,230kg. The results are reflected on the payload-range diagram shown in figure 9.14, drawn for the basic wing, the wing with long winglets at $\Theta = 60^o$, and the wing with a double winglet at $\Theta = 60^o$. It can be observed that, as expected, the double winglet at 60^o provides a greater range than the long winglet at 60^o, and that the maximum range in both configurations is greater than that for the basic wing. The corresponding values are gathered in Table 9.2:

Case	R_1 (nm)	R_2 (nm)	R_3 (nm)	ΔR_1 (%)	ΔR_2 (%)	ΔR_3 (%)
Basic	144.9	1030.7	1352.6	-	-	-
LW60	164.7	1112.7	1457.2	13.66	7.96	7.73
DW60	172.3	1144.3	1497.5	18.91	11.02	10.71

Table 9.2: Range for every geometry and point in the PL/R diagram

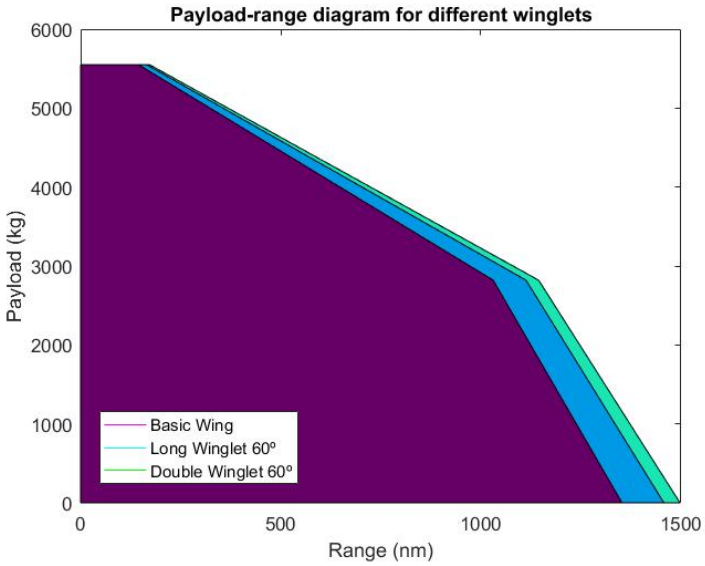

Figure 9.14: Payload-range diagram for different winglet configurations

As it can be observed, the increase in aerodynamic efficiency provided by the winglets provides roughly the same percentage increase in range at points R_2 and R_3, while yielding a significantly greater range at R_1. This seems to imply that the effect of winglets on range is greater for heavily loaded aircraft close to their maximum payload, while their contribution becomes more modest where payload mass is transferred to fuel mass. These results should be considered cautiously since the aerodynamic efficiency for the loiter phase included in the mission has been estimated, lacking the required data; but it can be concluded that wingtip devices have a beneficial effect on range determined by the increase in aerodynamic efficiency they provide at cruise conditions.

- **Endurance assessment mission**: a simple mission with cruise, loiter, and cruise-back phases for a fixed range of 200km, aiming to obtain the maximum endurance for the loiter phase. The results are quite similar to those found for range, with some of the most significant gathered in table 9.3.

Case	E (min)	ΔE (%)
Basic	173.8	-
LW60	187.2	7.71
LW75	190.8	9.78
DW60	192.3	10.64
Raked	178.7	2.82
Fence	178.9	2.93

Table 9.3: Endurance for every wing+winglet geometry

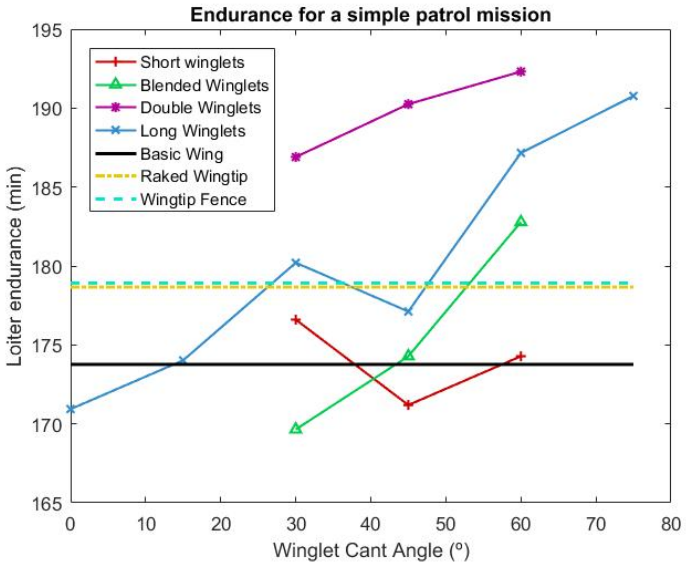

Figure 9.15: Endurance for several wing configurations

As figure 9.15 shows, both the raked wingtip and wingtip fence provide a modest improvement in endurance, while long and double winglets at high cant angles -$\Theta = 60^o$ and $\Theta = 75^o$- can provide up to an estimated additional 18 minutes in flight for the same fuel, payload, and empty mass. As in the case of the range, these results are not meant to reproduce real-world conditions, but to provide a first approximation to the benefits of including wingtip devices in wing designs.

- **Take-off field length and landing distance**

  As explained in chapter 7, the takeoff field length is related to a number of flight parameters, among them the wing loading and atmospheric density ratio; and it is inversely proportional to the maximum lift coefficient, which was obtained as $C_{L_{max}} = 1.33C_L$ at takeoff conditions. Consequently, any increase in lift coefficient should lead to a proportional decrease in takeoff field length. This can be observed in figure 9.16 for a reference takeoff field length of 1500m; as expected, the wing configurations providing the highest lift coefficients are those for which a shorter takeoff field length is necessary. It is interesting to note that the raked wingtip is the only design increasing, even if slightly, the TOFL; this, together with the increased span, might hypothetically become troublesome for some aircraft in terms of airport operation.

  As for the landing distance estimation, the increase in lift coefficient affected the ground roll distance directly, while the approach distance, usually fixed through regulations, was kept constant. Assuming an approach distance $S_a = 183m$, as typical for a general aircraft on a power-off approach, as well as a reference

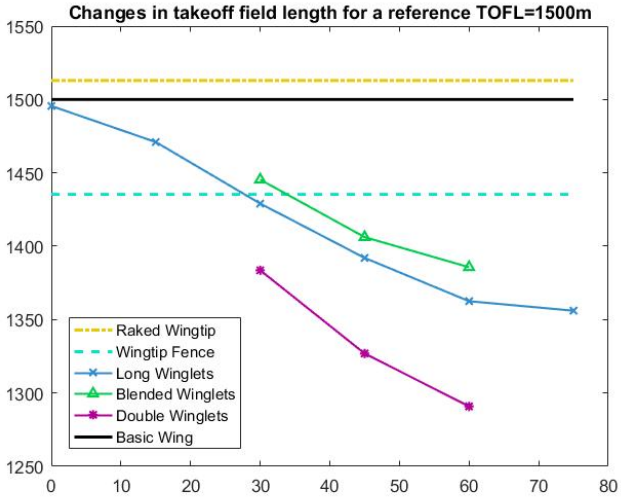

Figure 9.16: Takeoff field length for several wing configurations

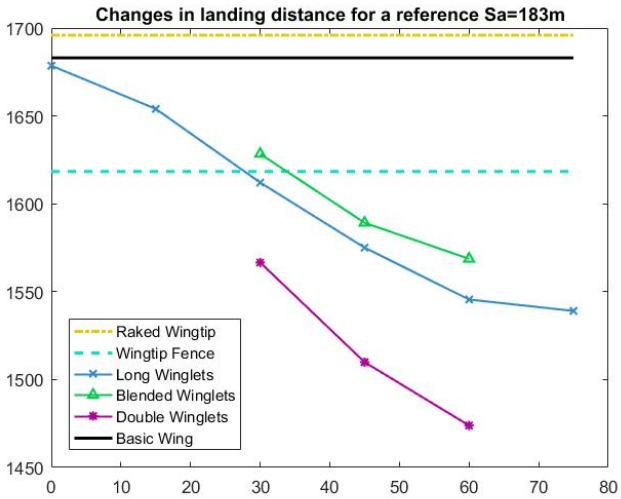

Figure 9.17: Landing distance for several wing configurations

landing distance $S_L = 1500m$, the comparison of wing configurations yields the same pattern as for the takeoff field length, as displayed in figure 9.17. It is important to remember, however, that in the lift coefficient of a complete aircraft the contribution of the wingtip devices will likely represent a lower percentage of the total due to the other lifting surfaces present, and the reduction in takeoff field length and landing distance might not be as significant as in this example.

Chapter 10

Analysis of XFLR5 Results

10.1 Cant angle effects on aerodynamic efficiency

Given the limitations presented by the 3D panel method embedded in XFLR5, already discussed in chapter 6, the analysis discussed in this chapter was only performed for the short and long winglets at the customary cant angles of $\Theta = 0^o$, 15^o, 30^o, 45^o, 60^o, and 75^o. The effect of varying the cant angle on the aerodynamic efficiency was studied for the takeoff and cruise cases, at a range of angles of attack $\alpha \in [-5^o, 12^o]$, and at velocities $U_\infty = 50m/s$, $U_\infty = 80m/s$, and $U_\infty = 100m/s$ for takeoff conditions, and $U_\infty = 80m/s$, $U_\infty = 100m/s$, and $U_\infty = 125m/s$ for cruise conditions. The severe handicaps found in XFLR5 for the analysis of three-dimensional flows, particularly the underestimation of the drag force due to the flat wake model, limits the consideration of these results to a qualitative overview of the flow behavior, serving only as a complement of the more exhaustive numerical analysis detailed in the previous chapter.

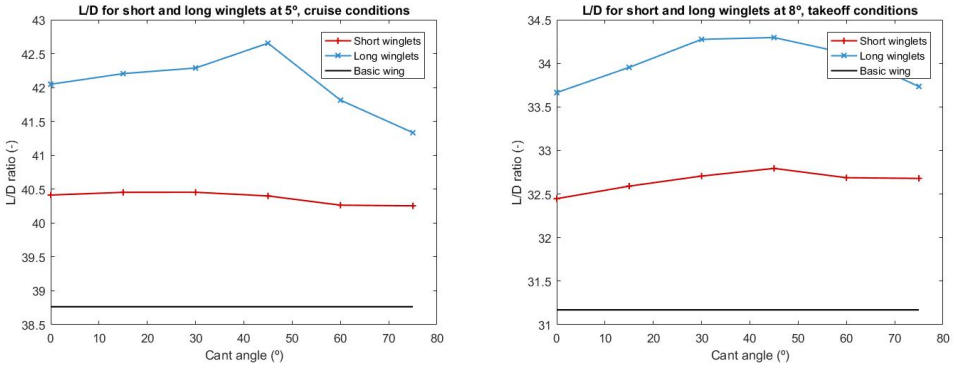

Figure 10.1: L/D ratio for all winglets at standard cruise (left) and takeoff conditions

The first parameter considered in the analysis of the results was the winglet area, together with the effect of the cant angle Θ on the aerodynamic efficiency for the standard takeoff and cruise conditions. Figure 10.1 shows the clear difference existing between the short and long winglet geometries, with long winglets showing a superior aerodynamic efficiency in both cases. The effect of the cant angle is similar to that observed in the

Fluent results, with the L/D ratio increasing with cant angle until a local maximum is reached, and then falling with a higher slope. While in the previous case an ascending tendency was found after a local minimum, this behavior is not present for the XFLR5 data; this, as many other differences between the two sets of results, is likely due to the fact that XFLR5 fails to model adequately the effect of the wingtip vortices. In this case, unlike in Fluent, the local maximum appears at 45º for both flight conditions and winglet types. The values obtained for the aerodynamic efficiency are much higher than initially expected, but this is most likely due to the problems associated to viscous drag modeling described in [48].

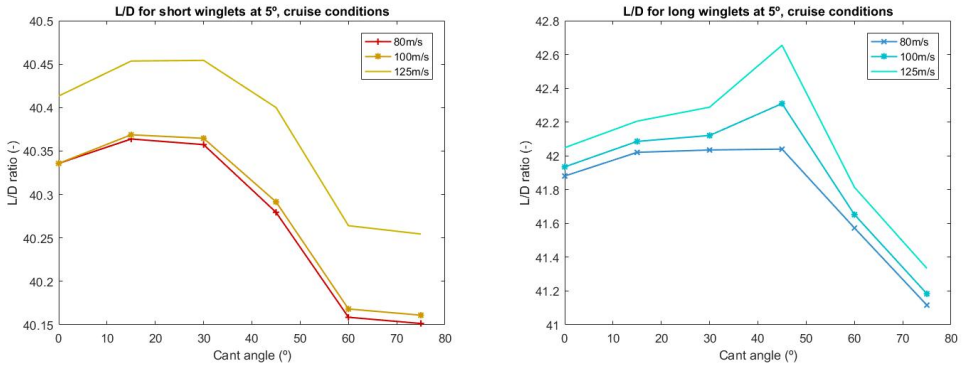

Figure 10.2: L/D ratio for short and long winglets at standard cruise conditions

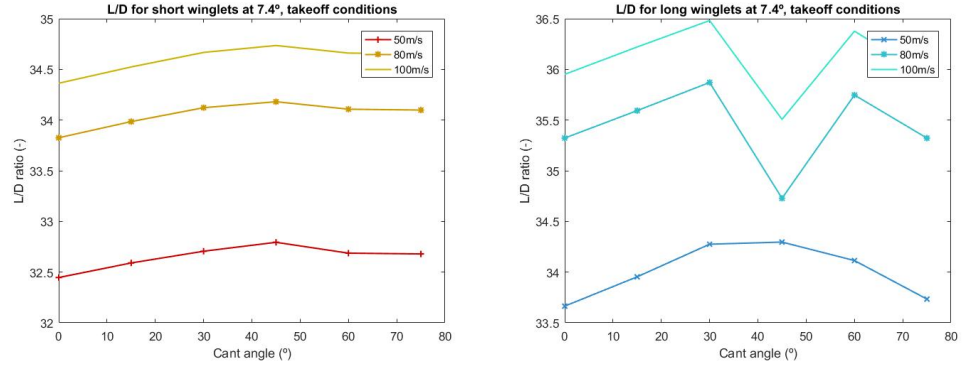

Figure 10.3: L/D ratio for short and long winglets at standard takeoff conditions

Figures 10.2 and 10.3 show the behavior of long and short winglets, separately, at the altitude and angle of attack corresponding to cruise and takeoff conditions, but with significant differences in flight speed. It can be appreciated that clear differences exist, particularly important at the higher angle of attack $\alpha = 7.4^{o}$ at sea level. Since the lift coefficient is not affected by flight speed, being only influenced by the angle of attack, and the induced drag coefficient, k, is purely related to the geometry of the wing, these variations must be due to changes in the parasitic drag coefficient C_{D_0}. As a matter

of fact, most estimations relate the parasitic drag coefficient to the wetted area and friction coefficient of the aircraft, such as that provided by Kundu [18]:

$$C_{D_0} = \frac{\Sigma S_{wet} C_f}{S_{ref}} \tag{10.1}$$

The friction coefficient C_f is, in turn, directly influenced by the flow regime, as described in chapter 6. The flat plate analogy typically employed for conventional wings yields a friction coefficient inversely proportional to $Re^{0.2}$ for turbulent boundary layers, as:

$$C_f = \frac{0.058}{Re^{\frac{1}{5}}} \tag{10.2}$$

and, since, in turn, the Reynolds number is computed as

$$Re = \frac{\rho U_\infty L_c}{\mu} \tag{10.3}$$

it is only logical to see the parasitic drag coefficient vary to some extent when flight velocity. The exact relationship between aerodynamic efficiency and flight velocity is difficult to determine, since the friction coefficient is highly dependent on the characteristics of the boundary layer, and it would require an estimation of the relative extent of the laminar and turbulent flow regimes over the wing, as well as the transition and separation points. Although several approaches to this estimation can be found in literature [2, 18], a much more detailed study should be performed to derive clear conclusions. For the purposes of this work, it is sufficient to observe that the aerodynamic efficiency increases slightly with flight speed, and that this variation can be explained through the influence of the Reynolds number on parasitic drag. Since these variations are two orders of magnitude smaller than the aerodynamic efficiency itself, it would be safe to assume the parasitic drag coefficient to be constant with speed for an initial estimate.

It must be noted that, as shown in figure 10.1, XFLR5 results provide a greater L/D ratio for any wing+winglet configuration than for the basic wing, probably due to the effects of the increased span in an overestimated lift coefficient.

10.2 Altitude effects on aerodynamic efficiency

The variations of aerodynamic efficiency with altitude, much as the variations with velocity explained in the previous section, are due to the influence of the Reynolds number on the parasitic drag coefficient, as the lift coefficient is only given by

$$C_L = C_{L_\alpha} \alpha + C_{L_{\alpha=0}} \tag{10.4}$$

and thus not affected by changes in fluid properties. Considering the international standard atmosphere model at reference conditions, ISA+0, the density at an altitude h is given by:

$$\rho = \rho_0 \cdot \theta^{4.2561} \tag{10.5}$$

where $\rho_0 = 1.225 kg/m^3$, and:

$$\theta = \frac{T}{T_0} = 1 - 2.25569 \cdot 10^{-5} \cdot h \tag{10.6}$$

begin $T_0 = 288.15K$. The dynamic viscosity μ, on the other hand, is obtained through:

$$\mu = \frac{1.458 \cdot 10^{-6}\sqrt{T}}{1 + \frac{110.4}{T}} \tag{10.7}$$

When comparing the evolution of density ρ and dynamic viscosity μ with altitude, it can be observed that the variations in density are much greater, falling from $\rho_0 = 1.225 kg/m^3$ at sea level to $\rho = 0.736 kg/m^3$ at $h = 5,000m$, while those in viscosity are somewhat modest: from $\mu_0 = 1.7894 \cdot 10^{-5} N \cdot s/m^2$ at sea level to $\mu = 1.6281 \cdot 10^{-5} N \cdot s/m^2$ at $h = 5,000m$.

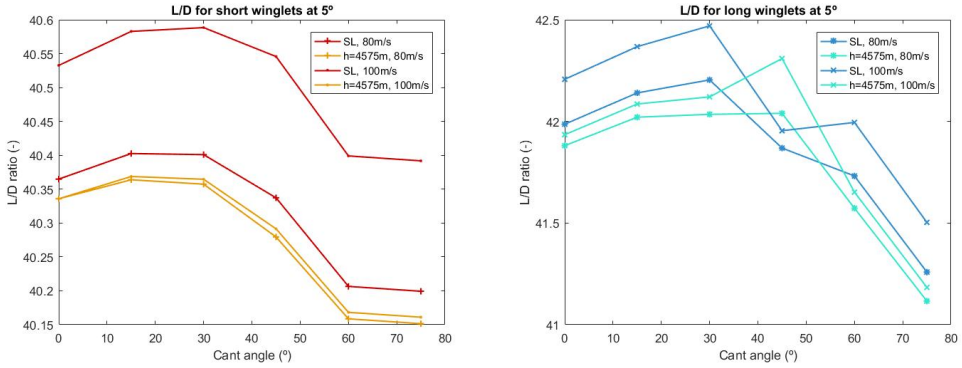

Figure 10.4: L/D ratio for short and long winglets at different altitudes

Given this fact, it would seem logical that the variations in density partially compensated those in viscosity, and that the resulting variation in parasitic drag coefficient appeared as a combination of these two effects. As it can be observed in the results shown in figure 10.4, for the vast majority of cant angles Θ the aerodynamic efficiency is higher at sea level conditions than at $h = 4,575m$. As observed with the variations due to flight speed, the changes seem to be very small in both cases; it is interesting to observe that at sea level the difference between the aerodynamic efficiencies at two different flight velocities is greater than at $h = 4,575m$.

The shift in maximum aerodynamic efficiency found in long winglets was considered remarkable: while in sea level conditions it appeared at $\Theta = 30^o$ for both velocities, at cruise altitude it took place at $\Theta = 45^o$. In order to study this phenomenon in greater depth, a number of additional analyses were performed for all the wings considered in this study, at altitudes of 1000m, 2000m, 3000m, 4000m, 5000m, and 6000m. In

an attempt to observe in more detail the wing+winglet configurations at cant angles between $\Theta = 30^o$ and $\Theta = 60^o$, three more geometries were defined at angles $\Theta = 35^o$, $\Theta = 40^o$, and $\Theta = 50^o$. The results of this analysis can be observed in figures 10.5 and 10.6, for short and long winglets at two different angles of attack and a constant speed $U_\infty = 100m/s$.

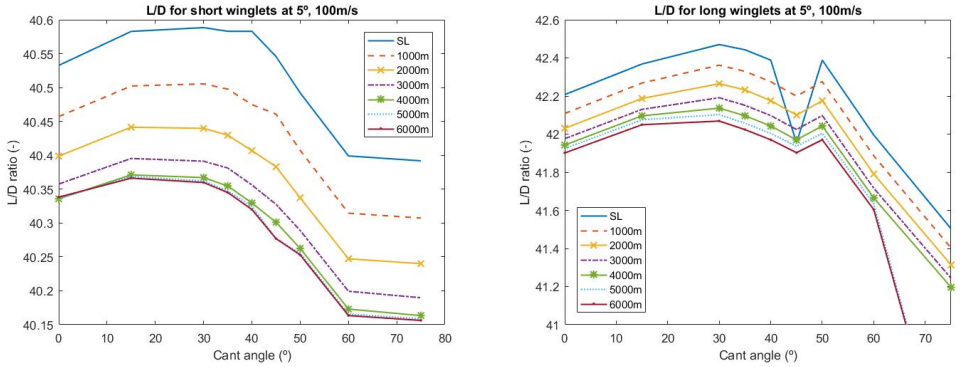

Figure 10.5: L/D ratio for short and long winglets at different altitudes, $\alpha = 5^o$

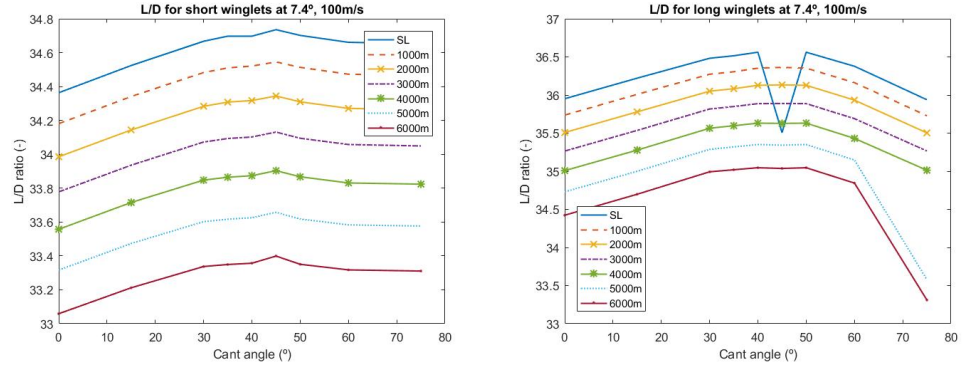

Figure 10.6: L/D ratio for short and long winglets at different altitudes, $\alpha = 7.4^o$

As shown in the figures above, for the more detailed analysis of altitude variations it becomes clear that aerodynamic efficiency increases slightly with altitude, confirming the trend observed in figure 10.4. However, it is also possible to observe that the unusual variation of the cant angle at which the maximum L/D ratio was found was, in fact, due to an anomaly in a specific simulation. The behavior of the wing configurations shown here seem to suggest that the aerodynamic efficiency is maximum at $\Theta = 30^o$ for long winglets at $\alpha = 5^o$; $\Theta = 45^o$ for short winglets at $\alpha = 7.4^o$, and $\Theta = 50^o$ for long winglets at $\alpha = 7.4^o$. While there is a slight variation in the short winglets at $\alpha = 5^o$, with $\Theta_{LD_{max}}$ switching from 30^o to 15^o beyond an altitude $h = 2000m$, the difference between L/D values is too small to draw any significant conclusions. The

XFLR5 results seem to suggest that altitude has little or no impact on the winglet cant angle for optimum performance.

It must be emphasized here that these results must be considered merely illustrative for this particular case, and that a better estimation of the lift and drag coefficients, particularly concerning viscous effects and boundary layer separation, would be required in order to draw more accurate conclusions.

10.3 Angle of attack and aerodynamic efficiency

While in previous sections the aerodynamic efficiency changed exclusively as a result of the variations in parasitic drag due to differences in the flow regime, in this case the lift coefficient was, as well, affected. As a matter of fact, the variations in the angle of attack had, by far, the greatest effects on aerodynamic efficiency for the same wingtip device geometry; while the variations in previous cases were of $O(10^{-1})$, in this case they were an order of magnitude greater.

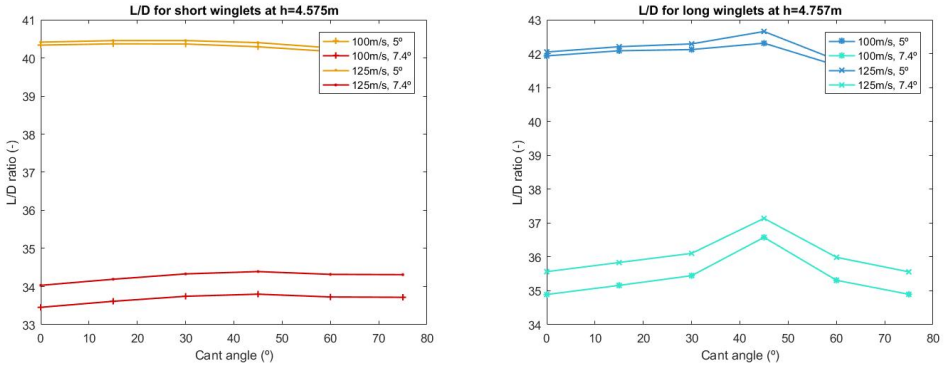

Figure 10.7: L/D ratio for short and long winglets at different α. h=4,575m

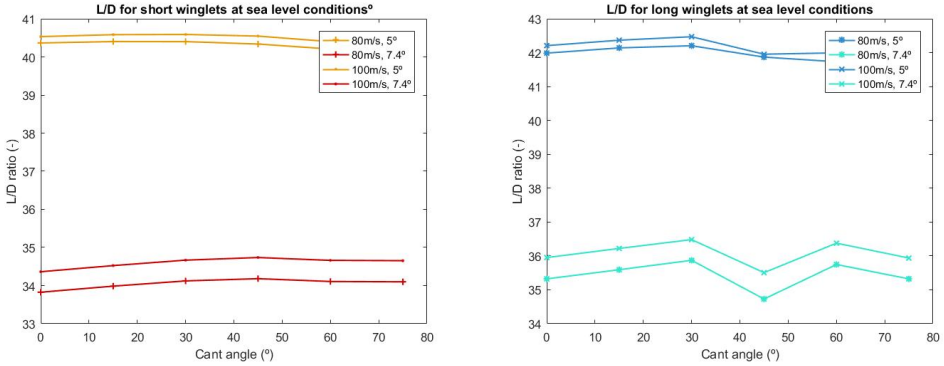

Figure 10.8: L/D ratio for short and long winglets at different α. Sea level

As it can be observed in figures 10.7 and 10.8, the aerodynamic efficiency is far larger for lower angles of attack: for a wing with a long winglet at $\Theta = 45^o$, flying at cruise conditions, it climbs from $L/D = 37.14$ for an angle of attack $\alpha = 7.4^o$ to 42.65 for $\alpha = 5^o$. Although this may seem counterintuitive at first, since a part of the lift coefficient is directly proportional to α, it is important to remember that for the parabolic drag polar the drag coefficient varies with the square of the lift coefficient, and thus variations in drag will be much larger than variations in lift. It is safe, then, to determine that the angle of attack is the main parameter affecting the magnitude of the L/D ratio. Although the maximum aerodynamic efficiency seems to be reached at the same cant angle of $\Theta = 45^o$ for the long winglets at the cruise altitude and $\Theta = 30^o$ at sea level, the results obtained in the previous section for a more detailed scope of cant angles between 30^o and 60^o seem to suggest that further research could modify these conclusions.

10.4 Comparing XFLR5 and CFD results

As it can be observed in figures 10.9 and 10.10, there were some significant differences between the results provided by XFLR5 and those obtained through computational fluid dynamics in ANSYS Fluent. XFLR5 results, as mentioned in previous sections, indicate an aerodynamic efficiency higher than that of the basic wing for every winglet geometry and cant angle. This is quite different for CFD results, which show that the aerodynamic efficiency is only improved for a limited range of cant angles in every geometry and flight condition.

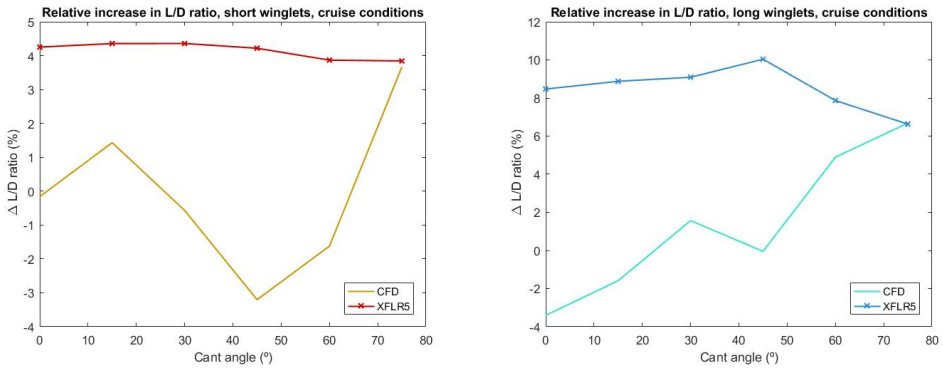

Figure 10.9: Increase in L/D ratio for long and short winglets, cruise conditions

Although both analyses show greater effects for long winglets than for short winglets, confirming the role of winglet area on lift generation and drag reduction, and the order of magnitude of the L/D variations is similar, the general trends observed for increasing cant angles diverge. XFLR5 results show a moderate increase in aerodynamic efficiency up to $\Theta = 30^o$ or $\Theta = 45^o$, while Fluent results often present a sharp fall at similar cant angles and a clear growth for higher Θ. This is probably due to the difficulties linked to wake and vortex modeling in XFLR5, which cause the results to be predominantly

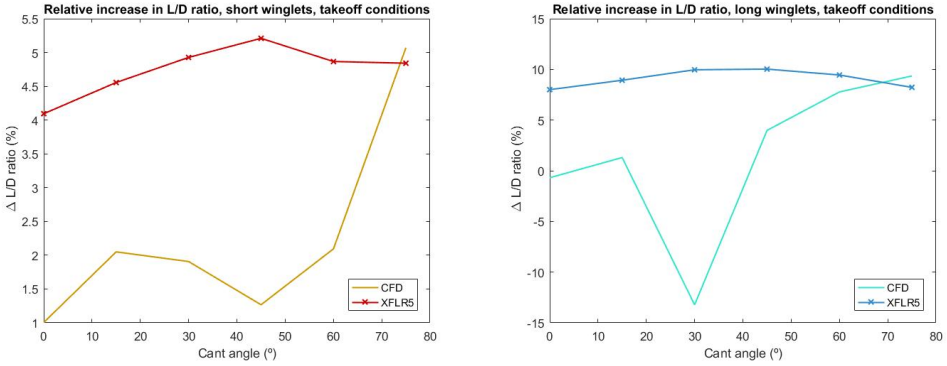

Figure 10.10: Increase in L/D ratio for long and short winglets, takeoff conditions

based on the increase in lift coefficient related to the effective span.

While CFD results could surely be improved with a larger, more refined mesh, and a number of analyses considering different altitudes, speeds, and angles of attack would be desirable, for the moment they are considered to be much more reliable than those obtained through the three-dimensional panel method. XFLR5 results should be examined with caution and employed only as an indicator of the order of magnitude of the improvements in aerodynamic efficiency which, for every flight condition, could be obtained by incorporating wingtip devices to the wing design.

Chapter 11

Project Budget and Planning

11.1 Project budget

The budget for this project was estimated by taking into account fixed costs -such as those related to the equipment and software licenses-, working hours,and electricity. As shown in Table 11.1, equipment costs included the 3D printer, six-degree transducer, laptop computer and oscilloscope employed for the experimental measurements, as well as ANSYS Fluent, CATIA, and MatLab^{TM} licenses. The working life of each product was estimated as one year for the software licenses, five years for the laboratory equipment[1], four years for the laptop computer and cables, and 200h per kilogram of ABS plastic for the given printer speed. Assuming that all equipment and software licenses would have other uses unrelated to this project, the percentage of the overall cost of each product invested in this work in particular was computed by assuming 1600 working hours in a year for general purposes and 4000h for ANSYS Fluent, where simulations can be programmed to run continuously.

The number of definitive XFLR5 simulations employed for this project amounted to 204, including six devoted to the initial grid-independence study and 198 for the case studies. Each analysis took an average of eight minutes to run, yielding a total of 27.2 simulation hours; when the additional failed analyses are taken into account, this number increases to 38.08h. In a similar way, the fifty-three ANSYS Fluent simulations performed throughout this work amounted to 1590h, with an additional 180h to account for the failed attempts and 40 more hours dedicated to the design and generation of the mesh. The total laptop working hours were estimated to take into account ANSYS Fluent and XFLR5 simulations, CATIA modeling, meshing, and research and writing time, with some of these processes taking place simultaneously.

The total project fixed cost can then be estimated by taking into account only the percentage of each product's working life employed during this work, or by assuming the total costs, as shown in table 11.1. In order to calculate the overall costs, it was necessary to account for labor and electricity costs, as shown in tables 11.2 and 11.3. Electricity

[1]The cost for the load cell and amplifier is estimated, as no data could be found

Product	**Total cost**	**Time**	**Project cost**
3D Printer	200€	20h	0.5€
ABS plastic (1kg)	20€	20h	2€
Tektronix TDS 3014C Oscilloscope	2000€	20h	5€
Kyowa LAT-10KA-1 transducer	300€	25h	0.98€
UC3M-made amplifier	60€	25h	0.19€
USB and Ethernet cables	7.40€	25h	0.05€
Computer	700€	2000h	218.75€
Dassault CATIA Student license	99€	60h	3.71€
ANSYS Workbench Research license	2500€	1800h	1125€
XFLR5 license	0€	38h	0€
MatLab 2016 Student license	89€	40h	2.23€
Tuition, access to research facilities	318.12€	300h	318.12€
Total fixed costs	6,293.52€	-	1,676.53€

Table 11.1: Costs of equipment and software licenses

Equipment	Time	Consumption	Cost
3D Printer	20h	50W/h	0.12€
Water channel	20h	4400W/h	10.56€
Oscilloscope	20h	40W/h	0.10€
Computer	2000h	900W/h	216€

Table 11.2: Electricity costs

costs were assumed at 0.12€per kWh, and labor costs at 20€/h. The former was based on estimations from several major electricity providers in the Madrid area, while the latter was calculated from typical values for Bachelor-level engineering professionals in their first years in the field.

Task	Time (h)	Cost (€)
Research	60	1200
Software learning	40	800
Geometry modeling	60	1200
Mesh design and optimization	20	400
Simulations setup	20	400
XFLR5 simulations	40	800
Experimental measurements	35	700
Data processing and analysis	80	1600
Thesis writing	80	1600
Total	435	8700

Table 11.3: Labor costs

Finally, when gathering data from tables 11.1, 11.2, and 11.3, the total cost of the project was found at 10,603.31€, which seems reasonable when compared to similar engineering projects [10] which have taken place at Universidad Carlos III de Madrid.

11.2 Project planning

The planning defined for this project, shown as a Gantt diagram in figure 11.1, was designed to allocate as much time as possible to the ANSYS Fluent simulations, which were considered the key point of the study, required a considerable amount of computational time, and were likely to need changes and refining. As a matter of fact, the initial extent of the project, which included simulations at different angles of attack and flight conditions, as well as compressibility effects at higher Mach numbers- would require several more months to be completed. XFLR5 simulations, on the other hand, required a considerably shorter period of time, being based only on a simplified model of the flow equations and employing a much coarser mesh. The experimental measurements were a later addition to the project, and as such they had to be carried out on the last weeks of May, instead of at a more convenient, earlier time. The complications found with the experimental setup and instruments described in chapter 8 delayed the measurements yet some more weeks.

As it can be observed in the figure, several weeks were allocated for research in order to gain a better understanding of the principles behind the use of wingtip devices, their history, and the existing models currently employed in the aeronautical industry. Some time was devoted, as well, to find previous studies concerning optimization of winglet shapes, although the subject has not been treated extensively in literature. The selection of a suitable turbulence model for the ANSYS Fluent simulations, however, was extended far beyond the alloted period, as the mathematical foundations of each model had to be studied and understood. The time dedicated to the geometry design and modeling was quite long, as it involved learning the basis of CATIA modeling through the open resources available, and solving several unexpected problems -mainly related to three-dimensional boolean operations- which arose during the design process.

As for the data processing and analysis, it had to be postponed until a significant number of ANSYS Fluent simulations, as well as XFLR5 analyses, were complete. Although regular inspections were performed in the data obtained from every simulation, in order to detect any anomalies, the comparative study required the results of virtually all geometries considered. Several later additions to the initial objectives of the problem delayed the derivation of significant conclusions and patters from these results. For this reason, the thesis-writing process had to be postpone until the final weeks of May and early June, when a comprehensive portrait of the effect of wingtip devices on aerodynamic efficiency and aircraft performance had been achieved.

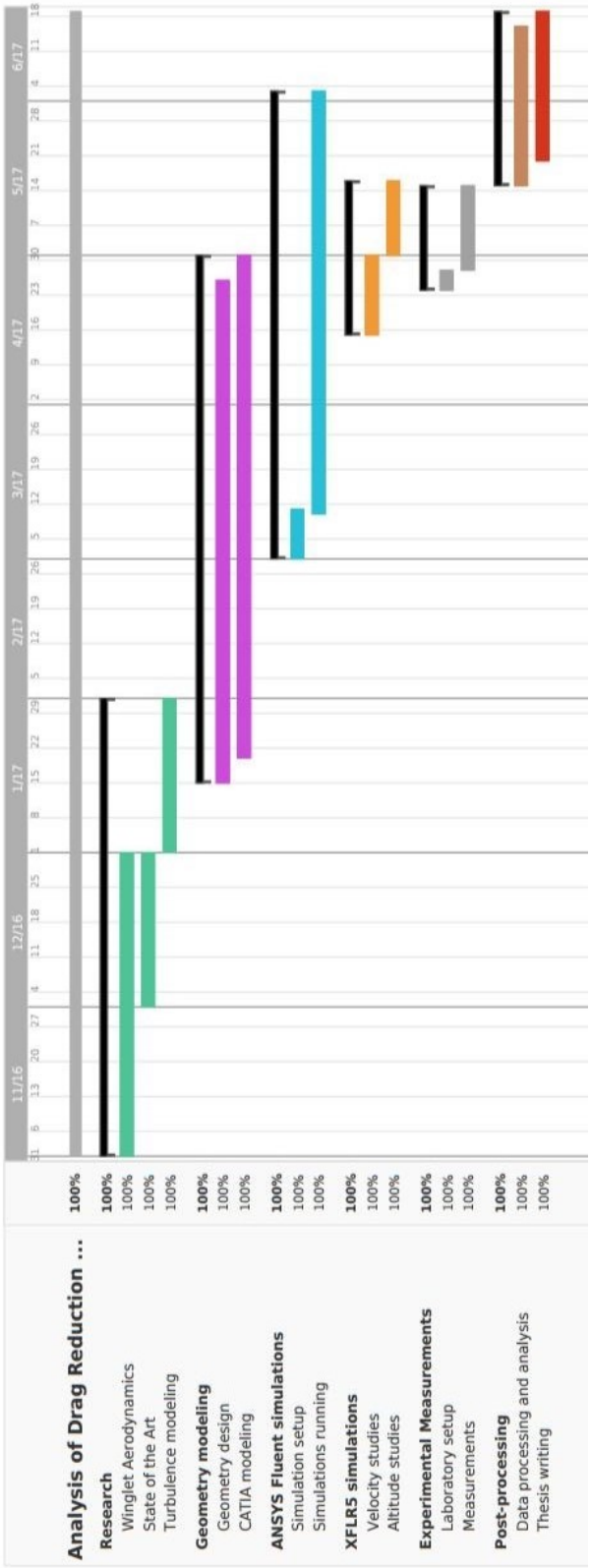

Figure 11.1: Gantt diagram for the project planning

Chapter 12

Conclusions and Future Work

12.1 Conclusion

The main objective of this project was to observe and analyze the effect of wingtip devices on the lift and drag forces acting on the aircraft. This was performed through the design of several wingtip device models for a wing similar to that of the CN235 aircraft, based on those commonly found in the market, for which several simulations were performed with fluid properties emulating cruise and takeoff conditions. Two main approaches -computational fluid dynamics, through ANSYS Fluent, and a three-dimensional panel method, through XFLR5- were employed, along with an unsuccessful attempt at experimental measurements. The main parameter used as an indicator of these effects was the aerodynamic efficiency, L/D, which was later employed in range and endurance calculations to show how its variations would modify flight performance in real-world applications. The main conclusions derived from this analysis were the following:

- Wingtip devices **affect lift and drag forces significantly**. A 10% increase in the lift-to-drag ratio, L/D, could be reached through some of the designs employed, resulting in a similar increase in range and endurance and decrease in takeoff field length and ground-roll landing distance.
- **Cant angle** Θ is one of the main parameters determining winglet performance. Winglets observed in ANSYS Fluent showed their peak performance at $\Theta = 60^{o}$ and $\Theta = 75^{o}$.
- **Winglet area** seems to be directly related to aerodynamic efficiency, with wingtip devices with a greater area yielding a higher L/D.
- **Double winglets** at $\Theta = 60^{o}$ provide an overall superior performance to all wingtip devices. This is thought to be due to their preventing flow recirculation around the wingtips more effectively.
- **Raked wingtips** and **wingtip fences** provide a modest increase in aerodynamic efficiency with a much smaller structural impact and little or none span extensions.

- A **relatively small fuid domain** is enough to provide an overview of the behavior of wings with and without wingtip devices, but a considerably large domain should be employed whenever possible.
- **Multi-winglet configurations** are surprisingly effective aerodynamically, but may become problematic from an structural approach.
- **XFLR5 results** cannot be considered realistic due to the oversimplified model employed by the software. They can be taken as a reference for key parameters, such as the effect of winglet area, but CFD simulations should be used.
- **Experimental measurements** cannot be performed with the tools available. The purchase of new instruments is strongly recommended.

In order to broaden the scope of this study, and to explore further the impact of wingtip devices in all disciplines affecting atmospheric flight, a much greater number of CFD simulations should be designed and run, considering a wide variety of flight conditions and geometric parameters.

12.2 Compliance with the project objectives

As it was mentioned in the introduction, this work included several main and secondary objectives, which have been fulfilled to the best of the available resources:

- To observe the effects of several wingtip devices of aircraft performance: the conclusions stated in the previous section provide an overview to this observation and summarize the main findings of this analysis.
- To find or suggest an optimum configuration to maximize aerodynamic efficiency: although it cannot be stated to be an *absolute* optimum, the double winglet at $\Theta = 60^{o}$ has been found to yield the best L/D ratio among all the models studied, for all flight conditions.
- To investigate the validity of the XFLR5 model: given the oversimplifications present in this model, it has been concluded that it is valid only for initial estimations and by no mean applicable to real cases.
- To conduct experimental measurements: although several attempts at obtaining empirical data for 3D printed model wings were performed, severe equipment limitations prevented their success. However, the most likely causes of these problems have been identified and a solution has been proposed towards future experimental works.

12.3 Future work

Although the study presented in this work has reached significant conclusions regarding the behavior and impact of wingtip devices from an aerodynamic standpoint, it cannot by any means be considered complete. In order to truly provide a holistic understanding of this matter, a number of additional studies should be undertaken, including:

- An extensive analysis of the effect of several geometric parameters not considered here, including geometric and aerodynamic twist, sweep angle, multiple-airfoil sections, optimized multi-winglet configurations, and combinations of several wingtip devices. As only six possible cant angles Θ were considered in this work, many more points should be incorporated to the research.
- Further research into the effect on aerodynamic efficiency of different winglet configurations at more flight conditions, regarding the variations due to changes in the flight velocity, altitude, and angle of attack. Although some estimations of the effect of these variables on the flow have been obtained through XFLR5, they cannot be considered reliable.
- Considerations of the effects of an increased wingspan on the dynamic stability and handling qualities of the aircraft, as wingtip devices will most likely affect several stability derivatives and alter the pitching, yawing, and rolling moments.
- A study of the impact of an additional point mass at the wingtips in the vibration modes -bending and torsion- of the wing, as well as the moment and forces at the wing root, which may reduce the fatigue life of the structure. Aeroelastic effects -such as divergence and flutter- should also be considered.
- Experimental measurements performed with a new, calibrated load cell, updated software, and a precise measurement system, aiming to reproduce or correct the results found in the CFD simulations. Ideally, a similarly high Reynolds number would be used for this analysis, involving both the water channel and wind tunnel if possible.
- CFD simulations aiming to understand the behavior of wingtip devices at higher Mach numbers, including compressibility effects, unsteady regimes, and careful identification of hypothetical transonic effects.
- An aeroacoustic study of the noise reduction that several manufacturers have allegedly achieved by incorporating wingtip devices to their design, trying to assess the role of wingtip vortices in noise generation.

It is likely that, during the development of these studies, further considerations will arise regarding aspects not yet considered in this project. As it is often the case in technological and scientific research, it is only logical to expect future works to provide answers to some of the fundamental topics presented here, while revealing a much wider range of questions to explore.

Bibliography

[1] J. D. Anderson, *History of Aerodynamics And its Impact on Flying Machines.* Cambridge, etc: Cambridge University Press, 1997.

[2] J. D. Anderson, *Fundamentals of Aerodynamics.* New York, etc.: McGraw-Hill, 2011.

[3] S. Biringen, C. Y. Chow, *An Introduction to Computational Fluid Dynamics by Example.* Hoboken (NJ): John Wiley & Sons, 2011.

[4] T. Cebeci, *An Engineering Approach to the Calculation of Aerodynamic Flows.* Long Beach; Berlin, etc: Horizons; Springer, 1999.

[5] T. Cebeci and J. Cousteix, *Modeling and Computation of Boundary-Layer Flows: Laminar, Turbulent and Transitional Boundary Layers in Incompressible Flows.* Long Beach, CA, etc: Horizons ; Berlin etc.: Springer, 1999.

[6] T. Cebeci, *Turbulence Models and their Application : Efficient Numerical Methods with Computer Programs.* Long Beach California; Berlin, etc: Horizons; Springer, 2004.

[7] T. Cebeci, *Analysis of Turbulent Flows.* Amsterdam, etc: Elsevier, 2004.

[8] R. M. Cummings et al, *Applied Computational Aerodynamics: A Modern Engineering Approach.* New York: Cambridge University Press, 2015.

[9] J. Dussauge and W. S. Saric. *Turbulent Boundary Layers in Subsonic and Supersonic Flow*, 1996-335.

[10] J. Gallego Moreno,"Analysis of the Performance of a Flexible Winglet in the Presence of Gusts", Bachelor Thesis, Department of Bioengineering and Aerospace Engineering, Universidad Carlos III de Madrid, Madrid, Spain, 2016.

[11] J.C. García Hiniesta, S. Esteban Roncero, *XFLR5: Manual de Iniciación.* Departamento de Ingeniería Aeroespacial y Mecánica de Fluidos, Escuela Superior de Ingenieros, Universidad de Sevilla, 2013.

[12] J. Hilario, *Design Weights and Range.* Class notes for Aircraft Design, Universidad Carlos III de Madrid, Madrid, Spain, 2017.

[13] C. Hirsch, *Numerical Computation of Internal and External Flows: Introduction to the Fundamentals of Computational Fluid Dynamics.* Oxford: Butterworth-Heinemann, 2007.

[14] D. Howe, *Aircraft Conceptual Design Synthesis*: John Wiley & Sons, 2014.

[15] R. de la Iglesia Barbera, *Obtención Experimental de la Matriz de Calibración de una Célula de Carga*, Bachelor Thesis, Department of Bioengineerig and Aerospace Engineering, Universidad Carlos III de Madrid, Madrid, Spain, 2013.

[16] P. Jackson (editor), *Jane's all the World's Aircraft.* Surrey: Jane's Information Group, 1955.

[17] J. Katz and A. Plotkin, *Low Speed Aerodynamics.* Cambridge, etc: Cambridge University Press, 2001.

[18] A. K. Kundu, *Aircraft Design.* Cambridge: Cambridge University Press, 2010.

[19] A. Mateos and A. Mosquera, *Analysis of a Tapered Wing in Compressible Regime*, Department of Bioengineering and Aerospace Engineering, Universidad Carlos III de Madrid, Madrid, Spain, 2016.

[20] G. Narayan, B. John, *Effect of winglets induced tip vortex structure on the performance of subsonic wings*, Aerospace Science and Technology 58, 328-340; Elsevier, 2016.

[21] D. P. Raymer, *Aircraft Design: A Conceptual Approach.* Blacksburg Virginia: American Institute of Aeronautics and Astronautics, 2012.

[22] Sohail R. Reddy et al. "Multi-winglets: Multi-objective optimization of aerodynamic shapes," in 53rd AIAA Aerospace Sciences Meeting. DOI: 10.2514/6.2015-1489.

[23] J. Tu, G. H. Yeoh and C. Liu, *Computational Fluid Dynamics.* Amsterdam; Boston: Elsevier/Butterworth-Heinemann, 2013.

[24] Narcis Ursache et al. *Morphing winglets for aircraft multi-phase improvement.* Bristol University, Bristol (UK), BS81TR- 2007.

[25] M. Van Dyke, *An Album of Fluid Motion.* Stanford, California: The Parabolic Press, 1982.

[26] `http://www.aircraft.airbus.com/aircraftfamilies/passengeraircraft/a320family/` [Last Accessed: 10/06/2017].

[27] `http://www.airfoiltools.com` [Last Accessed: 10/06/2017],

[28] `http://www.airport-data.com` [Last Accessed: 13/04/2017].

[29] `http://www.ansys.com` [Last Accessed: 16/06/2017].

[30] ANSYS, Inc. Release 15.0, *ANSYS Fluent Theory Guide*, http://www.ansys.com, 2013.

[31] https://www.aso.com/listings/spec/ViewAd.aspx?id=134765 [Last Accessed: 23/05/2017].

[32] http://www.aviationpartnersboeing.com/ [Last Accessed: 05/06/2017].

[33] https://aviation.stackexchange.com/ [Last Accessed: 09/06/2017].

[34] http://www.bakker.org/dartmouth06/engs150/ [Last Accessed: 16/06/2017].

[35] http://flyingmachines.org [Last Accessed: 15/04/2017].

[36] http://www.indonesian-aerospace.com [Last Accessed: 13/06/2017].

[37] K. Lehmkuehler and K. C. Wong. *Winglet design for a Fairchild Merlin III using CFD analysis*. 2011, Available: http://search.informit.com.au/. [Last Accessed: 10/06/2017].

[38] https://www.nasa.gov/centers/dryden/ [Last Accessed: 04/06/2017].

[39] https://www.reddit.com/r/aviation/comments/30o3tv/a-falcon-50-with-a-spiroid-winglet/ [Last Accessed: 11/06/2017].

[40] https://www.seo.org [Last Accessed: 15/06/2017].

[41] https://www.transtats.bts.gov/fuel.asp?pn=1 [Last Accessed: 16/06/2017].

[42] W. Schoppa and F. Hussain.*A large-scale control strategy for drag reduction in turbulent boundary layers.* Physics of Fluids 10(5), pp. 1049-1051. 1998. Available: http://dx.doi.org/10.1063/1.869789. DOI: 10.1063/1.869789. [Last Accessed: 05/05/2017].

[43] Y. Wei and Y. Zhigang. *Aerodynamic investigation on tiltable endplate for WIG aircraft*. Aircraft Engineering and Aerospace Technology 84(1), pp. 4-12. 2012. Available: http://search.proquest.com/docview/916979153. DOI: 10.1108/00022661211194933. [Last Accessed: 08/06/2017].

[44] http://winglet-technology.com/CitationX.html [Last Accessed: 16/04/2017].

[45] *Compact FieldPoint^{TM} cFP-180x Quick Start Guide*, National Instruments, 2005.

[46] *Ethernet /Serial Interfaces for Compact FieldPoint*, National Instruments, 2006.

[47] *Kyowa LAT-1000A Series Datasheet*, Kyowa Catalog, available at http://www.kyowa-ei.com/eng/product/category/sensors/s_lat-1000a_series/index.html [Last Accessed: 14/06/2017].

[48] *XFLR5 v6.02 Guidelines*, 2013. Available at: http://www.xflr5.com/xflr5.htm [Last Accessed: 15/05/2017].

[49] *Certification Specifications and Acceptable Means of Compliance for Large Aeroplanes*, European Aviation Safety Agency, CS25-2017.

[50] *IATA Technology Roadmap*, International Air Transport Aviation, 2013.

[51] *Military Specification: Airplane Strength and Rigidity Ground Tests*, U.S. Department of Defense, MIL-A-8867C(AS)-1987.

[52] *UAV Systems Airworthiness Requirements (USAR) for North Atlantic Treaty Organization (NATO) Military UAV Systems*, North Atlantic Treaty Organization, draft STANAG 4671-2007.

[53] *Advisory Circular: Damage Tolerance Inspections for Repairs and Alterations*, Federal Aviation Administration, AC120-93-2007.

[54] *Advisory Circular: Certification of Part 23 Airplanes for Flight in Icing Conditions*, Federal Aviation Administration, AC23.1419-2D-2007.